Direct Solar–powered Membrane Distillation for Small–scale Desalination Applications

by

Ahmad Mohammed O. Bamasag

A Dissertation Presented in Partial Fulfillment
of the Requirements for the Degree
Doctor of Philosophy

Approved October 2020 by the
Graduate Supervisory Committee:

Patrick E. Phelan, Chair
Abdelrahman Shuaib
Liping Wang
Luis Bocanegra
Ronald Roedel

ARIZONA STATE UNIVERSITY

December 2020

ABSTRACT

Water desalination has become one of the viable solutions to provide drinking water in regions with limited natural resources. This is particularly true in small communities in arid regions, which suffer from low rainfall, declining surface water and increasing salinity of groundwater. Yet, current desalination methods are difficult to be implemented in these areas due to their centralized large-scale design. In addition, these methods require intensive maintenance, and sometimes do not operate in high salinity feedwater. Membrane distillation (MD) is one technology that can potentially overcome these challenges and has received increasing attention in the last 15 years. The driving force of MD is the difference in vapor pressure across a microporous hydrophobic membrane. Compared to conventional membrane-based technologies, MD can treat high concentration feedwater, does not need intensive pretreatment, and has better fouling resistance. More importantly, MD operates at low feed temperatures and so it can utilize low–grade heat sources such as solar energy for its operation. While the integration of solar energy and MD was conventionally indirect (i.e. by having two separate systems: a solar collector and an MD module), recent efforts were focused on direct integration where the membrane itself is integrated within a solar collector aiming to have a more compact, standalone design suitable for small-scale applications. In this dissertation, a comprehensive review of these efforts is discussed in Chapter 2. Two novel direct solar-powered MD systems were proposed and investigated experimentally: firstly, a direct contact MD (DCMD) system was designed by placing capillary membranes within an evacuated-tube solar collector (ETC) (Chapter 3), and secondly, a submerged vacuum MD (S-VMD) system that uses circulation and aeration as agitation techniques was investigated (Chapter 4). A maximum water production per

absorbing area of 0.96 $kg \cdot m^{-2} \cdot h^{-1}$ and a thermal efficiency of 0.51 were achieved. A final study was conducted to investigate the effect of ultrasound in an S-VMD unit (Chapter 5), which significantly enhanced the permeate flux (up to 24%) and reduced the specific energy consumption (up to 14%). The results add substantially to the understanding of integrating ultrasound with different MD processes.

To my parents, Mohammed & Noor, who have worked so hard for the well-being of their children.

To my wife, Manal, & my daughter, Yasmin, for their unconditional love and support.

ACKNOWLEDGMENTS

First, I am thankful to God for giving me the courage and strength to pursue this research, along with countless other blessings.

I would like to express my sincere gratitude to my advisor Dr. Patrick Phelan, for having confidence in me and giving me the great opportunity to work in his lab. Thank you, Pat, for your guidance, help, willingness to teach me!

I also would like to thank my committee members, Dr. Abdelrahman Shuaib, Dr. Liping Wang, Dr. Luis Bocanegra, and Dr. Ronald Roedel, for taking time from their busy schedule to review my dissertation and for their insightful feedback. Special thanks go to Dr. Shahnawaz Sinha and Dr. Noreddine Ghaffour, for their collaboration and for sharing their expertise in water treatment technology.

I am also thankful to all my friends and colleagues from around the world, with whom I shared unforgettable moments during my PhD journey: Amr, Ali, Misbah, Abdulmajeed, Akhtar, Benjamin, Emmanuel, Praveen, and many others. A special thank goes to my friend Talal Alqahatani, who supported me in any possible way. This work wouldn't have been possible without your encouragement and assistance. I also want to thank my friend Hooman Daghooghi for offering help and support whenever I need it.

I also would like to express my deepest gratitude to my father, mother, sister, and brothers. They have always supported me and encouraged me with their best wishes and prayers.

Most of all, I would like to thank my wife, Manal, my best friend and the love of my life. Thank you for the love, patience and help through all these years. A special thank-you

to my daughter, Yasmin, for making me smile every day. Without you both I would be lost!

Finally, I gratefully acknowledge King Abdulaziz University (KAU) for supporting my graduate study in the USA.

TABLE OF CONTENTS

Page

LIST OF TABLES x

LIST OF FIGURES xi

NOMENCLATURE xv

CHAPTER

1 INTRODUCTION 1

1.1 Membrane Distillation (MD) 1

1.1.1 MD Configurations and Modules 2

1.1.2 Mass and Heat Transfer Basics 4

1.2 Research Gap and Objectives 9

1.3 Motivation and Potential Impact 12

1.4 Potential Challenges 14

1.5 Dissertation Structure 15

2 DIRECT SOLAR–POWERED MEMBRANE DISTILLATION: A REVIEW OF LITERATURE 17

2.1 Indirect SP–MD Systems 18

2.2 Direct SP–MD Systems 20

2.2.1 Heating Via Absorbing Plate 22

2.2.2 Heating Via A Coated Layer on The Membrane: 26

CHAPTER Page

2.3 Limitations and Conclusion Remarks 28

3 DIRECT SOLAR–POWERED DCMD SYSTEM USING EVACUATED TUBE COLLECTOR 31

3.1 Materials and Methodology 33

3.1.1 The Design of The Direct SP–MD Module 33

3.1.2 Experimental Setup and Procedure 36

3.1.3 Performance and Uncertainty Analysis 40

3.2 Results and Discussion 42

3.2.1 Indoor Experiments Under Steady–State Conditions 42

3.2.2 Daily Performance for Outdoor Experiments 49

3.3 Summary 56

4 SOLAR–HEATED SUBMERGED VACUUM MEMBRANE DISTILLATION SYSTEM 58

4.1 Materials and Methodology 62

4.1.1 The Design of the S–MD Module 62

4.1.2 Experimental Setup and Procedure 64

4.1.3 Uncertainty Analysis 67

4.2 Results and Discussion 68

4.2.1 Indoor Experiments Under Steady–State Conditions 68

CHAPTER Page

4.2.2 Outdoor Experiments Under Ambient Weather Conditions 72

4.2.3 Technical Assessment of The Outdoor Tests 77

4.2.4 Comparison of Some Direct Heating SP–MD Desalination Systems 81

4.2.5 Long-Term Operation 85

4.3 Summary 89

5 PERFORMANCE ENHANCEMENT OF A SUBMERGED VACUUM MEMBRANE DISTILLATION SYSTEM USING LOW-POWER ULTRASOUND 90

5.1 Materials and Methodology 93

5.1.1 Membrane and Module Specifications 93

5.1.2 Experimental Setup and Procedure 94

5.1.3 Uncertainty Analysis 97

5.2 Results and Discussion 98

5.2.1 The Performance of the Ultrasonic-Assisted S-VMD with Feed Temperature 98

5.2.2 Identifying the Ultrasonic Enhancing Mechanisms 101

5.2.3 The Influence of Feed Temperature on the Ultrasound-Assisted Enhancement 104

CHAPTER Page

5.2.4 The Influence of Ultrasonic Frequency on the Ultrasound-Assisted Enhancement 104

5.2.5 The Performance of the Ultrasonic-Assisted S-VMD with Feed Concentration 106

5.2.6 Long-term Operation 108

5.2.7 Enhancement in Specific Energy Consumption 112

5.3 Summary 114

6 CONCLUSIONS 116

7 FUTURE WORK 119

REFERENCES 122

APPENDIX

A. CO-AUTHOR PERMISSION STATEMENT 132

B. LIST OF PUBLICATIONS 134

LIST OF TABLES

Table Page

1. Major MD Configurations 3

2. Characteristics of the Direct SP–MD Modules..... 35

3. Uncertainty Analysis..... 42

4. Characteristics of the Solar–Heated S–VMD Module..... 63

5. Comparison of Performance Parameters for Different Experimental Runs 78

6. Comparison of Some Direct Heating SP–MD Desalination Systems 84

7. Characteristics of the S-VMD Module 94

LIST OF FIGURES

Figure Page

1. Basic Working Principle of MD 2

2. (a) Flat-Sheet Membrane in a Plate–and–frame Module, (b) Hollow Fiber Membranes in a Shell–and-tube MD Module, and (c) Spiral Wound Membranes 4

3. Heat and Mass Transfer Mechanisms in a DCMD System. 6

4. Integration of Solar Energy Membrane Distillation Systems 9

5. Conceptual Illustrations of Direct SP–MD Systems Using (a) Flat-sheet Membranes, and (b) Tubular Membranes..... 11

6. Indirect SP–MD System Using (a) a Single Loop, and (b) Two Loops. 19

7. The Temperature Profile at the Feed Side in Direct SP–MD Systems (a) When the Solar Radiation Is Applied at an Absorbing Plate, and (b) When the Heating Is Applied at the Membrane Surface. 21

8. Direct SP–MD Systems Equipped with an Absorbing Plate Working Under the (a) VMD, (b) DCMD, and (c) AGMD Configurations 23

9. Direct SP–MD Systems Equipped with a Heated Coated Membrane Under the (a) AGMD, (b) DCMD, and (c) VMD Configurations. 26

10. A Schematic Diagram (Top), and a Photograph (Bottom) of the ETC–MD Modules. 34

11. (a) A Schematic Diagram and (b) a Photograph of the Indoor Experimental Setup. 37

12. (a) A schematic Diagram and (b) a Photograph of the Outdoor Experimental Setup. 39

Figure Page

13. A Simplified Energy Balance Diagram in an MD Process. 41

14 The Effect of the Feed Inlet Temperature on the Permeate Flux with and without Radiation Heat Flux for (a) Module#1 and (b) Module#2. (at Feed Concentration: 3.5%, $\dot{m}_f$=0.008–0.02 kg/s, $\dot{m}_p$=0.008 kg/s, $T_{p,i}$=~22 °C) 45

15. The Difference Between the Inlet and the Outlet Temperature of the Feed and the Permeate Streams with the Feed Inlet Temperature with and without Radiation Heat Flux for (a) Module#1 and (b) Module#2. (at Feed Concentration: 3.5%, $\dot{m}_f$=0.008–0.02 kg/s, $\dot{m}_p$=0.008 kg/s, $T_{p,i}$=~22 °C) 47

16. GOR for Module#1 and Module#2 as a Function of Feed Inlet Temperature with and without the Effect of Radiation. (at Feed Concentration: 3.5%, $\dot{m}_f$=0.008–0.02 kg/s, $\dot{m}_p$=0.008 kg/s, $T_{p,i}$=~22 °C) 49

17. Outdoor Test Data on September 28th, 2019 for the Two ETC Configuration. (a) The Solar Radiation and the Inlet/Outlet Temperatures of the Feed and Permeate Water, and (b) the Hourly Cumulative Distillate Water and Permeate Flux..... 52

18. Outdoor Test Data on October 1st, 2019 for the Three ETC Configuration. (a) The Solar Radiation and the Inlet/Outlet Temperatures of the Feed and Permeate Water, and (b) the Hourly Cumulative Distillate Water and Permeate Flux..... 54

19. Conceptual Illustration of a Multi–stage Direct Heating SP–MD System 56

20. A Schematic Diagram (Top), and a Photograph (Bottom) of the S–VMD Module. 62

21. (a) A schematic Diagram, and (b) a Photograph of the Outdoor Experimental Setup. 65

22. Different Modes of Feed Agitation: (a) Aeration, (b) Internal Circulation. 66

Figure Page

23. (a) Permeate Flux J and (b) the Flux Enhancement Ratio Φ as a Function of the Feed Temperature with and without Feed Agitation, from the Indoor Experiments. (P_v = –94.5 ± 1.0 kPa). 71

24. Solar Intensity for Different Sunny Outdoor Experimental Runs (Different Days). 72

25. Variation of Feed Temperature for Different Sunny Outdoor Experimental Runs (Different Days). 73

26. Variation of Permeate Flux of the S–VMD System with and without Agitation, from the Outdoor Experiments on Sunny Days. (P_v = –94.5 ± 1.0 kPa). 75

27. The Changes in Solar Intensity, Feed Temperature, and Permeate Flux of the S–VMD without Agitation on a Cloudy Day (P_v = –94.5 ± 1.0 kPa). 77

28. Comparison of *GOR* and *SEEC* of the S–VMD System from Different Outdoor Experimental Runs (P_v = –94.5 ± 1.0 kPa), where the *SEEC* Values Are Estimated for A_a = 1 m^2 (10 ETCs) Based on Our Experimental Results with 1 ETC. 81

29. The Feed Temperature Profiles of a One-Day Test in an Indoor Controlled Environment and in the Outdoor Test. 86

30. The Performance of the S-VMD System Over 13 Days (P_v = -94.5 ± 1.0 kPa). 88

31. A Schematic Diagram (Left) and a Photograph (Right) of the S-VMD Modules. .. 93

32. A Schematic Diagram of the Experimental Setup. 95

33. Permeate Flux J with and without Ultrasound at (a) f = 40 kHz, and (b) f = 28 kHz, and (c) the Flux Enhancement Ratio Φ (P_v = -93.5 ± 0.5 kPa, Feed Concentration = 35 g/L). 99

Figure Page

34. The Variation of Kinematic Momentum (a) and (b) Critical Cavitation Bubble Radius with Ultrasonic Power, Frequency, and Feed Water Temperature. 101

35. (a) Permeate flux J and (b) the Flux Enhancement Ratio Φ as a Function of Feed Concentration with and without Ultrasound. (P_v = -93.5 ± 0.5 kPa, $T_{f,b}$ = 55 ^{o}C, W_{US} = 30 W, and f = 40 kHz)..... 107

36. The Variation of Permeate Flux J and Conductivity as a Function of Feed Concentration Factor with and without Ultrasound. (P_v = -93.5 ± 0.5 kPa, $T_{f,b}$ = 65 ^{o}C, Initial NaCl Concentration = 100 g/l, W_{US} = 30 W, and f = 40 kHz)..... 109

37. SEM/EDS of Membrane Surface and Cross Section at the End of the Long-Duration Test with And without Ultrasound..... 111

38. The Ultrasonic Enhanced Specific Energy Consumption (*UESEC*) (P_v = -93.5 ± 0.5 kPa, Feed Concentration = 35 g/L). 114

NOMENCLATURE

A_a	Projected Absorbing Area of a Solar Collector (m^2)
A_m	Membrane Effective Surface Area (m^2)
b	Transducer Radius (m)
c	Speed of Sound ($m\ s^{-1}$)
C_p	Specific Heat Capacity ($J\ kg^{-1}\ ^oC^{-1}$)
E_T	Acoustic Energy Delivered By Transducer (J)
F	Kinematic Momentum ($kg^2\ m^{-2}\ s^{-2}$)
f	Ultrasonic Frequency (kHz)
GOR	Gain Output Ratio (-)
h	Heat Transfer Coefficient ($W\ m^{-2}\ K^{-1}$)
h_{fg}	Latent Heat of Water (J/kg)
I	Solar Intensity (W/m^2)
I_a	Acoustic Intensity ($W\ m^{-2}$)
I_{rms}	Root Mean Square Current (A)
J	Permeate Flux ($kg\ m^{-2}\ h^{-1}$)
k	Thermal Conductivity ($W\ m^{-1}\ K^{-1}$)
K	Mass Transfer Coefficient ($kg\ Pa^{-1}\ m^{-2}\ h^{-1}$)
m_d	Distillate Water Mass (kg)
$\dot{m}_{HTF}$	Mass Flow Rate of the Heat Transfer Fluid (kg/s)
P_a	Acoustic Pressure (Pa)
P_b	Bubble Pressure (Pa)

$P_{f,m}$	Feed Vapor Pressure at the Membrane Surface (Pa)
$P_{p,m}$	Permeate Vapor Pressure at the Membrane Surface (Pa)
P_h	Hydraulic Pressure (Pa)
P_l	Fluid Instantaneous Pressure (Pa)
P_{max}	Bubble Maximum Pressure (Pa)
P_v	Vacuum Pressure (Pa)
$\dot{Q}$	Heat Rate (W)
SEC	Specific Energy Consumption (kWh kg^{-1})
SEEC	Specific Electric Energy Consumption (kWh kg^{-1})
STEC	Specific Thermal Energy Consumption (kWh kg^{-1})
T_f	Feed Temperature (^oC)
$T_{f,b}$	Feed Temperature at the Bulk Phase (^oC)
$T_{f,m}$	Feed Temperature at the Membrane Surface (^oC)
T_p	Permeate Temperature (^oC)
$T_{p,b}$	Permeate Temperature at the Bulk Phase (^oC)
$T_{p,m}$	Permeate Temperature at the Membrane Surface (^oC)
T_{max}	Bubble Maximum Temperature (K)
ΔT_{HTF}	Temperature Drop of the Heat Transfer Fluid (^oC)
U	Overall Heat Transfer Coefficient (W m^{-2} K^{-1})
UESEC	Ultrasonic Enhanced Specific Energy Consumption (-)
V_{rms}	Root Mean Square Voltage (V)
x	Distance from Transducer (cm)

x_i	Salt Mass Fraction (kg/kg)
$\dot{W}$	Electric Power (W)
$\dot{W}_{US}$	Ultrasonic Power (W)
$\dot{W}_{vaccum}$	Vacuum Pump Power (W)

Greek letters

ε	Membrane Porosity (%)
Φ	Permeate Flux Enhancement Ratio (-)
θ	Phase Angle (Rad)
ρ	Density (kg m^{-3})
α	Acoustic Attenuation Coefficient (m^{-1})
ω	Angular Frequency (Rad)
γ	Specific Heat Ratio (-)
σ	Surface Tension (Nm^{-1})
μ	Dynamic Viscosity (Pa.s)
δ	Acoustic Displacement (m)

Subscripts

f	Feed
i	Inlet
m	Membrane
o	Outlet
p	Permeate

Abbreviations

AGMD	Air Gap Membrane Distillation
DCMD	Direct Contact Membrane Distillation
ED	Electrodialysis
ETC	Evacuated Tube Collector
FO	Forward Osmosis
HTF	Heat Transfer Fluid
MBR	Membrane Bioreactor
MD	Membrane Distillation
MED	Multiple-Effect Distillation
MSF	Multi-Stage Flash
RO	Reverse Osmosis
SGMD	Sweeping Gas Membrane Distillation
S-MD	Submerged Membrane Distillation
SP-MD	Solar-Powered Membrane Distillation
S-VMD	Submerged Vacuum Membrane Distillation
TDS	Total Dissolved Solids
TPC	Temperature Polarization Coefficient
VMD	Vacuum Membrane Distillation

1 INTRODUCTION

Water desalination has become one of the viable solutions for water shortage in regions with limited natural resources. This is particularly true in small communities in arid and semi-arid regions, which suffer from low rainfall, declining surface water, and increasing salinity of groundwater. Yet, conventional desalination methods are difficult to be implemented in these areas due to their centralized large-scale design. Desalination processes can be thermally driven and/or membrane-based systems [1,2]. Thermally driven desalination methods, such as multi-effect distillation (MED) and multi–stage flash (MSF), are widely used, but usually operate at high temperatures and require intensive maintenance due to corrosion and fouling issues. Membrane–based desalination methods include reverse osmosis (RO), electrodialysis (ED), and forward osmosis (FO). RO is a mechanical pressure–driven method that has dominated the desalination industry in recent years mainly because of its cost advantage. One drawback of RO, however, is that it doesn't operate in high-salinity feed water due to the osmotic limitation. Moreover, ED is more suitable for low-salinity solutions and FO is not a standalone process as it needs draw solution recovery which is itself an energy-intensive process [3].

1.1 Membrane Distillation (MD)

One technology that can potentially overcome some of the discussed challenges and has received more attention is *membrane distillation* (MD) [4]. MD is a thermally driven, membrane–based desalination process that uses a microporous hydrophobic membrane to separate the hot feed (saline) water and the cold permeate side. Due to the temperature gradient across the membrane wall, a vapor partial pressure difference is created which

drives water vapor to transfer from the hot side to the cold permeate side. Due to the hydrophobic nature of the membrane, non–volatile components in the feed solution cannot pass the membrane wall and only water vapor can pass. The basic working principle of MD is shown in Figure 1.

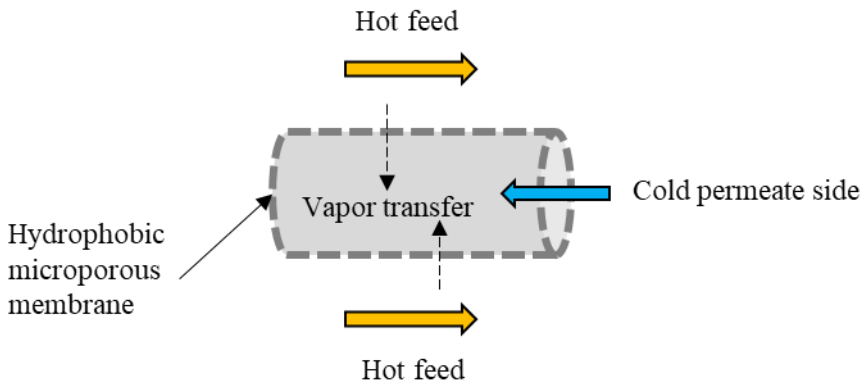

Figure 1. Basic Working Principle of MD

Unlike other desalination methods, MD can operate with high-concentration feed water (more than 25%) and doesn't need intensive pre–treatment. It also operates at low feed temperatures and so it can utilize low–grade heat sources such as solar energy, geothermal energy or waste heat for its operation [5]. In addition, MD systems can be integrated with conventional or other emerging desalination systems to desalinate the outlet brine, which helps in enhancing the overall water production and the specific energy [6,7]. For instance, one study found that water production and energy efficiency can be increased by 7.5% and 10%, respectively, when an MD system is integrated with an MED system [8].

1.1.1 MD Configurations and Modules

The four major MD configurations that have been intensively studied in the literature [4,9,10] are vacuum MD (VMD), air gap MD (AGMD), sweeping gas MD (SGMD), and

direct contact MD (DCMD). The main difference of these configurations is the way the condensation of vapor takes place on the permeate side of the MD module. Table 1 describes the mechanism of each type and its advantages and disadvantages. The DCMD and VMD systems are the most studied configurations due to their simplicity and applicability in the MD process. Recent studies have proposed new configurations such as material gap membrane distillation (MGMD) [11] and permeate gap membrane distillation (PGMD) [12].

Table 1 Major MD Configurations

Configuration	**Direct Contact MD (DCMD)**	**Vacuum MD (VMD)**	**Sweeping Gas MD SGMD**	**Air Gap MD (AGMD)**
Schematic	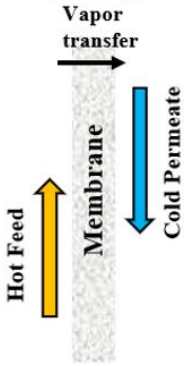	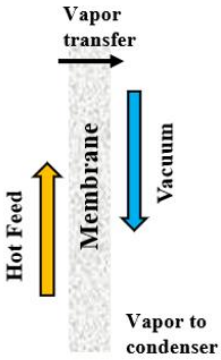	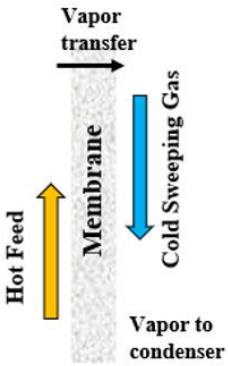	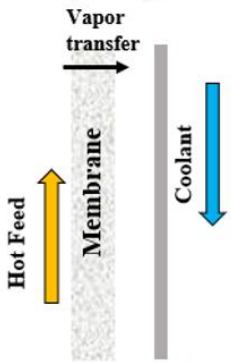
Permeate side	Cooling water	Vacuum	Cold sweeping gas	Air gap with cold plate
Condensation mechanism	Internal (in the permeate water)	external	external	Internal (on a cold surface)
Advantages	Simple operation, fewer equipment	High flux	Less heat loss	Easy heat recovery
Disadvantages	High conduction heat loss	Higher risk of wettability; more equipment	Higher electric energy requirements	High resistance to mass transfer; lower flux.

In addition to the different MD configurations, three main types of MD modules have been studied in the literature, namely plate–and–frame, shell–and–tube, and spiral wound modules. Schematics of these modules are shown in Figure 2. The plate–and–frame configuration is widely used in lab–scale systems due to the simplicity of construction. The

flat-sheet membranes used in this configuration are easy to be removed to test and clean. This makes it easier to test different membranes with the same module [13].

The spiral wound configuration uses flat-sheet membranes in a spiral arrangement, and it is similar to the plate–and–frame type in terms of theoretical modelling, but it has not been studied as much. This configuration has higher surface-area-to-module-volume ratio compared to the flat plate type, but it is more sensitive to fouling [13].

Shell–and–tube uses bundled capillary tubes or hollow fiber membranes and can be more attractive due to its very high membrane surface-area-to-module-volume ratio. This configuration usually works on DCMD and VMD systems, although the AGMD system has also been studied [14]. Despite its many advantages, it is more challenging to replace the membrane in case of wetting or scaling events [13,15]. Before the current study is described, several important concepts and definitions will be presented below.

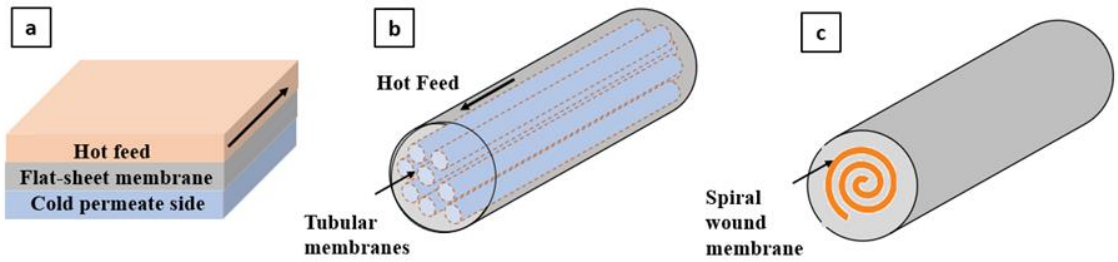

Figure 2. (a) Flat-Sheet Membrane in a Plate–and–frame Module, (b) Hollow Fiber Membranes in a Shell–and-tube MD Module, and (c) Spiral Wound Membranes

1.1.2 Mass and Heat Transfer Basics

The mass and heat transfer mechanisms in MD have been widely described in the literature [9,10]. Modelling heat transfer in MD systems is like modeling a heat exchanger, but it is more complicated because it involves mass transfer as well.

Figure 3 shows the mechanisms of mass and heat transfer in a DCMD system. The vapor transfer mechanism can be described in three steps [16]:

1) Vapor is generated on the hot feed side due to the vapor pressure difference.
2) Vapor transfers through the pores of the membrane.
3) Vapor condenses on the cold permeate side of the membrane in DCMD or AGMD systems or in an external condenser for other MD configurations.

The permeate flux of vapor is linearly dependent on the vapor partial pressure difference across the membrane. This relation is as follows [9,17]:

$$J = K(P_{f,m} - P_{p,m}) \tag{1.1}$$

where J is the water flux of the system ($kg \cdot m^{-2} \cdot h^{-1}$), K the mass transfer coefficient ($kg/Pa.m^2 \cdot h$), and $P_{f,m}$ and $P_{p,m}$ the partial pressures of water vapor at the feed and permeate side, respectively. Water vapor pressure at the surface of the membrane can be calculated using the Antoine equation as follows:

$$P_v = \exp\left[23.328 - \frac{3841}{T_{f,m} - 45}\right] \tag{1.2}$$

where P_v is in Pascal and $T_{f,m}$ is the water temperature at the membrane's surface (in Kelvin). The water vapor pressure decreases in the presence of salt in the feed water, and thus it should be accounted for using the following approximation (Raoult's law):

$$P_{f,m} = (1 - x_i)P_v \tag{1.3}$$

where x_i is the mass fraction of salt in water.

The mass transfer coefficient K is a function of both the membrane characteristics (such as pore size, thickness, porosity, etc.) and operation conditions (feed and permeate temperatures, pressures, flow rates, etc.) Different mechanisms have been developed to

model the transport of vapor through a porous medium: Knudsen model, ordinary–molecular diffusion model, viscous model, and/or a combination of two or more of those mechanisms.

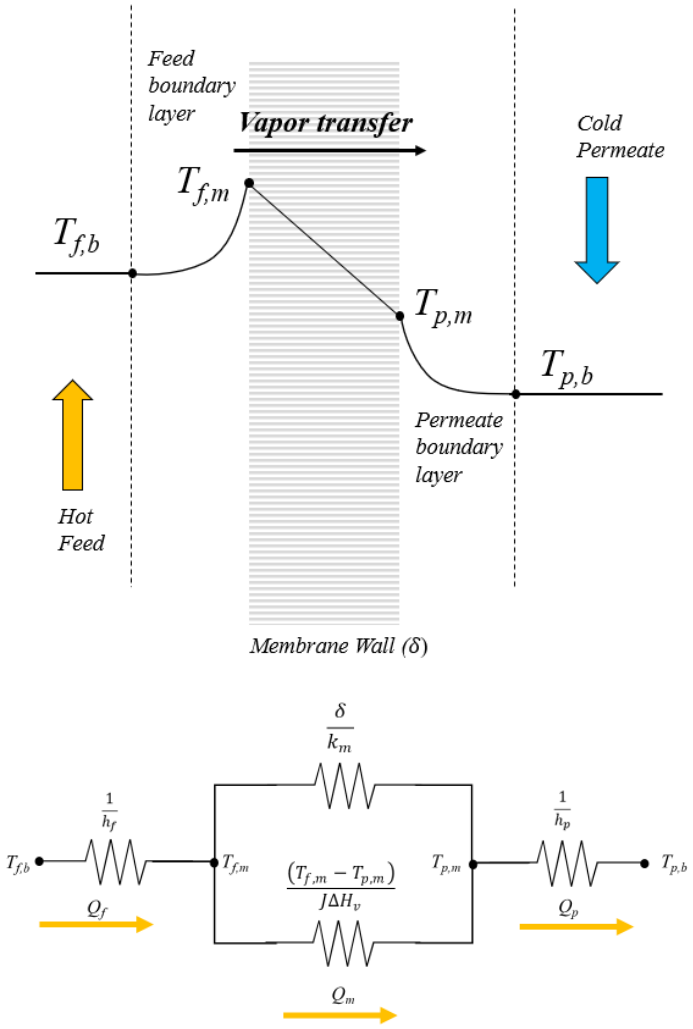

Figure 3. Heat and Mass Transfer Mechanisms in a DCMD System.

Heat transfer mechanisms in the MD can be divided into three steps:

1) Convection heat transfer in the boundary layer of the feed side (i.e. from the feed bulk temperature to the vapor–liquid interface at the membrane surface). This can be expressed as follows:

$$\dot{Q}_f = h_f(T_{f,b} - T_{f,m}) \quad (1.4)$$

2) Heat transfer across the membrane, which is a combination of conduction heat transfer through the membrane structure and air in the pores in addition to the latent heat of vaporization from vapor.:

$$\dot{Q}_m = \frac{k_m}{\delta_m}\left(T_{f,m} - T_{p,m}\right) + Jh_{fg} \quad (1.5)$$

3) Heat transfer in the permeate side boundary layer. In case of DCMD, this can be described as convection from the vapor-liquid interface at the membrane surface to the permeate side:

$$\dot{Q}_p = h_p(T_{p,m} - T_{p,b}) \quad (1.6)$$

In the above equations, Q is the heat transfer rate, h_f and h_p the heat transfer coefficients in the feed and permeate boundary layers, respectively, $T_{f,b}$ and $T_{f,m}$ the feed temperatures at the bulk phase and at the membranes surface, respectively, $T_{p,b}$ and $T_{p,m}$ the permeate temperatures at the bulk phase and at the membranes surface, respectively, h_{fg} the latent heat of vaporization, δ_m the membrane' thickness and k_m the total conductivity of the microporous membrane, which can be estimated using the following equation [17]:

$$k_m = \varepsilon k_g + (1 - \varepsilon)k_p \quad (1.7)$$

where ε is the membrane porosity, k_g the thermal conductivity of gas filling the membrane pores, and k_p the membrane material conductivity. The membrane porosity is defined as the void volume fraction of the membrane (i.e. the volume of the pores divided by the total volume of the membrane). The heat transfer coefficients h_f and h_p can be estimated using

semi–empirical equations of the dimensionless numbers (Nusselt number (*Nu*), Reynolds number (*Re*), and Prandtl number (*Pr*)).

At steady state, the total heat transfer flux through the system, *Q*, is given by:

$$\dot{Q} = \dot{Q}_f = \dot{Q}_p = \dot{Q}_m \tag{1.8}$$

Combining Eqs. (1.4) – (1.8), the total heat flux can be written as follows:

$$\dot{Q} = U\left(T_{f,b} - T_{p,b}\right) \tag{1.9}$$

where *U* is the overall heat transfer coefficient, which can be written as:

$$U = \frac{1}{h_f} + \frac{1}{\frac{k_m}{\delta} + \frac{Jh_{fg}}{\left(T_{f,m} - T_{p,m}\right)}} + \frac{1}{h_p} \tag{1.10}$$

Now, it is necessary to define an important phenomenon in MD systems, which is temperature polarization (TP). The Temperature Polarization Coefficient *TPC* is defined as the ratio of the temperature difference between the feed and permeate at the membrane surface to that in the bulk phases [18]. In DCMD, for example, *TPC* is defined as follows:

$$TPC = \frac{\left(T_{f,m} - T_{p,m}\right)}{\left(T_{f,b} - T_{p,b}\right)} \tag{1.11}$$

As seen in Figure 3, the feed temperature at the membrane surface is lower than the bulk feed temperature, which is a result of the presence of a boundary layer at the membrane surface in addition to the heat loss due to evaporation at the membrane surface. The temperature at the surface on the cold side is higher than that at the bulk permeate side due to the effect of condensation. A typical MD system will have lower thermal boundary layer resistance and a TPC value close to unity (i.e. the temperature difference between the bulk and surface temperatures is the same). According to [17], the TPC value varies

between 0.4–0.7 in DCMD systems. The temperatures of the membrane surface at the feed side and permeate side can be calculated as follows:

$$T_{f,m} = T_{f,b} - \frac{Jh_{fg} + k_m(T_{f,m} - T_{p,m})/\delta}{h_f} \text{ and } T_{p,m} = T_{p,f} - \frac{Jh_{fg} + k_m(T_{f,m} - T_{p,m})/\delta}{h_p} \quad (1.12)$$

1.2 Research Gap and Objectives

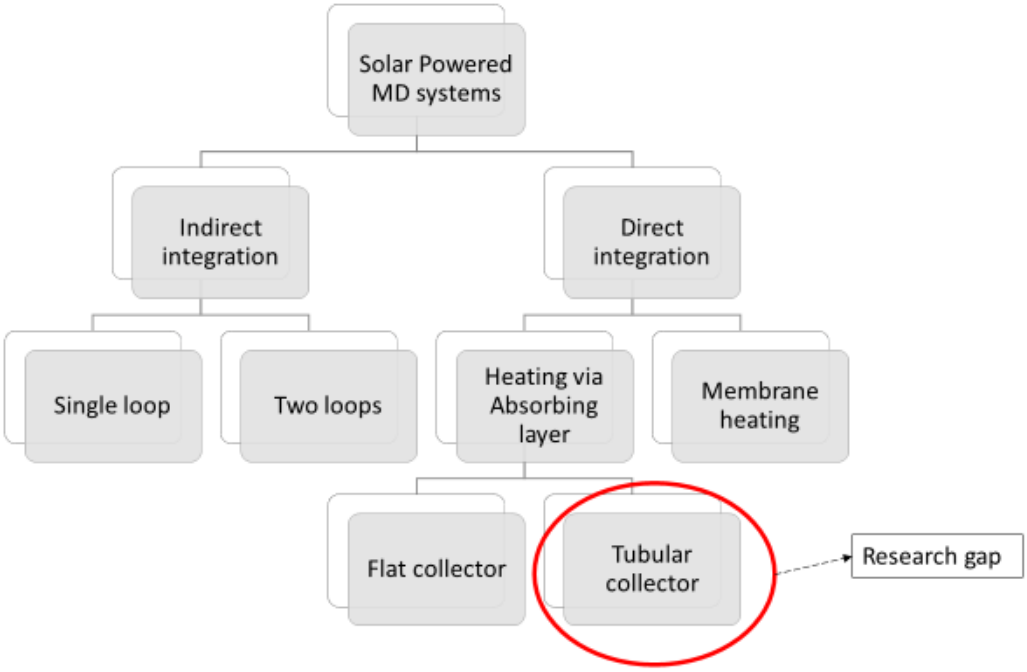

Figure 4. Integration of Solar Energy Membrane Distillation Systems

As discussed earlier, MD can utilize low–grade heat sources such as solar energy, geothermal energy or waste heat for its operation. The performance of solar–powered MD (SP–MD) desalination systems has been investigated by bench-scale and pilot–scale experiments and by theoretical models [19,20].

As shown in Figure 4, the integration of solar energy and the MD process can be categorized into indirect and direct integration:

1) **Indirect SP–MD:** in conventional solar–powered MD systems, two subsystems (an MD module and a solar thermal collector) are used. The feed water can be heated using [19–21]:
    a) A single loop: the feed water flows directly in the solar collector and then to the MD module.
    b) Two loops: a heat transfer fluid (HTF) is used in the solar collector. The feed water loop is integrated with the HTF via a heat exchanger.
2) **Direct SP–MD:** in recent years, researchers have suggested a direct integration system where the membrane itself is integrated within a solar collector aiming to have a more compact design. This can be done using a flat-sheet membrane within a flat-plate collector (Figure 5(a)), or a tubular membrane with a solar tube collector (Figure 5(b)). The feed heating mechanism can be classified into two methods:
    a) Heating via an absorbing plate: a top black plate absorbs radiation and transfers the heat to the feed water.
    b) Heating the membrane surface: a transparent glass is used in this module and the membrane itself is coated with an absorbing layer to heat up the feed water that flows above the membrane.

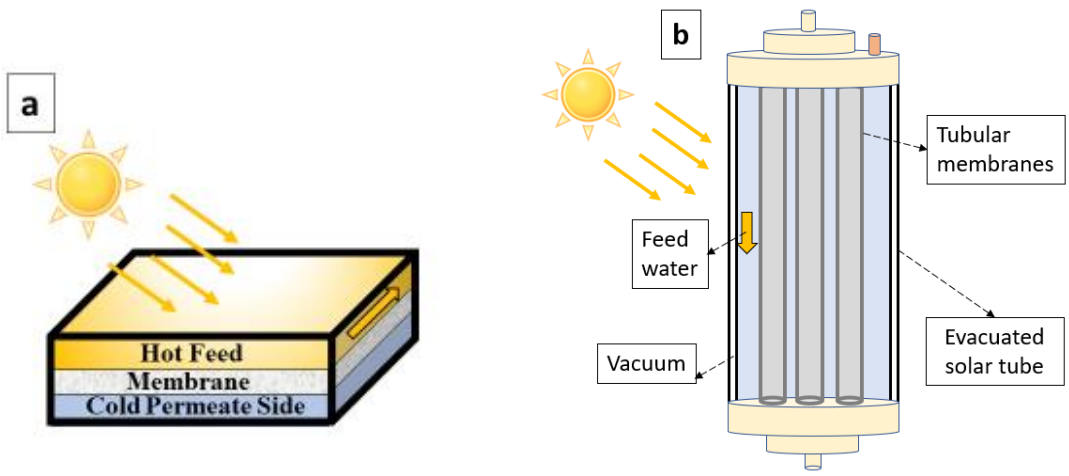

Figure 5. Conceptual Illustrations of Direct SP–MD Systems Using (a) Flat-sheet Membranes, and (b) Tubular Membranes.

So far, the direct SP–MD method has primarily been applied to flat-sheet membranes integrated within a flat–plate solar collector as shown in Figure 5(a). In other words, there has been little focus to study direct SP–MD systems using other types of membranes or solar collectors such as evacuated tube collectors. These collectors, generally speaking, are more efficient particularly in cold and/or cloudy conditions when compared to flat plat collectors [22].

Therefore, in view of the absence of intensive studies of such systems, **the main objective of this study** is to examine the feasibility of novel designs and processes of direct SP–MD modules that integrate *tubular* membranes (including hollow fibers or capillaries) inside a *tubular* solar collector working under different MD configurations and feed flow mechanisms. The study will be conducted through a largely experimental approach, but with appropriate application of theory to analyze the data and to suggest future directions for research.

The expected contributions of this research are to:

- Design and fabricate module structures that are practical and scalable for real–world application and have long–term stability.
- Test the modules in an indoor controlled environment and outdoors under ambient weather conditions.
- Investigate the use of different MD configurations (e.g. DCMD and VMD).
- Study the modules under different feed flow mechanisms (e.g. cross–flow and submerged).
- Obtain the optimum permeate production and thermal efficiency by varying the operation conditions, which may include varying radiation intensity, operating temperature, flow rates, feed concentrations, etc.
- Propose new techniques (e.g. ultrasound) to enhance the system's performance and efficiency.

1.3 Motivation and Potential Impact

1) Water scarcity is still a major challenge in the world and desalination, as a solution, is utilized mostly in rich countries [23]. MD is a promising technology in this industry, but it needs more improvements regarding energy use in order to be a more attractive option. Utilizing solar energy in a more efficient way can play a role in reducing primary energy use and consequently reduce the capital and operating costs of MD systems.
2) Remote communities that suffer from power and water shortages require sustainable methods to provide fresh water [19]. Other off–grid locations, such as oil and gas

extraction locations, produce a large amount of water that needs to be treated before disposal or injection [15]. Small–scale, stand–alone MD systems that directly utilize solar energy can be suitable for off–grid markets to treat brackish groundwater or seawater. These systems can be totally run by solar energy if solar photovoltaic (PV) panels are used to operate the circulating and/or vacuum pumps.

3) Brine disposal is a major environmental problem associated with large desalination plants. A recent UN–sponsored study suggested that four neighboring countries (Saudi Arabia, UAE, Kuwait and Qatar) are responsible for 55% of total global brine production, which might result in contaminating food chains and polluting the marine environment [23]. While toxic brine can be treated, those processes are technically complex and expensive in terms of capital cost and energy use. Thus, developing MD systems that use renewable energy sources can potentially play a role in addressing this issue since it can operate at high salinity. The integration of MD with conventional desalination systems has been studied by many researchers [7]. Several studies suggested that integrating MD technology with MED and OR systems to recycle the hot brine can increase the overall water production and energy utilization [6].
4) Most commercial membranes and modules that have been tested in the MD literature were designed for other filtration applications and not specifically made for MD processes [13,24]. MD technology has progressed slowly in comparison to other desalination technologies due to lack of appropriate commercial membrane types with acceptable flux rates [4]. Thus, it is important to propose designs to advance research and innovation in this field.

1.4 Potential Challenges

MD has some operational challenges such as temperature polarization, high specific energy, membrane wetting, scaling, and fouling, although to a lesser degree than RO systems. Those challenges slow down MD progress toward commercialization and wide applicability. I discuss below some challenges that may arise throughout the research project:

1) Operational challenges such as leakage and membrane damage are always expected in experimental work. Thus, it is important to fabricate and build a reliable module that efficiently integrates membranes inside solar collectors. This module must be made of materials that work under high temperatures, different flow rates, and high concentrations of saline water. The membranes must be glued and potted effectively to prevent any leakage or damages.
2) Thermal challenges such as temperature polarization is considered a limiting parameter in MD systems [18]. Other thermal issues we might face are thermal stratification and diurnal temperature. However, compared to other thermally driven desalination systems, MD is less sensitive to such temperature fluctuations and can operate in large temperature ranges of 40 to 90 °C [25]. So, it is important to maintain a uniform temperature distribution throughout the evacuated tube without thermal stratification, and to keep the temperature differential (< 20 °C) across the membranes.
3) A huge amount of MD research has focused on membrane wetting, scaling, and fouling. Fouling can cause pore blocking and foulant adsorption, leading to a decrease in performance over time [10,26]. In addition, Saffarini et al. noted that pore wetting and leakage are possible operational problems in SP–MD systems [19]. Those issues might

arise because of inappropriate pore size, pressure spikes, and deposit accumulation on membrane surfaces. Furthermore, it is not yet clear how direct solar radiation can affect the membrane characteristics over time.

4) Cost estimates of desalination systems and particularly in emerging technologies such as MD suffer from high degrees of inconsistency even for similar–size systems [2]. Thus, it can be challenging to conduct an accurate comprehensive economic analysis of SP–MD systems due to the absence of well–established data as well as the high uncertainty associated with the cost, performance, and lifetime of the membranes [10].

1.5 Dissertation Structure

This dissertation is divided into six chapters as follows:

Chapter 1 presented basic fundamentals of the research topic in this dissertation and the research gap in the field of solar-powered membrane distillation (SP-MD). In addition, the chapter discussed the research objectives and motivations as well as a few potential impacts and challenges.

Chapter 2 provides a comprehensive review of recent efforts that directly integrated solar energy with MD systems and discusses some limitations that should be addressed in future work.

Chapter 3 presents a novel direct solar-powered direct contact membrane distillation (DCMD) system, which integrates capillary membranes within an evacuated-tube solar collector.

Chapter 4 presents a novel, solar-heated, submerged vacuum membrane distillation (S-VMD) system that utilizes circulation and aeration as agitation techniques to enhance its performance.

Chapter 5 investigates the effects of applying low-power ultrasound in an S-VMD system working under different operating conditions to enhance the permeate flux and efficiency.

Chapter 6 discusses the conclusions based on the results presented in each chapter.

Chapter 7 outlines possible future work.

2 DIRECT SOLAR–POWERED MEMBRANE DISTILLATION: A REVIEW OF LITERATURE

Water desalination has become one of the viable solutions for water shortages in regions with limited natural resources. Yet, conventional desalination technologies require large amounts of energy, and are mostly powered by fossil fuels, which are expensive and linked to climate change [1,2]. Therefore, more attention has been paid to renewable energy as an alternative in desalination processes.

Among all applicable renewable energy resources, solar energy represents a promising option to utilize in desalination processes because of its high availability and its low operating and maintenance requirements. Despite these advantages, it should be clarified that solar desalination systems have not been widely used in the desalination industry, mainly because of the high cost and low water production when compared to large–scale conventional desalination systems [25]. However, solar–powered desalination can be attractive solutions in remote and arid areas particularly for small–scale systems.

Solar energy can be harvested in the form of electrical energy through photovoltaic (PV) modules or through direct absorption via solar thermal collectors. Conventional membrane–based technologies such as RO are usually coupled with PV systems, while thermal desalination technologies (MSF or MED) are integrated with thermal solar systems.

As membrane distillation (MD) represents a thermally driven, membrane–based desalination technology, and because the operating temperature of MD systems is well below the boiling point and MD can desalinate water over a wide range of feed temperature, solar energy can be integrated with MD systems mainly to heat up the feed water. The

performance of SP–MD desalination systems has been investigated by bench scale and pilot–scale experiments and by theoretical models [4,16,19,20,25].

As discussed in Chapter 1, the integration of solar thermal collectors and MD membranes can be direct or indirect. Previous reviews on SP–MD system have focused more on the indirect use of solar energy. In the absence of a comprehensive review regarding direct SP–MD systems, the main objective of this chapter is to provide an in–detail analysis of such systems. Specifically, it will focus on the different heating mechanisms in direct SP–MD and discuss their applicability and limitations in the real world based on the findings reported in the literature. Before that, it will be necessary to give a brief overview of indirect SP–MD systems.

2.1 Indirect SP–MD Systems

In this study, indirect SP–MD systems are used to refer to those systems in which the feed water is heated outside the MD module using a solar collector. In other words, a solar thermal collector is used as an alternative to an external electric heater or boiler to heat up the feed water. In these systems, two subsystems (an MD module and a solar thermal collector) are integrated.

It is worth noting that the vast majority of studies on SP–MD systems have focused more on the indirect use of solar energy. This is mostly because this method has been widely used in conventional thermal–based desalination systems (e.g. MED and MSF), and because it doesn't require module fabrication, and is easier to design and implement. As discussed previously in Chapter 1, the MD module and solar collector in indirect SP–MD

systems can be coupled in a single loop or in two loops as shown in Figure 6(a) and Figure 6(b), respectively.

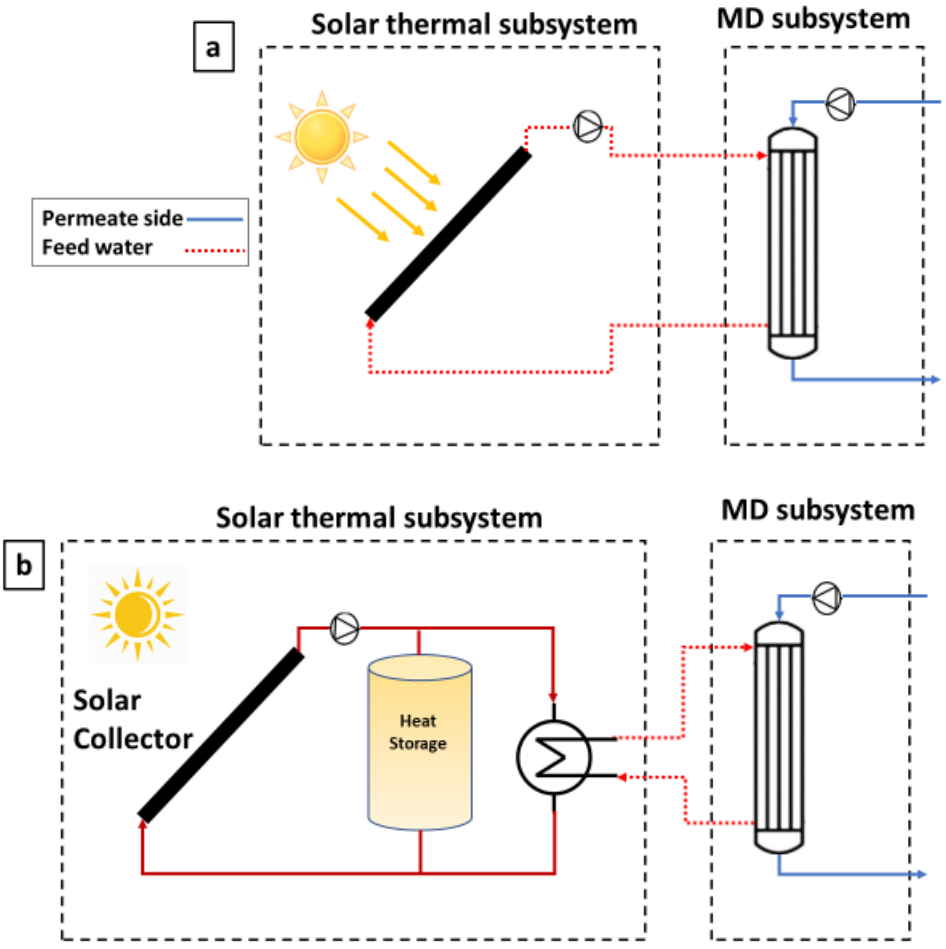

Figure 6. Indirect SP–MD System Using (a) a Single Loop, and (b) Two Loops.

In single–loop SP–MD systems, the feed water flows directly in the solar collector, and then is pumped to the MD module. This allows the feed water to harvest a larger amount of solar energy. However, solar collectors in single–loop systems tend to be more expensive because they must be made of corrosion–resistant materials such as CuNi in order to avoid scaling [27].

In two–loop SP–MD systems, a heat transfer fluid (HTF) flows in the solar collector and transfers the heat to the feed water via a heat exchanger. Although the feed water is not heated as much as in a single–loop system, cheap solar collectors that are commercially available can be used as the scaling mostly affects the heat exchanger, which is easier to clean [27]. Furthermore, the solar collectors in two–loop systems can be integrated with a heat storage unit to use it during the nighttime to ensure extended operating hours as shown in Figure 6(b).

In general, single–loop systems are preferred in small–scale MD units, while two–loop systems are mainly used in medium- to large-scale MD plants, which have been studied theoretically [20]. In both cases, the feed may run in a closed cycle (i.e. the outlet brine flows back to the feed container to recover some of the heat) or in an open cycle (i.e. untreated seawater or brackish water is used as the feed and the outlet brine goes to disposal).

Researchers have conducted bench–scale and pilot–scale experiments as well as theoretical models to test the performance of indirect SP–MD systems. Different types of solar collectors were used in these studies, including flat plates [28], evacuated tubes [29–31], parabolic troughs and solar ponds [32]. The studies were carried out using different MD configurations and membrane types. More information about these studies can be found in two review papers [19,20].

2.2 Direct SP–MD Systems

Because indirect SP–MD systems require more equipment, more space, and higher capital cost, recent studies have suggested a system that directly utilizes solar energy to

heat up the feed water inside the MD module aiming to achieve a more compact system suitable for small–scale MD applications with low cost and simple operation. So, instead of having two subsystems, the membrane is integrated with an absorbing surface into one unit that can heat and desalinate the feed water simultaneously. As a result, this will eliminate the need of using a separate solar system or a heat exchanger. This can minimize the capital cost of the system and reduce the heat loss due to recirculation.

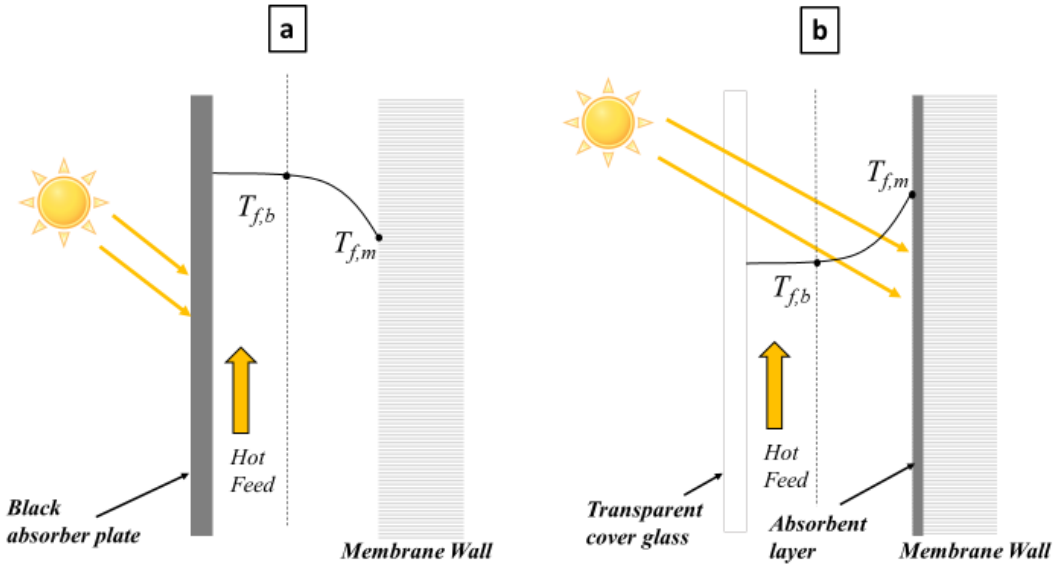

Figure 7. The Temperature Profile at the Feed Side in Direct SP–MD Systems (a) When the Solar Radiation Is Applied at an Absorbing Plate, and (b) When the Heating Is Applied at the Membrane Surface.

Direct SP–MD systems can be classified on the basis of heating mechanisms. The radiation can be absorbed either via an absorbing plate above the feed stream or via an absorbing coating layer on the membrane placed below the feed stream. The major difference between them is the temperature profile of the feed flow as shown in Figure 7. In the first method (i.e. heating via an absorbing plate) the feed temperature at the membrane $T_{f,m}$ is lower than at the bulk phase $T_{f,b}$. On the other hand, when the radiation is

absorbed by a coated membrane, $T_{f,m}$ is higher than $T_{f,b}$, eliminating the effect of temperature polarization. Thus, the latter method may achieve higher permeate flux when the operating conditions (inlet feed temperature, feed flow rate, …etc.) are the same. The following two sections will discuss previous studies that have implemented this technique.

2.2.1 Heating Via Absorbing Plate

Most of the work related to this type of systems focused primarily on the use of flat-sheet membranes as shown in Figure 5(a). The concept of these modules is very similar to flat–plate solar collectors used for domestic hot water systems. The module is covered by a glazed glass that allows solar radiation to penetrate to a dark–colored absorber plate, which in turn transfers the heat to the feed water. The hot feed water flows between the absorber plate and the hydrophobic flat sheet membrane. The vapor travels through the membrane to the permeate side at the bottom of the module. These types of modules were studied experimentally and numerically under the DCMD [33], AGMD [34], and VMD [35] configurations as shown in Figure 8.

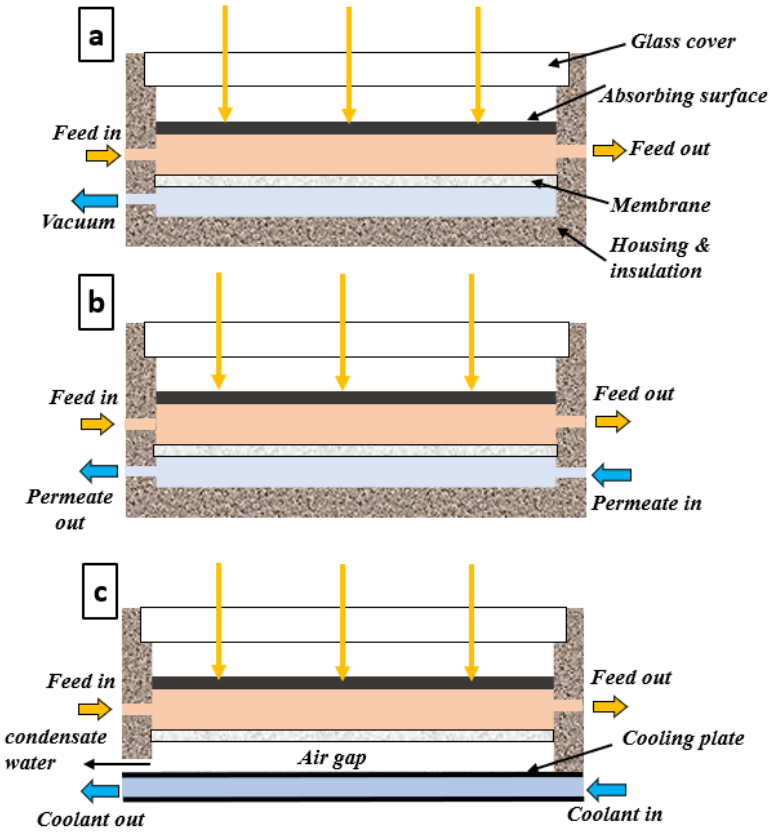

Figure 8. Direct SP–MD Systems Equipped with an Absorbing Plate Working Under the (a) VMD, (b) DCMD, and (c) AGMD Configurations

2.2.1.1 Direct SP–MD Systems Equipped with an Absorbing Plate Working Under the DCMD Configuration

The performance of a flat sheet DCMD system using an absorber plate (Figure 8(b)) was studied numerically and experimentally using a solar simulator by Chen and Ho [33]. The study was based on the solar–assisted concept in which the feed water is heated outside the module, and solar energy is used as a secondary source to directly heat the feed water inside the module. The permeate flux of the module was investigated with and without the effect of direct heating to measure the performance enhancement of the DCMD process. The authors found that, under similar operating conditions, the permeate flux can be enhanced by direct heating up to 16% (from 5.5 to 6.4 $kg \cdot m^{-2} \cdot h^{-1}$) at a low flow rate and a

feed inlet temperature of 35 ^{o}C. This improvement rate diminishes as the feed flow rate increases, the feed inlet temperature increases, or the radiation heat flux decreases, even though the absolute value of permeate flux increases with higher inlet temperature and higher flow rate. The study found that solar heating can reduce the effect of temperature polarization. It also concluded that the system is still expensive in terms of water cost compared to conventional desalination systems.

2.2.1.2 Direct SP–MD Systems Equipped with an Absorbing Plate Working Under the AFMD Configuration

Summers et. al. studied the effect of direct solar heating on a bench–scale, flat sheet AGMD system using a solar simulator [34]. In this system, the vapor transfers to the air gap in the permeate side and condensates on a cooling copper plate as shown in Figure 8(c). The module was tested under two heating mechanisms: by applying radiation to a coated absorber plate, and to a composite membrane (with a layer of a solar absorbing hydrophilic polymer). A permeate flux of 0.1–0.3 $kg \cdot m^{-2} \cdot h^{-1}$, and a GOR of 0.2–0.3 was achieved. The low values of flux were caused by the high mass transfer resistance due to the air gap. Another reason for the flow flux can be explained by the fact that a very low feed flow rate was required to absorb enough radiation to increase the effect of temperature polarization.

2.2.1.3 Direct SP–MD Systems Equipped with an Absorbing Plate Working Under the VMD Configuration

A numerical model of small–scale, flat sheet VMD that directly utilizes solar energy (Figure 8(a)) was developed by Ma et al. [35]. They found that operating the system at

lower feed temperature continuously is more effective than running it periodically at higher temperatures in terms of the daily water production and energy use, even though the average permeate flux was higher in the latter approach. A daily water production of 2.8 kg and GOR of 0.71 was predicted based on a 0.35 m^2 membrane/collector area and 12 hours of operation. In a follow–up work [36], the authors integrated a heat pump to recover the latent heat of evaporation and to work as a vapor condenser. The simulation showed that the system can produce 3.7 kg of water per day using a membrane area of 0.18 m^2 and a photovoltaic module of 0.13 m^2.

2.2.1.4 Direct SP–MD Systems Equipped with an Absorbing Surface Using Evacuated Tubular Solar Collector

As shown in Figure 5(b), tubular solar collectors such as evacuated tube collectors (ETCs) can also be used in direct SP–MD systems with tubular membranes (hollow fiber or capillary membranes). ETCs are made of double–wall low emissivity borosilicate glass, where the outer wall is highly transmissive, and the inner wall is coated with a black layer to increase absorption across the entire solar spectrum. A vacuum between the two walls minimizes the heat loss to the surroundings. Li et al. studied a VMD system by inserting four 30–cm–long capillaries in an ETC [37]. Vapor passes to the inner cores of the capillaries and is transferred to condense outside the module. The system achieved a permeate flux of 7.5 $kg \cdot m^{-2} \cdot h^{-1}$ when $T_{f,b} > 60$ °C and the vacuum pressure was ~10 kPa. The authors estimated that a system with an absorbing area of 1.6 m^2 (using 16 ETCs) equipped with a total membrane area of 0.2 m^2 can produce 3.2 to 4.8 kg of fresh water per day.

The integration of a hollow fiber VMD system in the receiver tube of a compound parabolic concentrator (CPC) was suggested by Abdallah et al. [38]. The system can achieve a maximum permeate flux of 6.8 $kg \cdot m^{-2} \cdot h^{-1}$, 30% higher when compared to a non–integrated hollow fiber VMD system (i.e. having two separate subsystems: CPC and VMD module) under the same operating conditions. It is worth mentioning that a detailed heat and mass transfer analysis was not discussed, and the effect of heat loss by distillation in the integrated VMD module might not have been taken into consideration as others have noted [35]. In addition, a similar concept in which helical hollow fiber membranes inserted within a CPC was also proposed by Zrelli et. al. [39].

2.2.2 Heating Via A Coated Layer on The Membrane:

To overcome some of the challenges associated with absorbing plate heating, researchers have suggested heating the membrane itself to assist in the MD process. These membranes use either an absorbing layer or photothermal nanoparticles to absorb solar radiation and heat up the feed water at the membrane surface. Figure 7 showed schematically the temperature profile of the feed under this heating mechanism.

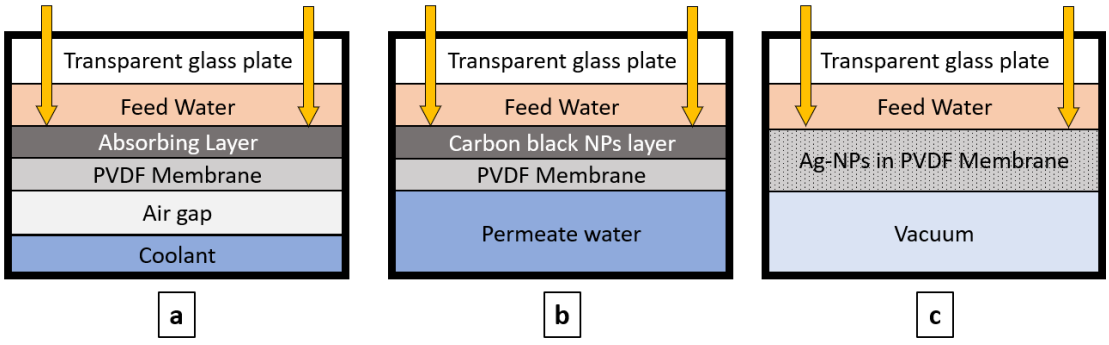

Figure 9. Direct SP–MD Systems Equipped with a Heated Coated Membrane Under the (a) AGMD, (b) DCMD, and (c) VMD Configurations.

The first study that suggested this approach (i.e. heating the membrane directly) was by Summers et. al. [34]. They used a two–layer membrane consisting of a black hydrophilic layer to absorb radiation on top of a hydrophobic PVDF membrane in an AGMD configuration (Figure 9(a)). They found that heating the membrane surface instead of heating via an absorbing plate was better in terms of permeate flux and energy efficiency. This was due to both the reduction in heat loss to the environment associated with the coated absorber plate as well as the reduction in the heat transfer resistance from the feed water to the membrane surface (i.e. no temperature polarization effect as shown in Figure 7).

The use of a nanophotonics–enabled membrane in a direct solar powered DCMD system was demonstrated by Qilin Li's group at Rice University [40]. The novel design was based on the *localized heating* concept, which uses light–absorbing nanoparticles to directly absorb solar illumination to heat up the feed water on the surface of the membrane instead of heating up the entire feed water. The group first used carbon black nanoparticles with a PVDF membrane as shown in Figure 9(b). In the bench scale–experiment under focused solar illumination, they achieved a permeate flux of 5.38 $kg \cdot m^{-2} \cdot h^{-1}$ with a solar efficiency of 20%. The flux in the outdoor experiment was 0.55 $kg \cdot m^{-2} \cdot h^{-1}$ with an efficiency of 54%. One important achievement in their experiment is that the feed and the permeate streams enter the module at the same temperature (20 ^{o}C). This means the feed is only heated inside the module. In another study, the same group used a PVDF membrane coated with carbon black nanoparticles and SiO_2/Au nanoshells [41]. The feed inlet temperature was 35 ^{o}C while the permeate temperature was 20 ^{o}C. The coated membrane

showed a 33% enhancement when compared to the uncoated membrane under simulated sunlight.

Politano et al. proposed a nano–enhanced membrane by inclusion of silver nanoparticles (Ag NPs) in a PVDF membrane as illustrated in Figure 9(c) [42]. The membrane was tested under the VMD configuration using simulated UV irradiation. The feed inlet temperature was 20 °C and the vacuum pressure was 2 kPa. The nano–enhanced membrane showed better performance in terms of efficiency and permeate flux (up to 11 times with a 25% Ag NPs membrane). The enhancement was attributed to the reduction in temperature polarization in the case with nano-enhance membrane.

2.3 Limitations and Conclusion Remarks

The concept of direct solar powered membrane distillation (direct SP–MD) has received little focus in the MD literature. This chapter reviewed and analyzed various studies on direct SP–MD systems in the last decade. It also identified the various ways the solar absorption mechanism is integrated with MD systems. Based on these studies, various real–world challenges associated with direct SP–MD systems have been identified:

1) **Preheating requirement:** It was observed that these systems generally do not use unheated feed water (i.e. the feed water doesn't enter the module at a low temperature of ~25 ^{o}C). Rather, it is either pre–heated using an external heater and the direct SP–MD module is used only to assist in the MD process, or the feed water flows in a closed loop so that the outlet feed from the module is stored in a container, which helps to recover some of the heat. Therefore, a real challenge in direct SP–MD systems is to use

cold (unheated) feed water and run it through the module to heat it up to a degree that allows the distillation process to take place.

2) **Lower flow rate requirement:** it was noted that for a directly heated SP–MD system to work only on solar energy, the feed flow rate must be reduced significantly in order to absorb the radiation flux. This creates a huge boundary layer resistance which increases the effect of temperature polarization (i.e. the feed temperature at the membrane surface is much lower than that at the bulk phase). Consequently, a significant reduction in the driving force to the vapor transfer is expected in these systems. However, this also means that less power is required to run the circulating pumps, which create an opportunity to use a small–size, inexpensive PV panel to run a DC pump.
3) **Scalability challenge:** So far, direct SP–MD systems were either analyzed numerically or experimentally studied on bench–scale units. The water production per unit of solar absorbing area was found to be relatively lower when compared to the indirect SP–MD systems or other solar powered desalination technologies. Thus, direct SP–MD systems still have a long way to be implemented as a stand–alone, large–scale desalination plant. However, it can be a promising option to provide water as a compact small–scale desalination unit in remote off–grid areas.
4) **Long–term uncertainty:** Unlike indirect SP–MD systems, the performance of direct SP–MD systems was not studied for an extended period of time. In fact, the studies were either conducted indoor using a solar simulator or outdoor environment for a few hours. So far, the long–term performance of a direct SP–MD system using real feed water (e.g. seawater or brackish water) has not been studied. In such cases, there is a

high risk of scaling on the membrane surface if antiscalant is not used. This could affect the flux and the water quality and reduce the membranes' lifespan. In indirect SP–MD systems, however, this problem is less significant as the scaling mostly affects the heat exchanger or the solar collector, which are easier to clean

5) **High cost:** both direct and indirect SP–MD systems suffer from high cost of water production when compared to other mature desalination technologies. The high cost can be justified if the system is implemented as a small–scale unit to provide water in off–grid areas with high shortages, or if it is used to treat hypersaline water where other technologies can't be used.

3 DIRECT SOLAR–POWERED DCMD SYSTEM USING EVACUATED TUBE COLLECTOR[1]

Membrane distillation (MD) is a technology that combines thermal–based and membrane–based desalination processes and has attracted increasing interest recently [4]. MD uses feed water at low temperatures and so it can utilize low–grade heat sources such as solar energy [5]. Solar–powered MD (SP–MD) can be classified into two main categories: indirect and direct. In indirect systems, the feed water is heated *outside* the MD module using a solar collector [16,25]. In direct systems, the membrane is integrated within a solar collector and the feed water is heated inside the MD module. So, instead of having two subsystems, the MD module alone will heat and desalinate the feed water at the same time. As a result, this will eliminate the need for a heat exchanger and a separate solar system, thus minimizing the capital cost of the system and reducing the heat loss.

Most of the work related to direct SP–MD systems focused primarily on the use of flat sheet membranes integrated with a flat–plate solar collector. Only one study that considered the use of a tubular collector in direct SP–MD systems. So far, no study has investigated the technical feasibility of a direct SP–MD system that uses a tubular collector working under the DCMD configuration. In fact, DCMD may offer several advantages over VMD in this type of system. First, DCMD requires less equipment compared to VMD

[1] Published in *Desalination* as:
Bamasag, A., Alqahtani, T., Sinha, S., Ghaffour, N., & Phelan, P. (2020). Experimental investigation of a solar-heated direct contact membrane distillation system using evacuated tube collectors. *Desalination*, *487*, 114497.

which needs a vacuum pump and an external condenser, resulting in a lower initial cost for a small–scale SP–MD system. Second, DCMD consumes less electric energy, making it cheaper to operate and more attractive in off–grid areas where a small solar photovoltaic (PV) can be used to provide electricity. Third, although VMD may achieve a higher permeate flux than DCMD, it suffers from high risk of membrane pore wetting which leads to a reduction in the quality of produced water over time. This means the membranes may need to be replaced more often than in DCMD.

The main aim of this study is to design and test the functionality of an innovative SP–MD module that utilizes solar energy *directly* using the DCMD process. The proposed design integrates hydrophobic hollow fiber membranes into an evacuated–tube solar collector (ETC). The system can therefore operate without the need for an external heat exchanger as the heating process is taking place inside the module, and it also does not need a condenser as the vapor condenses in the permeate cold water.

The outcomes of this work will provide a preliminary understanding of the effect of direct heating via solar radiation on the performance of the MD module. It is expected that, under similar operating conditions, applying direct radiation to the feed water inside the module would enhance J when compared to the case without applying radiation. This is because the feed water is being heated while it is flowing on the shell side of the module and thus the temperature drop of the feed water is reduced and the local flux along the module is increased.

The small–scale system might be an effective technique to provide fresh water in off–grid or remote coastal areas. It is also suitable to be integrated with conventional small–scale water treatment units to treat the produced brine since it can work with high

concentration water. The system can be integrated with a PV panel to provide the electricity required for operating the circulating pumps.

3.1 Materials and Methodology

3.1.1 The Design of The Direct SP–MD Module

The fundamental concept of the module design is to use a solar evacuated–tube collector (ETC) as the housing for the hollow fiber MD membranes. The proposed direct SP–MD module works as a shell–and–tube heat exchanger where feed water (seawater or brackish water) flows on the shell side of the module, and the permeate water flows on the tube side. The evacuated solar tube consists of two borosilicate glass tubes, fused together under a slight vacuum to minimize overall heat loss to the environment. Moreover, the inner tube is blackened in order to increase absorption across the entire solar spectrum and to provide uniform heating of the feed water. The black coating also blocks the visible spectrum of sunlight, which prevents algae growth and associated membrane fouling potential. Two evacuated tubes with different lengths (0.5 m and 1.8 m) were used in this study.

Figure 10 shows a schematic and a photograph of the proposed design of the direct SP–MD module. The permeate cold water enters the SP–MD module from the top cap, and then flows inside the fibers. The water is collected at the bottom cap and carried outside the module taking a U–shape path as shown in Figure 10. On the other hand, a tube is placed in the middle of the module to carry the feed water to the bottom of the solar tube. The feed water then moves up on the shell side of the module until it reaches the top and then it flows outside the module.

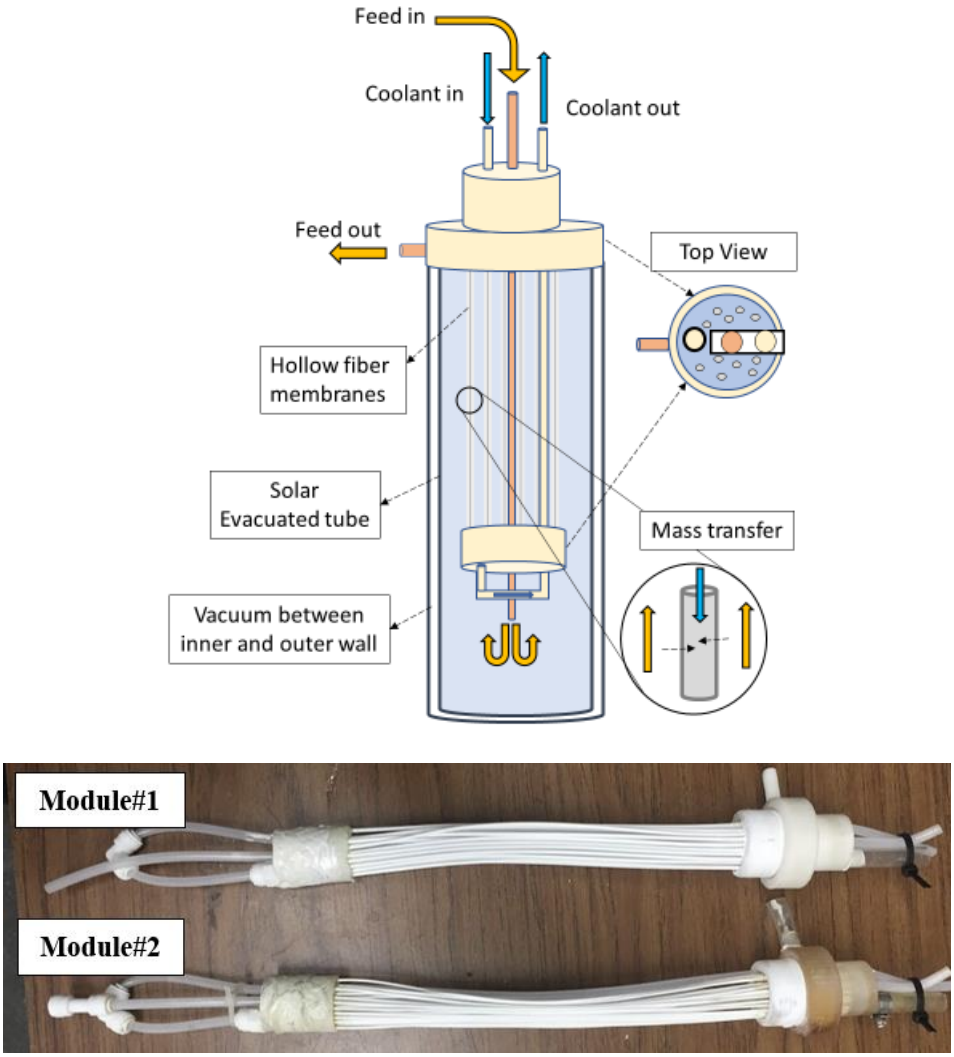

Figure 10. A Schematic Diagram (Top), and a Photograph (Bottom) of the ETC–MD Modules.

Placing the hollow fiber membranes inside the solar evacuated tube in a proper and efficient way was the most challenging task. The membranes were carefully placed and potted using epoxy resin in the top and bottom caps. In addition, since commercially available ETCs come with only one open end, it was challenging to design a hollow fiber module where the inlet and the outlet of the feed and permeate streams are placed in one side of the tube. This design may cause some heat loss in the feed side due to the thermal

exchange between the inlet and outlet feed streams. So, fabricating a solar evacuated tube with two open ends (i.e. similar to standard shell–and tube modules) should be considered in future work to achieve a more efficient MD operation. One advantage of the present design, however, is that it is very easy to take the membrane outside the module to clean the fibers or to check for any changes in the membrane's characteristics in case of wetting, scaling, or leakage events.

Table 2 Characteristics of the Direct SP–MD Modules

	Module# 1	Module# 2
Membrane manufacturer	Microdyn–Nadir	3M
Membrane material	Polypropylene	Polypropylene
Pore size (μm)	0.2	0.2
Porosity	0.7	0.7
Tortuosity	1.4	1.4
Fiber inner diameter (mm)	1.8	1.2
Fiber outer diameter (mm)	2.7	1.8
Fiber thickness (μm)	450	300
Number of fibers in each module	27	36
Packing Factor	0.10	0.06
Length of fibers (mm)	240	255
Total membrane surface area (m^2)	0.037	0.035
Solar tube inner diameter (mm)	44	
Solar tube outer diameter (mm)	58	
Solar tube length (mm)	500 and 1800	

Two direct SP–MD modules were manufactured using two types of commercially available polypropylene (PP) membranes. They both have a mean pore size of 0.2 μm and a porosity of 70% but have a different inner diameter and wall thickness. Table 2 summarizes the characteristics of the two modules and their corresponding hollow fiber membranes.

3.1.2 Experimental Setup and Procedure

3.1.2.1 Indoor Testing Under Steady–State Operating Conditions

The objective of the indoor testing is to gain a fundamental idea of the performance of the proposed direct SP–MD module under steady–state conditions. In other words, the permeate flux of the module is obtained when the flow rates and inlet temperatures of both the feed and permeate streams are fixed at specific values for an extended period of time. The permeate flux is also measured when a constant radiation heat flux is applied on the module under the same steady–state operating conditions in order to determine any improvement in the performance after heat flux is directly applied on the MD process.

A schematic representation and a photograph of the indoor experimental setup are shown in Figure 11. The desalination experiments were carried out using aqueous sodium chloride solution (using lab grade NaCl supplied by The Science Company) at concentrations of 30–35 g/L (TDS of standard seawater) as feed water. The feed water in this experiment flows in a closed loop, meaning that the brine coming out of the module circulates back to the feed tank.

The hot saline water circulates on the shell side of the module and the cold permeate water circulates on the tube side in a counterflow mode under controlled flow rates using two peristaltic pumps (Thermo Scientific FH100 Peristaltic Pump). The permeate inlet temperature $T_{p,i}$ was fixed at room temperature (22–24 °C) using a chiller. The feed inlet temperatures $T_{f,i}$ were varied (at 45, 55, and 65 °C) using a circulating water bath (Thermo Haake DC10 circulator with a resolution of ± 0.1 °C). The temperatures of the inlet and outlet were continuously recorded using calibrated K–type thermocouples connected to a

data acquisition system (National Instruments, cDAQ–9171). A laboratory scale (± 0.01 g) was used to measure the increase of the mass in the permeate container over time

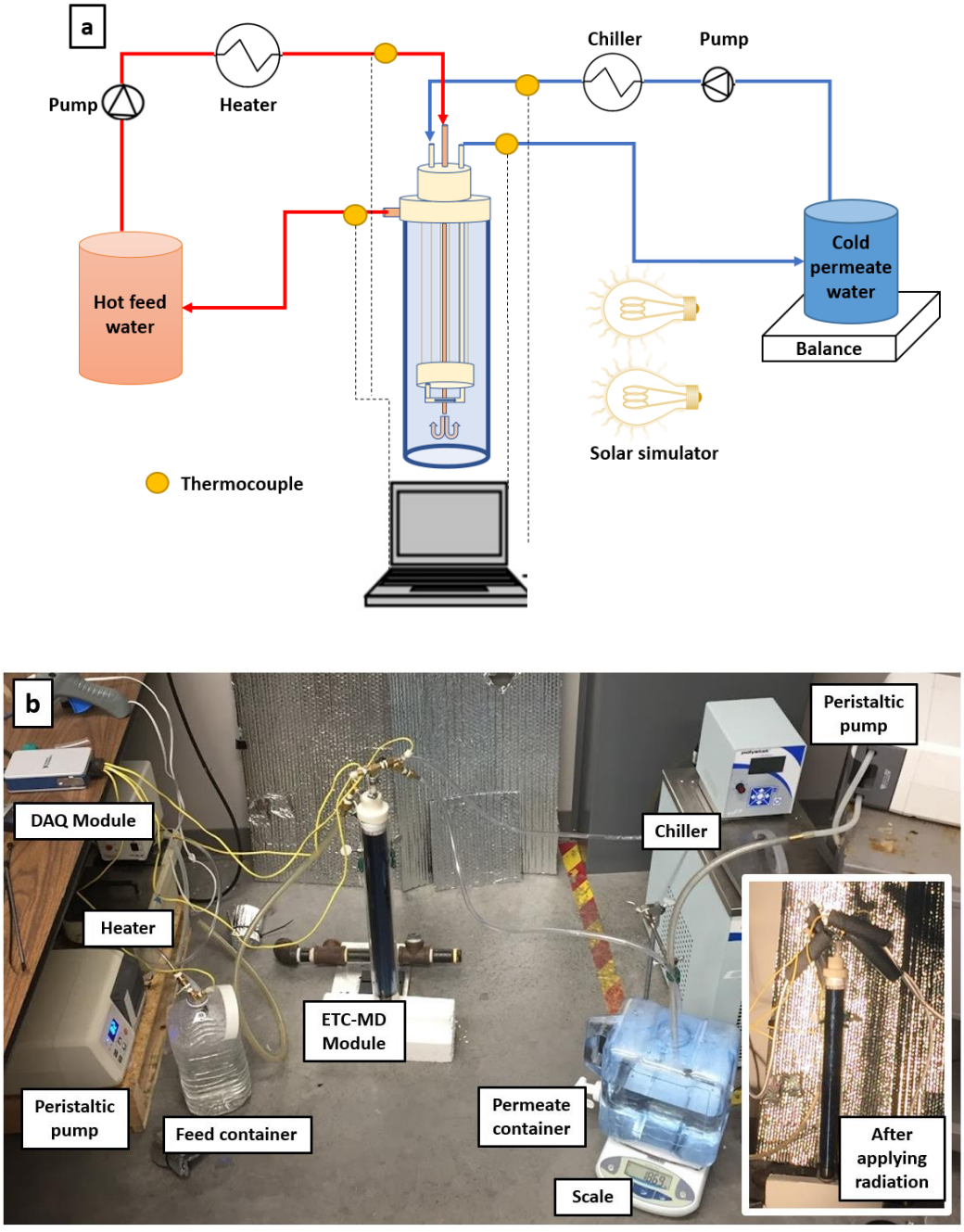

Figure 11. (a) A Schematic Diagram and (b) a Photograph of the Indoor Experimental Setup.

The flux was obtained by measuring the change in the permeate tank's weight every 10 minutes and dividing it by the membrane surface area as follows:

$$J_{measured} = \frac{\Delta m_d}{A_m \Delta t} \tag{3.1}$$

where $J_{measured}$ is the measured permeate flux ($kg \cdot m^{-2} \cdot h^{-1}$), Δm_d the change in the permeate tank mass (kg), A_m the membrane area (m^2), and t the sampling period (h).

The radiation heat flux was achieved by using an artificial solar simulator made of two General Electric 1000W PAR64 halogen light bulbs. The solar simulator was placed 3 m from the solar MD module, in order to provide an average of 950 W/m^2 of radiation heat flux. The average radiation intensity was estimated using a pyranometer sensor from Apogee Instruments.

Every experimental run lasted between 80 to 100 minutes. The solar simulator is switched on in the middle of each experimental run in order to measure the permeate flux under radiation heat flux for the same operating condition. After each run, the quality of the permeate water tank is tested using a portable electrical conductivity meter (HM EC–3), to measure any changes in the water salinity due to the membrane's wetting.

3.1.2.2 Outdoor Testing for Daily Operation

The direct SP–MD module was also investigated under ambient sunlight to determine the daily performance of the system. In this test, the electric heater (i.e. the water bath in the indoor testing) is eliminated, and all heating energy is provided by solar energy. Moreover, instead of using a simple tank for the feed water, another ETC (not equipped with a membrane) is placed next to the direct SP–MD module to function as a feed water

storage/container. This minimizes the heat loss to the surroundings, and at the same time, provides sufficient heating that can recover some of the energy loss due to the distillation effect in the direct SP–MD module.

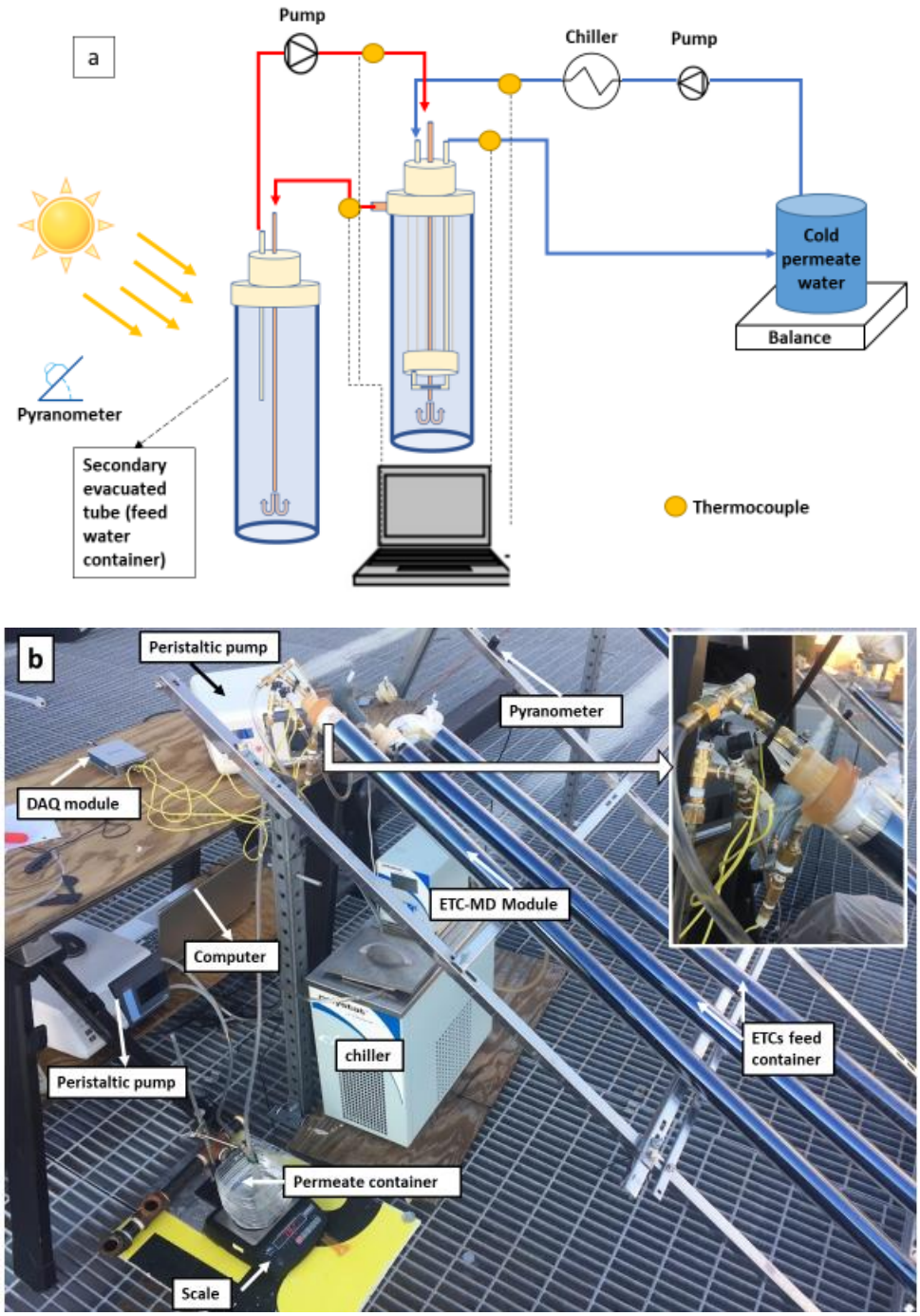

Figure 12. (a) A schematic Diagram and (b) a Photograph of the Outdoor Experimental Setup.

The daily performance enables a preliminary understanding of the potential long–term operation of the direct SP–MD system. Figure 12 shows a schematic illustration and a photograph of the outdoor setup.

The outdoor experiments were performed during the fall of 2019 in Tempe, Arizona, USA (latitude: 33.43°; longitude: –111.96° and altitude of 1132 ft above sea level), where most of the solar energy is gained between 8:00 AM and 4:00 PM during the fall season. The tilt angle of the module was set at 36°. A pyranometer sensor was placed next to the direct SP–MD module at the same tilt angle to record the solar intensity.

3.1.3 Performance and Uncertainty Analysis

One parameter that is usually used to evaluate the performance of MD processes including solar–powered MD (SP–MD) systems is the gain output ratio (*GOR*) [20,43]. The *GOR* measures how well the input energy is utilized for water production. It is defined as the ratio of the heat required to evaporate the distillate water to the total heat input by solar radiation or any other external heater. In other words, it is the ratio of the useful energy (i.e. the energy required to evaporate the distillate water) to the total energy input as shown in the energy balance diagram in Figure 13. The gain output ration (GOR) can be expressed mathematically as:

$$GOR = \frac{\dot{m}_d h_{fg}}{IA_a + \dot{Q}_{in}} \tag{3.2}$$

where $\dot{m}_d$ is the water production rate (kg/s), h_{fg} the latent heat of water (J/kg), I is the measured solar intensity (W/m^2), A_a the solar projected area (m^2), and Q_{in} the heat input from other sources (W).

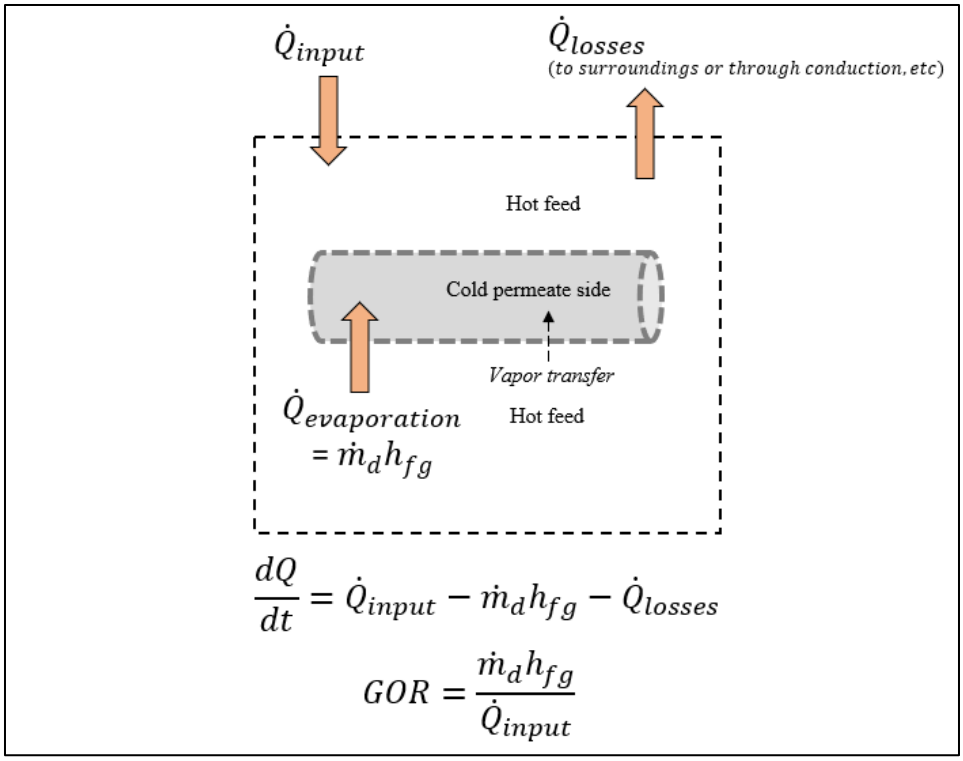

Figure 13. A Simplified Energy Balance Diagram in an MD Process.

To assure a high level of confidence (~95%), expanded uncertainties were calculated [44,45]. In this method, individual uncertainties from different sources are estimated and combined in each measurement. Table 3 shows the uncertainty analysis for different measurements. The uncertainty in the permeate flux in the indoor test is a combination of the uncertainty in the weight measurement and the standard deviation of the mean of four repeated readings (the uncertainties of membrane area and time are neglected). Moreover, the uncertainty in *GOR* is a combination of uncertainties from weight measurement and heat input.

Table 3 Uncertainty Analysis

Source of uncertainty	Weight (g) [1]			Flow rate (ml/min)			Radiation intensity (%)			Temperature (°C)		
	Value ±	Divisor	Standard uncertainty	Value ±	Divisor	Standard uncertainty	Value ±	Divisor	Standard uncertainty	Value ±	Divisor	Standard uncertainty
Calibration uncertainty							5.0	2	2.5	0.2	2	0.10
Resolution [2]	0.05	√3	0.03	5.00	√3	2.89				0.1	√3	0.06
Effect of wind [2][3]	0.50	√3	0.29									
Combined standard uncertainty			0.29			2.89			5.0			0.12
Expanded uncertainty *u*			0.58			5.77			5.0			0.23

(1) In the indoor test, the standard uncertainty of the mean of repeated readings is also considered.

(2) Here rectangular probability distribution is assumed and the (±) half-width divided by √3 is used.

(3) This is only applied in the outdoor test analysis.

3.2 Results and Discussion

3.2.1 Indoor Experiments Under Steady–State Conditions

In the indoor experiments, the two direct SP–MD modules in Table 2 were tested using a 50–cm–long ETC. The permeate flux was obtained under different steady–state operating conditions. The feed inlet temperature $T_{f,i}$ was varied between 45 °C and 65 °C, while the permeate inlet temperature $T_{p,i}$ was kept at 22 °C. The feed flow rates $\dot{m}_f$ were controlled under two conditions: 480 mL/min (~0.008 kg/s with a water velocity of 0.006 m/s) and 1250 mL/min (~0.02 kg/s with a water velocity of 0.013 m/s), while the permeate flow rate $\dot{m}_p$ was kept constant at 480 mL/min (with an equivalent water velocity of 0.11 m/s) in all cases. All experimental data were taken with and without the effect of direct radiation.

3.2.1.1 The Effect of the Feed Inlet Temperature and Flow Rate

Figure 14(a) and Figure 14(b) shows the permeate flux as a function of feed inlet temperature under different feed flow rates, for Module#1 and Module#2, respectively. As expected, higher feed inlet temperatures lead to higher permeate flux. This is because the

vapor pressure increases exponentially with temperature, which in turn increases the flux driving force as described in Eq. (1.1). For Module#1, while $J_{measured}$ is negligible at a feed inlet temperature $T_{f,i}$ of 45 °C at $\dot{m}_f$ = 0.008 kg/s (about 0.7 kg·m^{-2}·h^{-1}), $J_{measured}$ increased from 1.01 to 1.58 kg·m^{-2}·h^{-1} when $T_{f,i}$ increased from 55 to 65 °C when the radiation was not applied. For Module#2, under similar operating conditions, $J_{measured}$ was 1.97, 3.18, and 5.86 kg·m^{-2}·h^{-1} when $T_{f,i}$ was 45, 55, and 65 °C, respectively. Although both modules have similar characteristics in terms of membrane material, porosity, pore size, and effective membrane area, the membrane used in Module#2 has a thinner wall thickness, which explains the dramatic increase in flux compared to Module#1 under similar operating conditions. According to El–bourawi et al. [46], the mass transfer resistance is reduced with thinner membrane thickness, which leads to higher permeate flux.

Moreover, it is clear that increasing $\dot{m}_f$ from 0.008 to 0.02 kg/s caused an increase in $J_{measured}$. This was also expected because increasing $\dot{m}_f$ reduces the temperature drop (i.e. lower heat loss) in the feed along the membranes (Figure 15) which leads to a higher flux. Moreover, increasing $\dot{m}_f$ decreases the boundary layer resistance on the feed side, which reduces the effect of temperature polarization and leads to higher permeate flux [47]. After increasing $\dot{m}_f$, $J_{measured}$ increased to 1.13, 1.67, and 2.02 kg·m^{-2}·h^{-1} for Module#1, and to 2.38, 4.28, and 8.80 kg·m^{-2}·h^{-1} for Module#2, for $T_{f,i}$ = 45, 55, and 65 °C, respectively.

3.2.1.2 The Effect of Applying Direct Heating Via A Radiation Simulator

The permeate flux of both modules was obtained under the same steady–state operating conditions after applying direct radiation. An average radiative flux of 950 W/m^2 was provided by placing the solar simulator 3 m away from the module. As shown in Figure

14(a–b), it is clear that applying the radiation has a positive effect on $J_{measured}$ for both modules. For Module#1, at $T_{f,i}$ = 45 °C, $J_{measured}$ increased by 17% (from 0.69 to 0.80 kg·m^{-2}·h^{-1}) compared to that without radiation heat flux. The improvement percentage is 18% and 16% at $T_{f,i}$ = 55 °C and 65 °C, respectively as shown in Figure 14(a). For Module#2, at $\dot{m}_f$ of 0.008 kg/s, $J_{measured}$ improved by 13%, 16%, and 9% at $T_{f,i}$ = 45, 55, and 65 °C, respectively, as shown in Figure 14(b). In a previous work [48], an improvement percentage of 42% was achieved. However, the amount of radiation from the solar simulator was not measured during that experiment, but rather roughly calculated. After measuring it, the radiation was found to be over 2000 W/m^2, which indicates that the 42% improvement percentage is not realistic under natural solar intensity (<1200 W/m^2).

At a higher $\dot{m}_f$ of 0.02 kg/s, $J_{measured}$ also increased after applying direct radiation heating, but with lower percentage improvement compared to that at lower $\dot{m}_f$. For Module#1, the rate of improvement was 10%, 14%, and 7% at $T_{f,i}$ of 45, 55, and 65 °C, respectively. For Module#2, an even lower rate of improvement was observed under higher $\dot{m}_f$ (11%, 4%, and 3% for $T_{f,i}$ of 45, 55, and 65 °C, respectively). These results are in agreement with Chen and Ho [33], who concluded that at higher $\dot{m}_f$, direct heating has a lower effect on $J_{measured}$.

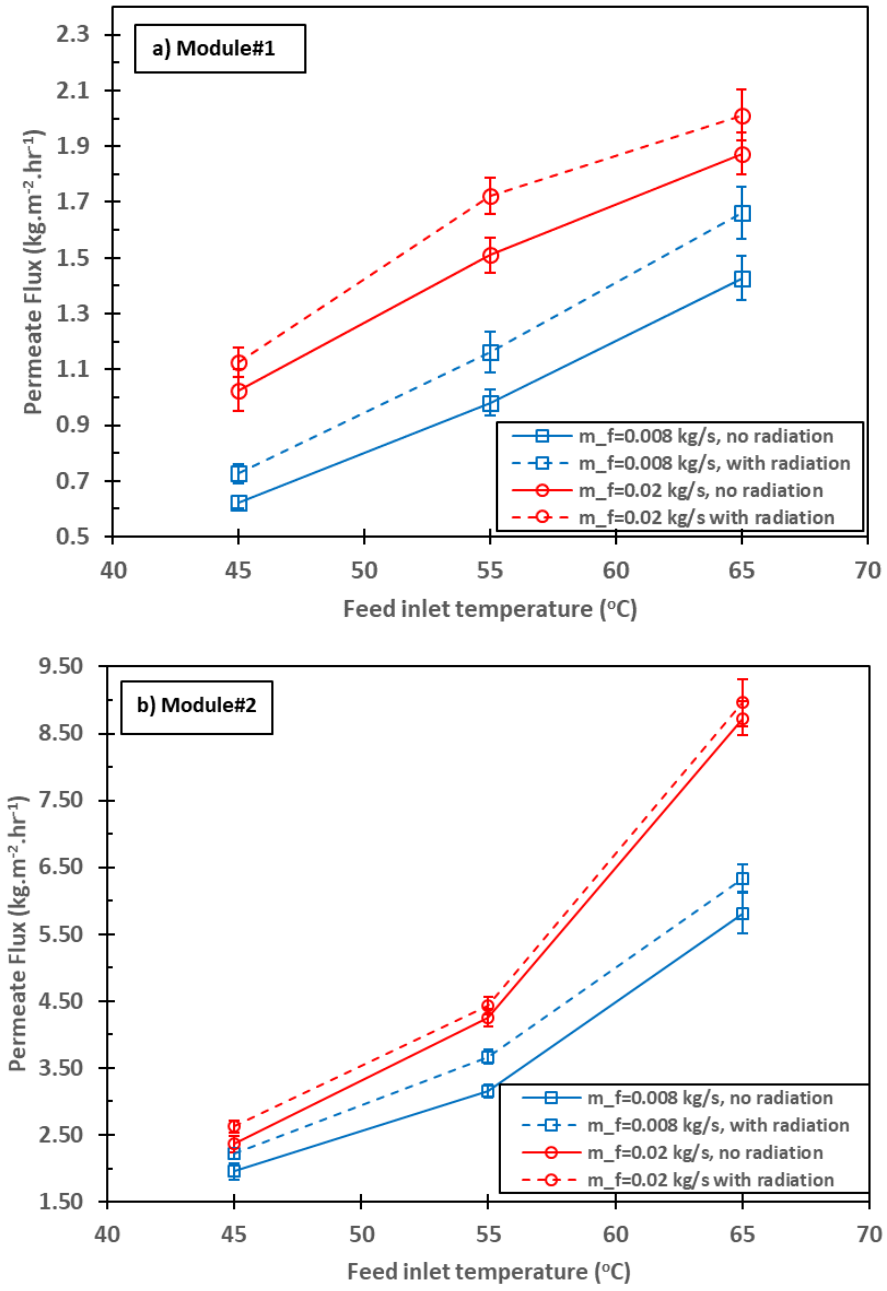

Figure 14 The Effect of the Feed Inlet Temperature on the Permeate Flux with and without Radiation Heat Flux for (a) Module#1 and (b) Module#2. (at Feed Concentration: 3.5%, $\dot{m}_f$=0.008–0.02 kg/s, $\dot{m}_p$=0.008 kg/s, $T_{p,i}$=~22 °C)

The increase in $J_{measured}$ after utilizing direct heating can be mainly attributed to the reduction in the temperature drop of the feed water along the module due to the additional

heat source. The differences between the outlet and inlet temperatures of the feed water ($\Delta T_f = T_{f,o} - T_{f,i}$) and that of the permeate water ($\Delta T_p = T_{p.o} - T_{p,i}$) are shown in Figure 15(a) for Module#1 and in Figure 15(b) for Module#2. It can be observed that ΔT_f generally increases at higher $T_{f,i}$. This can be attributed to the higher heat loss via conduction at higher $T_{f,i}$ as well as to the higher $J_{measured}$ at higher $T_{f,i}$, which creates greater cooling effect due to evaporation. Moreover, the values of ΔT_f were greater in Module#2 when compared to those in Module#1 at the same $T_{f,i}$ and $\dot{m}_f$. This is mostly because the membranes used in Module#2 have a thinner wall thickness, resulting in a greater conduction heat loss. Another reason is that Module#2 achieved higher permeate flux than Module#1 and that increases the effect of vapor vaporization in the feed side.

It is apparent that ΔT_f decreases after applying radiation heat flux on the direct SP–MD module for all experimental runs. For instance, for Module#1 at $T_{f,i}$ = 65 ^{o}C, ΔT_f is –4.9 ^{o}C without radiation and –4.0 ^{o}C with radiation at low flow rates, and is –2.3 ^{o}C without radiation and –1.5 ^{o}C with radiation at higher $\dot{m}_f$. This suggests that the temperature profile of the feed water along the membrane's length is expected to be slightly higher after applying the radiation, and consequently, the local permeate flux is expected to increase along the module as a result of the direct heating.

While it was reported that direct heating can minimize the temperature polarization effect in a flat sheet DCMD system [33], it is not yet clear how direct heating can influence temperature polarization in a tubular geometry equipped with hollow fiber membranes.

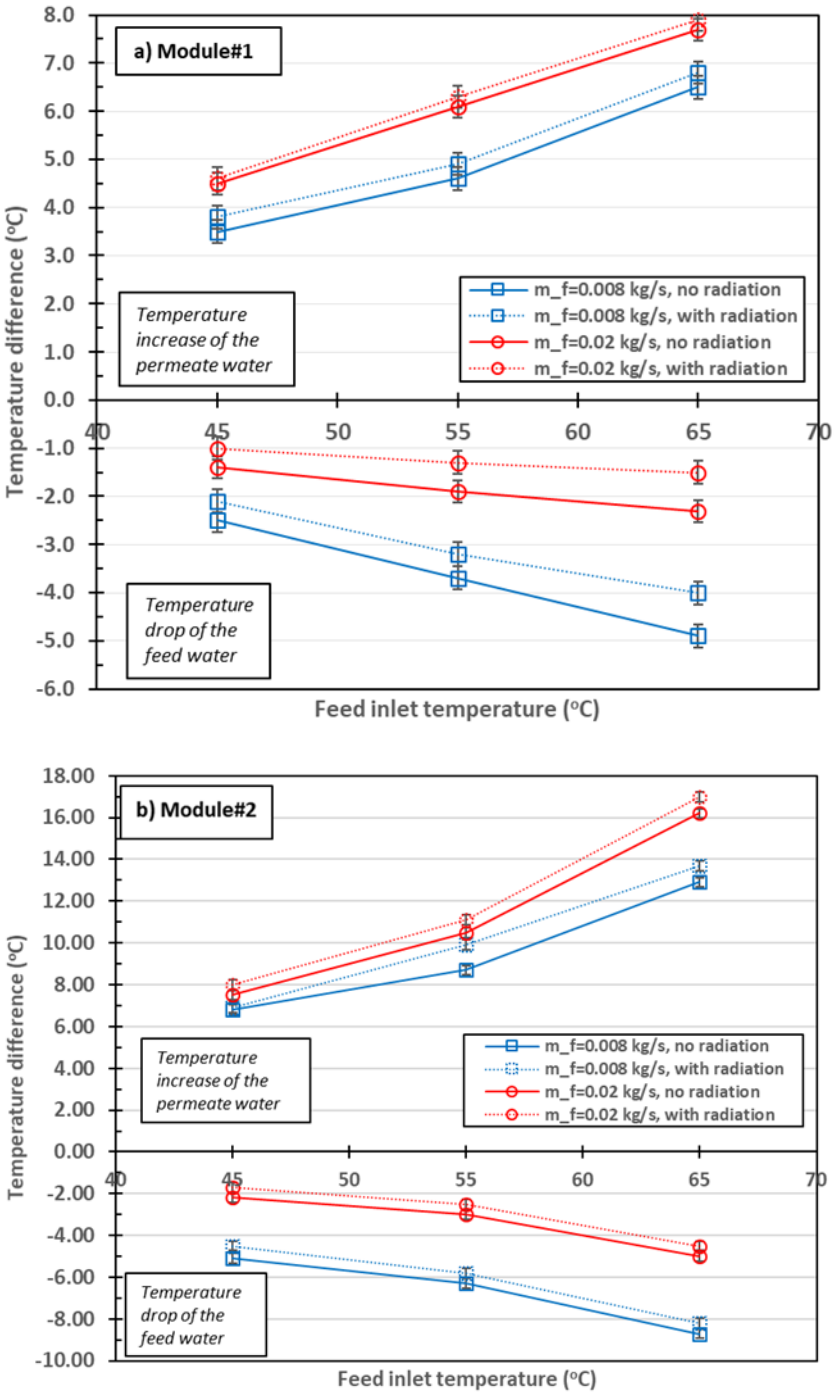

Figure 15. The Difference Between the Inlet and the Outlet Temperature of the Feed and the Permeate Streams with the Feed Inlet Temperature with and without Radiation Heat Flux for (a) Module#1 and (b) Module#2. (at Feed Concentration: 3.5%, $\dot{m}_f$=0.008–0.02 kg/s, $\dot{m}_p$=0.008 kg/s, $T_{p,i}$=~22 °C)

3.2.1.3 Performance Analysis

The *GOR* values of both modules under the previous steady–state operating conditions are shown in Figure 16. It can be observed that even though Module#2 required higher energy consumption due to higher heat loss, it achieved higher values of *GOR* compared to Module#1. This is mostly attributed to the higher rate of produced distillate water in Module#2.

It is also apparent that there is an improvement in *GOR* after applying the direct radiation heating. For Module#1, at $\dot{m}_f$ = 0.02 kg/s, the *GOR* varied between 0.19 to 0.22 without radiation and varied between 0.23 to 0.29 with radiation. At 0.02 kg/s, the *GOR* of Module#2 was in the range of 0.28 to 0.46 with no radiation, and 0.34 to 0.49 with radiation. The *GOR* also showed an improvement for both modules at $\dot{m}_f$ = 0.008 kg/s as shown in Figure 16. This implies that more distillate water can be produced per unit of energy input when solar energy is directly utilized in the process.

These results suggest that the direct SP–MD module can be used in "solar–assisted MD systems", where conventional heating sources or waste heat provides most of the heat input. Using "free energy" from the sun to assist in the MD process will lead to more efficient systems and can reduce the water cost. Moreover, the direct SP–MD design can be applied for multi–stage MD systems too. As shown in Figure 15, the temperature drop along one module can be reduced by 0.5 to 0.9 ^{o}C when solar radiation is applied directly. For an 8–stage MD system, for instance, this could mean that the outlet temperature in the final MD stage can be more than 4 ^{o}C higher if the system consists of if direct radiation is applied in the process. Consequently, more heating can be recovered from the outlet brine

in the final stage. Also, the average permeate flux will be higher in each stage because the inlet temperature in each stage is higher.

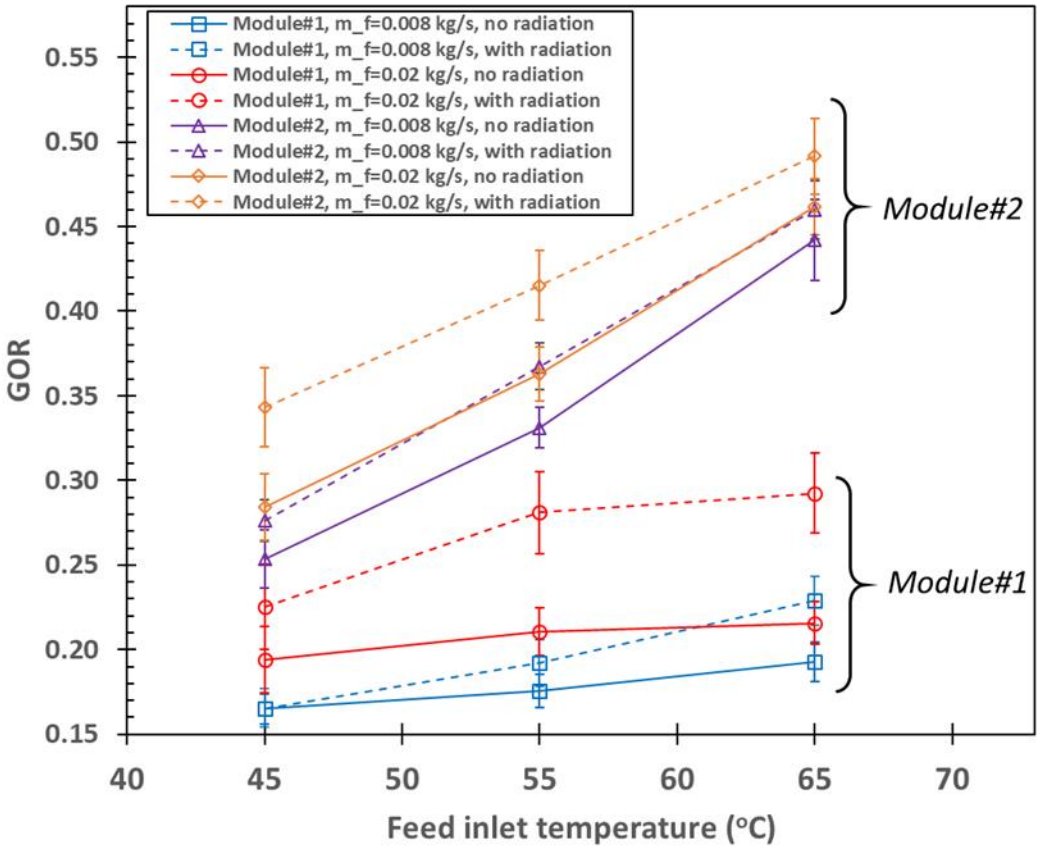

Figure 16. GOR for Module#1 and Module#2 as a Function of Feed Inlet Temperature with and without the Effect of Radiation. (at Feed Concentration: 3.5%, $\dot{m}_f$=0.008–0.02 kg/s, $\dot{m}_p$=0.008 kg/s, $T_{p,i}$=~22 °C)

3.2.2 Daily Performance for Outdoor Experiments

Outdoor testing of the direct SP–MD module was carried out to provide more insight into the effectiveness of this design and its applicability in real–world environments. Module#2 was used in this experiment because of its high permeate flux compared to Module#1. Longer ETCs (1.8m long) were used in the outdoor experiment in order to provide more exposure to solar radiation.

In the beginning, the direct SP–MD module and the other ETC container are filled with saline water. When the temperature of the feed water reaches 70–80 ^{o}C inside the tubes, the circulating pump for the feed water is switched on. When the system reaches a stable thermal state (i.e. the inlet and outlet temperatures in the direct SP–MD module are very close), the circulating pump for the cold permeate water is switched on, and the distillation process takes place. The permeate flux is obtained at 5–minute intervals using a laboratory scale.

Two scenarios were considered: (i) using two ETCs with a total absorbing area of 0.2 m^2 (where one ETC is equipped with membranes and the other ETC functions as the feed container), and (ii) using three ETCs with a total absorbing area of 0.3 m^2 (where one ETC is equipped with membranes and the other two ETCs work as feed containers). This will determine how much absorbing area is required in order to ensure that the input solar radiation is close to the heat loss due to the distillation process. For comparison, in their VMD experiment, Li et al. (2019) estimated that the ratio of the membrane area to absorbing area (A_m/A_a) is 1/10 [37].

3.2.2.1 Daily Testing Using Two ETCs

The first test was performed on September 28th, 2019. One ETC was used as a container for the saline water and another ETC was equipped with the membranes as shown in Figure 12(a). Figure 17(a) shows the solar intensity and inlet and outlet temperatures for the feed and permeate streams. Once the feed temperature inside the tube reached ~80 ^{o}C at 12:30 PM, the feed and permeate water started to circulate at a flow rate of 480 ml/min (0.008 kg/s). It can be seen that $T_{f,i}$ decreased dramatically to 58 ^{o}C after just 30 minutes of running the experiment. The high heat loss was due to the high distillation the module provided

during this period (~8 $kg \cdot m^{-2} \cdot h^{-1}$ at 12:30 and ~5 $kg \cdot m^{-2} \cdot h^{-1}$ at 1:00) as shown in Figure 17(b). The heat transfer rate from solar radiation to the feed water flowing at 0.008 kg/s was not enough to compensate for the heat loss caused by distillation. As a result, the experiment was stopped for ~10 minutes to allow the feed water to recover some of the heat loss in the first 30 minutes. Moreover, the flow rates were adjusted to 220 ml/min (~0.004 kg/s) in order to achieve more stable operation, and avoid a huge temperature drop in the feed side.

The operation was resumed when $T_{f,i}$ reached ~63 ^{o}C and stopped again when $T_{f,i}$ dropped to 53 ^{o}C (from 1:10 to 1:50 PM). During this period, $J_{measured}$ dropped from 4.2 to 2.6 $kg \cdot m^{-2} \cdot h^{-1}$. The pump was switched off for ~10 minutes every hour to ensure that the feed water recovers some of the heat loss. In the next two periods (from 2:05 to 2:55, and from 3:05 to 3:55) $T_{f,i}$ varied between ~60 ^{o}C to ~53 ^{o}C and $J_{measured}$ varied between 2.3 to 1.3 $kg \cdot m^{-2} \cdot h^{-1}$. The final period (from 4:10 to 5:15 PM) was mostly cloudy and $T_{f,i}$ dropped from ~56 ^{o}C to ~39 ^{o}C and $J_{measured}$ varied between 1.7 and 1 $kg \cdot m^{-2} \cdot h^{-1}$ as shown in Figure 17(b).

The cumulative water produced during the experimental run (4.75 hours) was about 340 g as shown in Figure 17(b). The daily *GOR* using Eq. (3.2) was found to be 0.18. This value takes into account the solar energy required to heat up the saline water before running the experiment. The total solar exposure was 6.1 kWh/m^2.

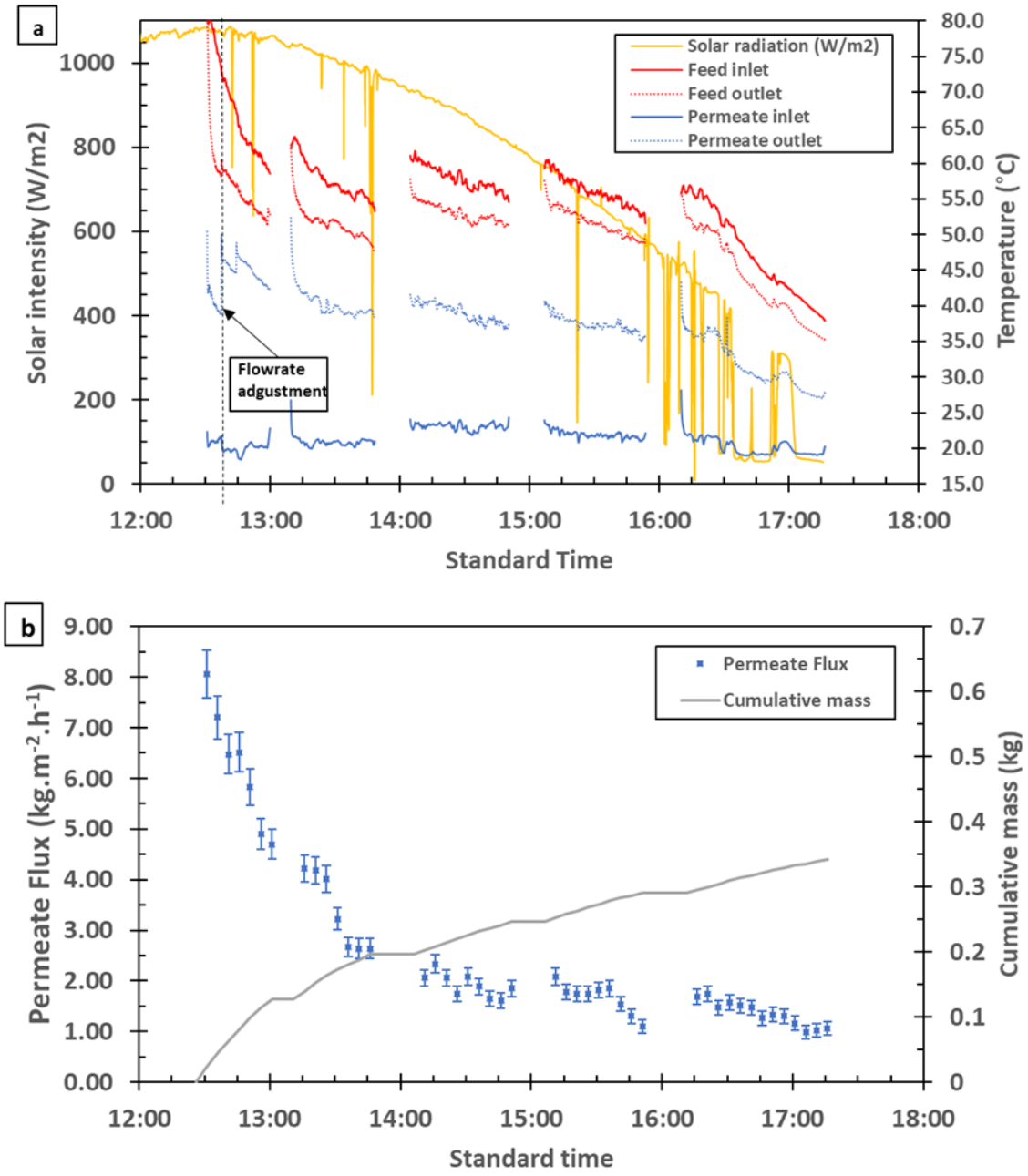

Figure 17. Outdoor Test Data on September 28th, 2019 for the Two ETC Configuration. (a) The Solar Radiation and the Inlet/Outlet Temperatures of the Feed and Permeate Water, and (b) the Hourly Cumulative Distillate Water and Permeate Flux.

3.2.2.2 Daily Testing Using Three ETCs

The second test was performed on October 1st, 2019. In this test, two ETCs were used as feed water containers instead of one ETC. In other words, the outlet feed water from the ETC–MD module goes through a two–stage heating process before entering the ETC–MD module again as shown in Figure 12(b). This allows the feed water to recover more of the heat loss during the distillation process and should reduce the rate of temperature drop of the feed water over time. The feed flow rate was kept at 0.004 kg/s in order to achieve quasi steady–state conditions and to be comparable with the daily test with two ETCs. Figure 18(a) shows the solar intensity and inlet and outlet temperatures for the feed and permeate streams, and Figure 18(b) shows the permeate flux and the cumulative water produced.

The experiment started at 11:00 AM when the feed water reached ~85 ^{o}C. In the first hour of the experiment, a 10 ^{o}C drop in $T_{f,i}$ was observed, and $J_{measured}$ in the range of 6.6 to 5.1 kg·m^{-2}·h^{-1} was obtained. It can be noted that the use of two ETCs helped to reduce the rate of temperature drop and achieve a more stable flux over time. It also helped to reduce the stop time to 5 minutes each hour, which was enough to check for the water quality.

From 12:00 to 1:00, $T_{f,i}$ decreased from ~75 ^{o}C to ~68 ^{o}C and $J_{measured}$ varied between 5.3 to 3.1 kg·m^{-2}·h^{-1}. This flux is relatively lower than that at $T_{f,i}$= 65 ^{o}C obtained in the indoor tests. To clarify, $J_{measured}$ at $T_{f,i}$ = 65 ^{o}C was found to be 5.9 to 8.8 kg·m^{-2}·h^{-1} in the indoor testing for Module#2. The lower $J_{measured}$ in the outdoor testing at higher $T_{f,i}$ is a result of the lower feed flow rate, as required by the system. This increases the effect of temperature polarization and reduces the permeate flux.

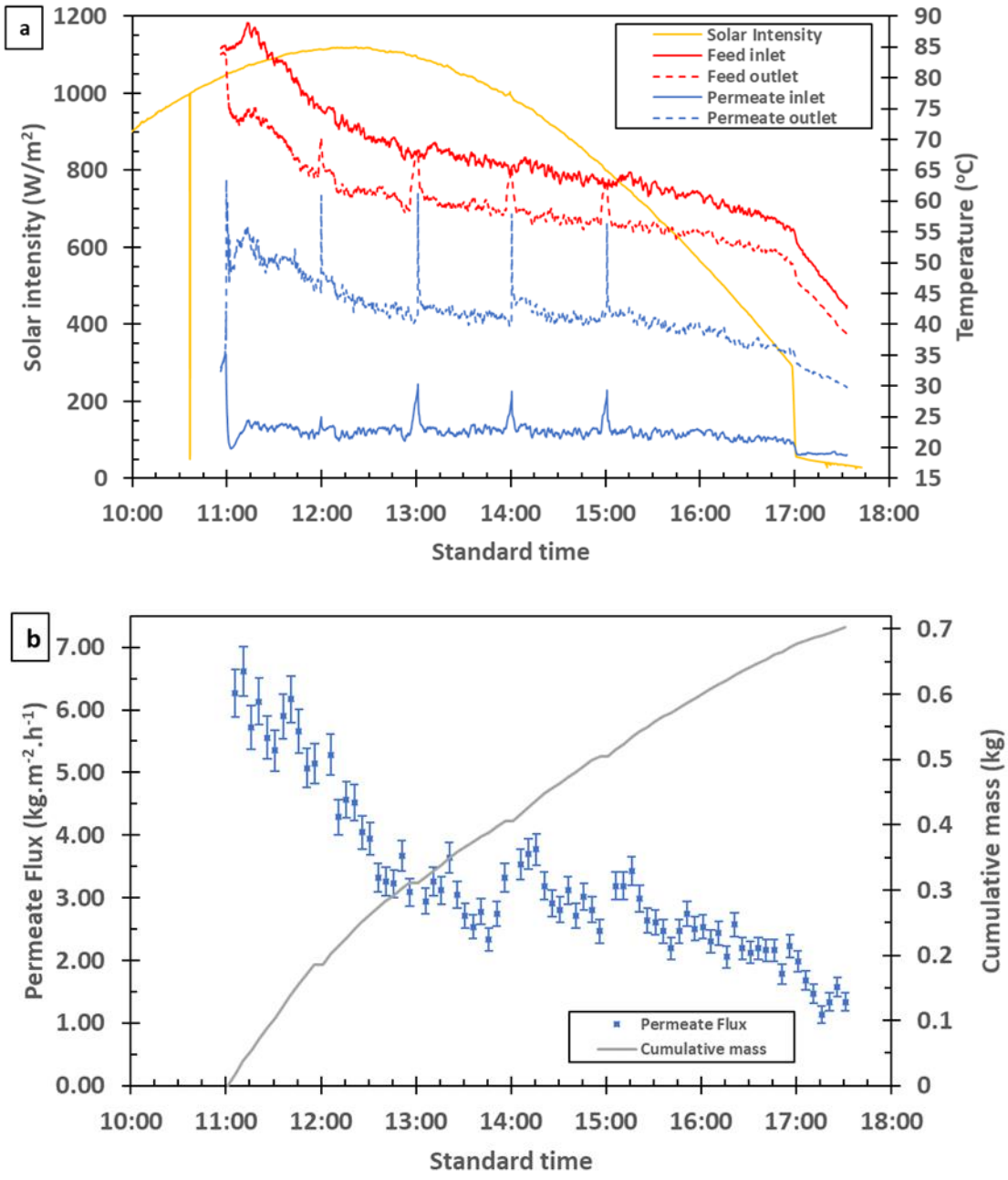

Figure 18. Outdoor Test Data on October 1st, 2019 for the Three ETC Configuration. (a) The Solar Radiation and the Inlet/Outlet Temperatures of the Feed and Permeate Water, and (b) the Hourly Cumulative Distillate Water and Permeate Flux.

From 1:00 PM to 4:00 PM, $T_{f,i}$ dropped from ~68 °C to ~60 °C (~8 °C in three hours), which shows the advantage of using a second ETC as a feed container. The permeate flux during this period was in the range of 3.7 to 2.5 kg·m^{-2}·h^{-1}. A weaker solar radiation caused

$T_{f,i}$ to drop from ~60 ^{o}C to ~54 ^{o}C from 4:00 to 5:00. After that, the radiation effect was absent due to shading and $T_{f,i}$ reduced to ~43 ^{o}C in just 30 minutes, and the experiment was stopped at 5:30 PM. A permeate flux in the range of 2.4 to 1.3 $kg \cdot m^{-2} \cdot h^{-1}$ was obtained during this period (4:00 to 5:30 PM).

As shown in Figure 18(b), the total water produced during the experimental run (6.5 hours) was 0.7 kg. According to Eq. (3.2), the system's daily *GOR* is 0.24 with a total solar exposure of 6.1 kWh/m^2.

The flux variation throughout the day shows that MD can operate with intermittent energy supply. Furthermore, it was found that this test (with a total absorbing area of 0.3 m^2) was more stable than the test with 0.2 m^2 absorbing area and experienced less temperature drop as shown in Figure 17(a) and Figure 18(a). This suggests that an acceptable ratio of membrane area to absorbing area (A_m/A_a) is ~1/9, which is close to the value (~1/10) estimated by Li et al. (2019) in their VMD experiment [37].

Based on these results, a small–scale system of 6–stage SP–MD modules can produce up to 4.2 L per day. The system consists of 18 ETCs connected in series, where 6 ETCs are equipped with membranes and the other 12 ETCs are used to heat up the feed water as illustrated in Figure 19. The feed water runs in series (i.e. the feed outlet from stage 1 will be the feed inlet in stage 2) until it reaches the last tube, where it is pumped again to the first stage. On the other hand, the permeate water enters the 6 stages in parallel (i.e. at constant temperature). The outlet warm permeate water can be used for domestic water heating (to cool down) before it circulates back to the system.

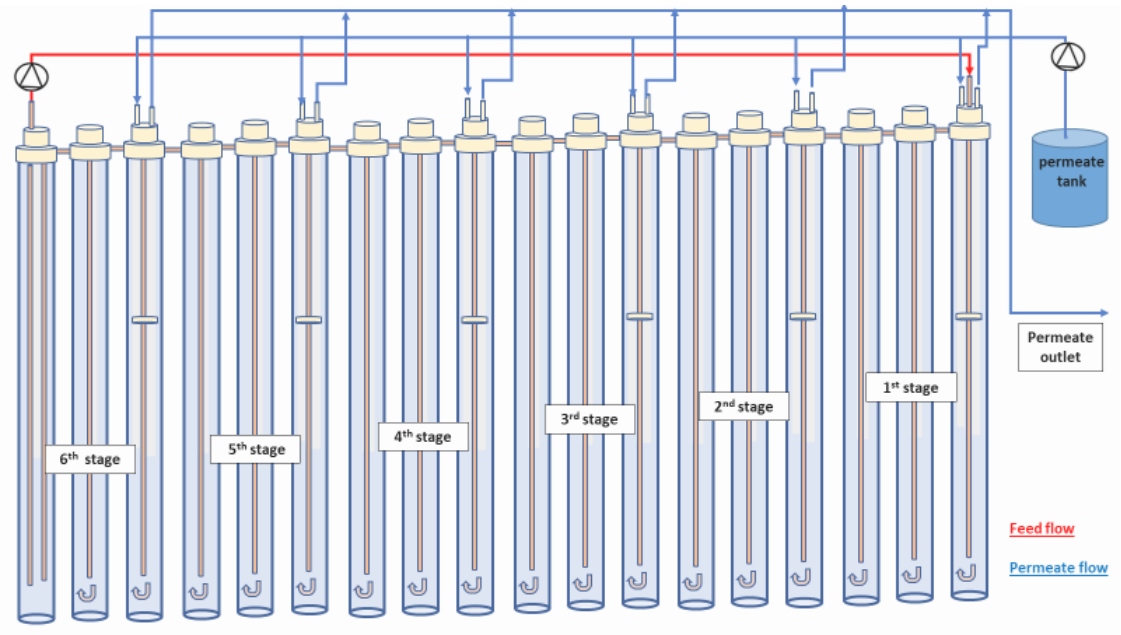

Figure 19. Conceptual Illustration of a Multi–stage Direct Heating SP–MD System

3.3 Summary

The performance of an innovative MD module that integrates hollow fiber membranes within an evacuated solar tube to desalinate aqueous NaCl solution was investigated experimentally. The small–scale, stand–alone desalination system utilizes solar energy directly and it is suitable to provide drinkable water in remote areas with limited access to fresh water and electricity.

The results from the indoor tests validated the hypothesis that applying solar radiation would improve the permeate flux and efficiency when compared to that when the radiation is absent (under the same operating conditions). The improvement in permeate flux was greater at lower feed flow rates. The flux and efficiency enhancement can be mainly attributed to the reduction in the temperature drop in feed water.

The outdoor tests of the module show that it can operate with intermittent energy supply. The hourly permeate flux per membrane effective area varied between ~1 to ~7

$kg \cdot m^{-2} \cdot h^{-1}$. The average water production per collector absorbing area was found to be 0.37 $kg \cdot m^{-2} \cdot h^{-1}$. The system was found to produce 0.7 kg of fresh water per day (4.2 L/day for a 6–stage system).

Various real–world limitations associated with direct SP–MD were identified during the experiment. First, it is still challenging to use unheated feed water in the system. The feed water must be preheated or flow in a closed loop to sustain a high feed temperature. Second, it was found that the feed flow rate must be decreased significantly for the feed to absorb solar radiation as shown in Table 3. As a result, a larger boundary layer resistance is created at the feed side and the effect of temperature polarization increases, which leads to lower flux.

4 SOLAR–HEATED SUBMERGED VACUUM MEMBRANE DISTILLATION SYSTEM[2]

Membrane distillation (MD) has received considerable attention in the last two decades as a promising desalination technology to provide high–quality water [4,49]. MD uses a microporous hydrophobic membrane to separate between two sides, a hot feed side (e.g. seawater or brackish water) and a cold permeate side. Due to the partial pressure difference across the membrane wall, vapor is created at the surface of the membrane on the hot feed side and transferred to the cold permeate side leaving behind non–volatile components in the feed water [10].

While water production in MD is relatively lower than that from reverse osmosis (RO), MD has less fouling issues and doesn't require intensive pre–treatment, and it can tolerate high concentration feed water [4,9]. Additionally, MD can use low–grade energy sources such as solar energy and geothermal energy [5]. Among the four major MD configurations—direct contact MD (DCMD), vacuum MD (VMD), sweeping gas MD (SGMD), and air gap MD (AGMD)—VMD was found to yield the highest permeate flux and lowest energy loss [19,50] and has the potential to be further improved through other novel configurations [51]. In VMD, a vacuum is created on the permeate side where vapor is collected and condenses outside the MD module.

---

[2] Published in *Separation and Purification Technology* as:
Bamasag, A., Alqahtani, T., Sinha, S., Ghaffour, N., & Phelan, P. (2020). Solar-heated submerged vacuum membrane distillation system with agitation techniques for desalination. *Separation and Purification Technology*, 117855.

Recent studies have proposed *submerged* membrane distillation (S–MD) systems as a more energy–efficient alternative to conventional cross–flow MD modules [52]. In the MD literature, a cross–flow configuration refers to those modules with a feed inlet and outlet, where the hot feed stream is pumped through the system and travels tangentially *across* the membrane's surface. In conventional S–MD systems, however, the membranes are directly placed in a tank filled with feed water which is heated by an electric heating element. This configuration eliminates the need for feed pumping and reduces heat loss due to recirculation and reheating.

Much of the work related to S–MD has mainly focused on treating high concentration feed water with a large suspended solid content, such as inland brine [53,54], seawater RO brine [55], and coal–seam–gas–produced water [56]. Some researchers suggested using S–MD with membrane bioreactor (MBR) systems [57–59], and others combined it with a crystallization process to achieve zero liquid discharge [60–62], amongst numerous other applications using hybrid systems [7].

Because the feed water is not flowing along the membrane surface in S–MD systems, the temperature and concentration polarizations are expected to be higher (i.e. the feed temperature and concentration at the membrane's surface is higher than those at the bulk phase), which has a negative impact on the permeate flux and can cause severe fouling [18,53]. Therefore, researchers have proposed several agitation techniques to mitigate this problem in S–MD systems, including transverse vibration [53,54,62], stirring [52,55,62], and aeration [53,54]. These techniques were found to be helpful in reducing fouling, improving permeate flux, and producing higher quality water for a longer period of time. For instance, Meng et al. found that, in a submerged VMD system, applying transverse

vibration can improve the permeate flux by 21% compared to the case without agitation [53]. More recently, Zou et al. suggested that stirring and aeration can significantly reduce the effect of temperature polarization, improve the permeate flux, and delay membrane fouling [62].

The idea of utilizing solar energy with S–MD was suggested by Mericq et al. [63]. The authors theoretically compared a membrane module submerged in a salinity–gradient solar pond (SGSP) with three different solar–powered VMD configurations. It was found that the S–MD suffers significantly from temperature and concentration polarizations. The system was found to be difficult to implement and produced a very low permeate flux (~95% lower) when compared to an external module fed by water from the SGSP in a cross–flow operation mode. However, the authors claimed that agitation techniques (such as circulation or bubbling) can improve the S–MD performance even though these techniques may affect the stability of the SGSP and require intensive maintenance and energy.

The aim of this chapter is to experimentally investigate the feasibility of a submerged vacuum membrane distillation (S–VMD) system that uses solar energy as the sole heating source. This study utilizes an evacuated tube solar collector (ETC) as the feed container. The hollow fiber membranes are submerged in the middle of the ETC. Two agitation techniques (aeration and internal circulation) are applied to examine their effects on the feed temperature and the permeate flux. It is expected that the turbulence effect resulting from these techniques will reduce the effect of temperature and concentration polarizations, thus achieving better permeate flux.

To the best of our knowledge, this is the first attempt to design and test a solar–powered S–MD system. Therefore, the main focus of this chapter is to demonstrate the functionality of the system by measuring its daily performance and understand the effects of different agitation strategies on the permeate flux and efficiency. The study also provides a preliminary understanding of how relatively long operation hours impact the permeate flux and its quality. In future work, long–term operation tests using a high concentration feed water (e.g. real inland brine) will be conducted to study the resulting fouling and scaling in the membrane based on different modes of feed agitation.

It is worth noting that the use of ETC has been studied with cross–flow MD process under the VMD [37] and DCMD [64] configurations. In these studies, the feed water is pumped to the bottom of the ETC by an external pump and then moves in a cross–flow parallel to the hollow fiber membranes which are placed at the top of the ETC, mimicking the design of conventional shell–and–tube MD modules. On the contrary, the proposed solar–heated S–VMD system in the present study will work as a closed MD system in which the feed water does not leave the module. This will minimize the heat loss due to recirculation, eliminate the need of circulation pumps (i.e. less electric energy), and also reduce the complexity of the system.

The proposed S–VMD system can utilize solar and electric energy in a more efficient way, which in turn can drive down the capital and operating costs. The small–scale system can provide high–quality potable water in areas with limited natural resources. This system could be a promising solution to real–world challenges such as treating produced water in the oil and gas industry.

4.1 Materials and Methodology

4.1.1 The Design of the S–MD Module

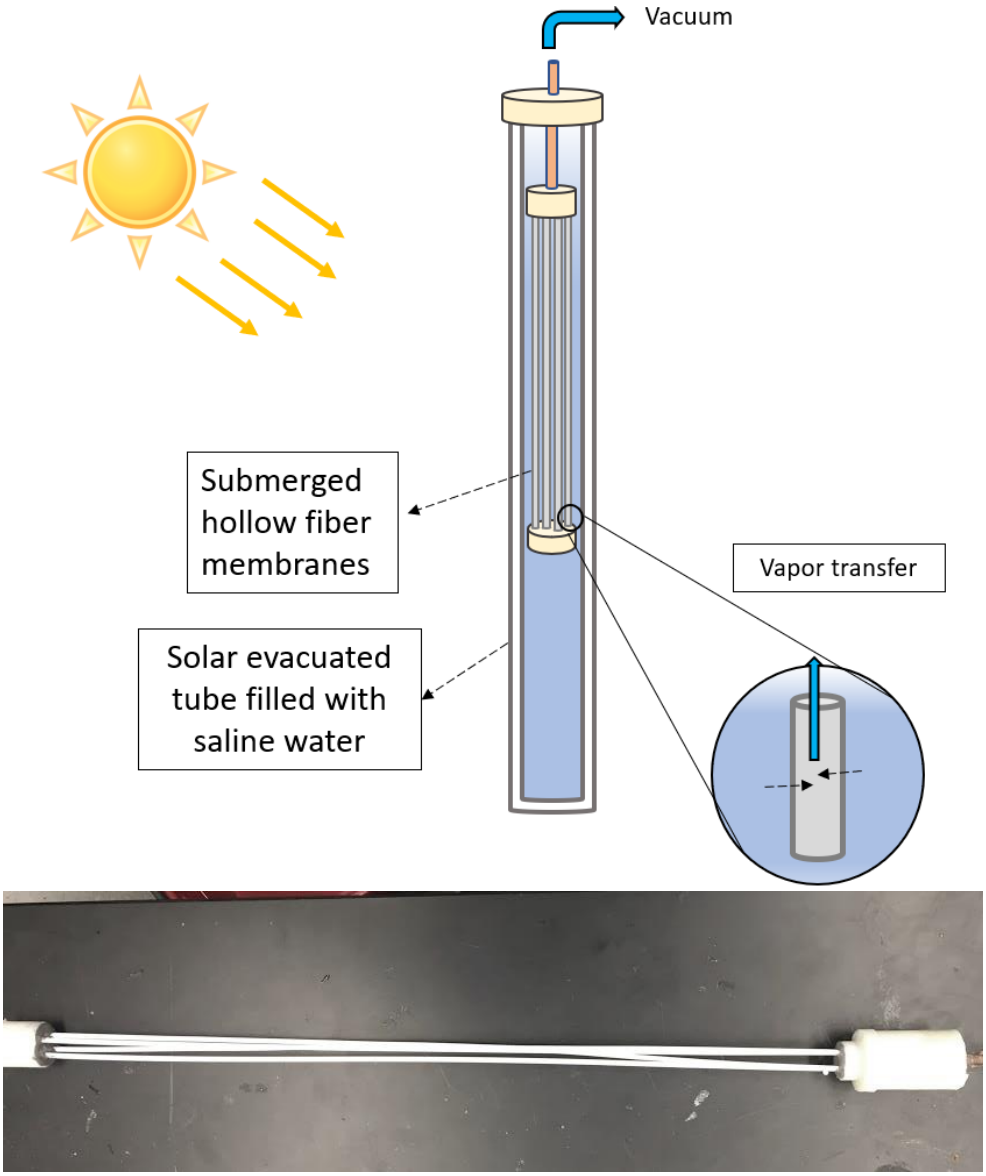

Figure 20. A Schematic Diagram (Top), and a Photograph (Bottom) of the S–VMD Module.

A schematic and a photograph of the solar–heated S–VMD module are shown in Figure 20. Four commercially available hydrophobic capillary membranes with effective length of 40.5 cm were used in the module. The membranes were potted using epoxy resin in

plastic caps. The bottom cap represents the "dead–end" side and the top cap is connected to the vacuum line. Due to the manual potting procedure, the exact surface area of the membrane can be estimated with some certainty as 0.0092 ± 0.0001 m^2. The membrane area was determined so that the heat loss $\dot{Q}_{loss}$ due to the distillation process can be compensated by the heat input $\dot{Q}_{in}$ from solar radiation to achieve a thermally stable operation. The ratio of the membrane area to solar absorbing area (A_m/A_a) was found to be 1/9 to 1/10 [37,64].

Unlike previous studies that placed the submerged membranes in an electrically heated feed tank, the proposed solar–heated S–VMD module is placed within an evacuated–tube collector (ETC). ETCs are made of double–wall low emissivity borosilicate glass, where the outer wall is highly transmissive, and the inner wall is coated with a black layer to increase absorption across the entire solar spectrum. A vacuum between the two walls minimizes the heat loss to the surroundings. Table 4 summarizes the physical characteristics of the S–VMD system.

Table 4 Characteristics of the Solar–Heated S–VMD Module

Membrane manufacturer	Microdyn–Nadir
Membrane material	Polypropylene
Pore size (μm)	0.2
Porosity	0.7
Tortuosity	1.4
Fiber inner diameter (mm)	1.8
Fiber outer diameter (mm)	2.7
Fiber thickness (μm)	450
Number of fibers	4
Length of fibers (cm)	40.5
Membrane surface area A_m (m^2)	0.0092
Solar tube inner diameter (mm)	44
Solar tube outer diameter (mm)	58
Solar tube length (m)	1.8
Solar absorbing area A_a (m^2)	0.1

4.1.2 Experimental Setup and Procedure

4.1.2.1 Outdoor Testing for Daily Operation

A schematic and a photograph of the outdoor experimental setup are shown in Figure 21. The experiments were conducted during the second half of February 2020 in Tempe, Arizona, USA (latitude: 33.43°; longitude: –111.96° and altitude of 1132 ft above sea level). Overnight, the ETC is filled with NaCl saline water at concentrations of 30–35 g/L (TDS of standard seawater). After sunrise, by the time the feed water temperature reaches about 70 ^{o}C a vacuum pressure (–94.5 ± 1.0 kPa) is applied on the permeate side of the membranes using a vacuum pump. The vapor generated by the distillation process transfers outside the module and condenses in an external cold trap placed in an ice bath. The amount of distillate water is measured every hour. A portable electrical conductivity meter (HM EC–3) is used to measure the permeate water quality. The permeate flux J (in $kg \cdot m^{-2} \cdot h^{-1}$) is calculated as:

$$J_{measured} = \frac{m_d}{A_m \Delta t} \tag{4.1}$$

where m_d is the amount of distillate water (kg), A_m the membrane area (m^2), and t the sampling period (h).

A thermocouple is placed in the middle of the ETC (just below the membranes) to measure the temperature of the feed water. A data acquisition system (National Instruments, cDAQ–9171) records the real–time temperatures using the LabView platform. The vacuum pressure was monitored using a pressure gauge in the permeate side. A pyranometer sensor at the same tilt angle of the ETC (~36^{o}) records the real–time solar intensity.

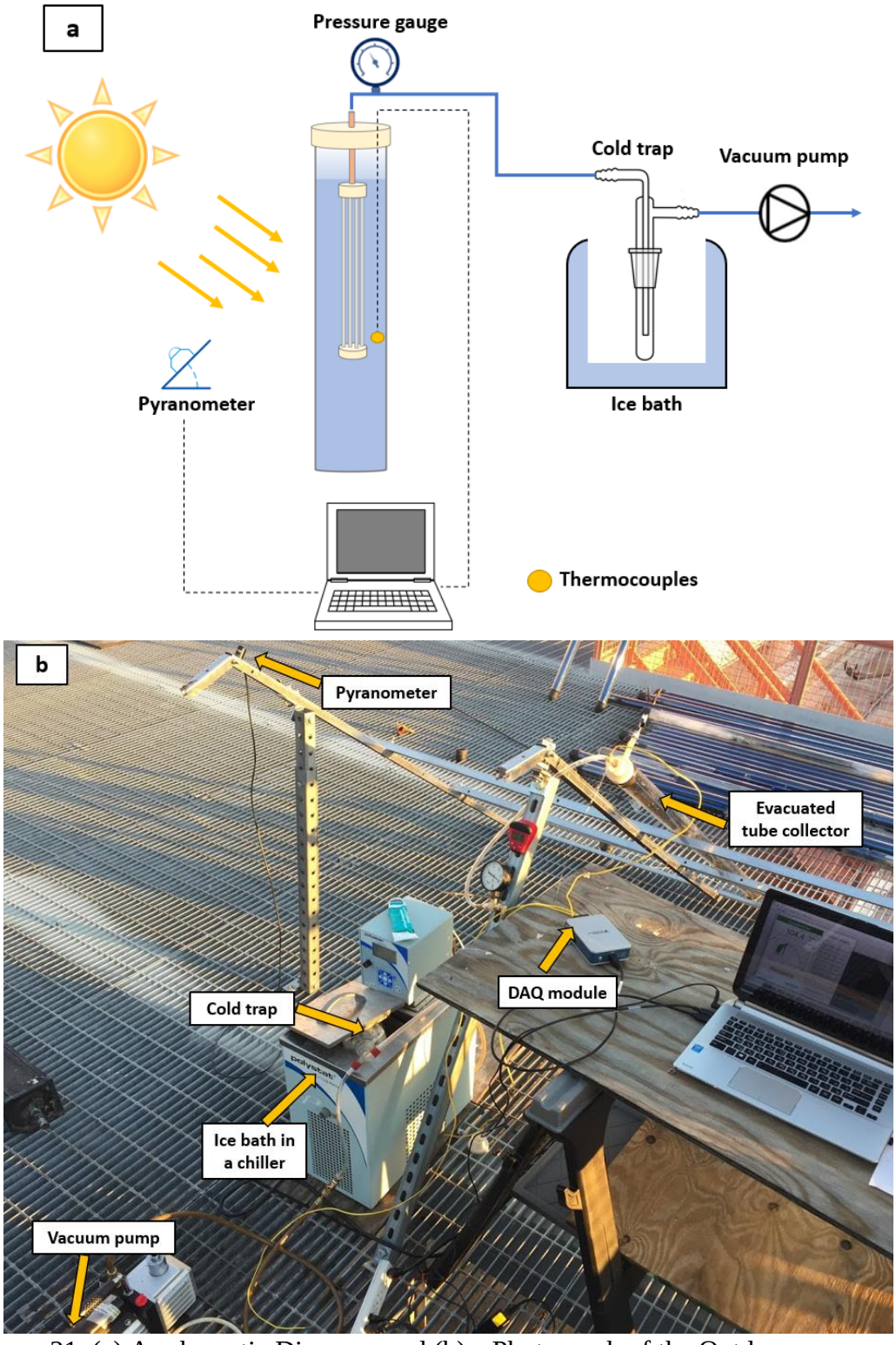

Figure 21. (a) A schematic Diagram, and (b) a Photograph of the Outdoor Experimental Setup.

Four different scenarios were studied: (i) no agitation on a sunny day, (ii) no agitation on a cloudy day, (iii) application of aeration, and (iv) application of internal circulation. During aeration, a 3 W air pump supplies air at a rate of 2.5 L/min (using an adjustable flow knob) to an air stone that is placed at the bottom of the tube to generate macro–size bubbles as shown in Figure 22(a). This induces a turbulence effect within the feed and generates shear at the membrane surface. For the case of internal circulation, a 15 W submersible pump is placed at the bottom of the feed water as shown in Figure 22(b). The pump circulates feed water from the bottom to the upper part of the ETC at a rate of 3.5 L/min, to ensure a good distribution of heat along the module. The flow rate is controlled by a power supply unit. Due to power restrictions, the pump works in a cycle (20 minutes ON – 10 minutes OFF).

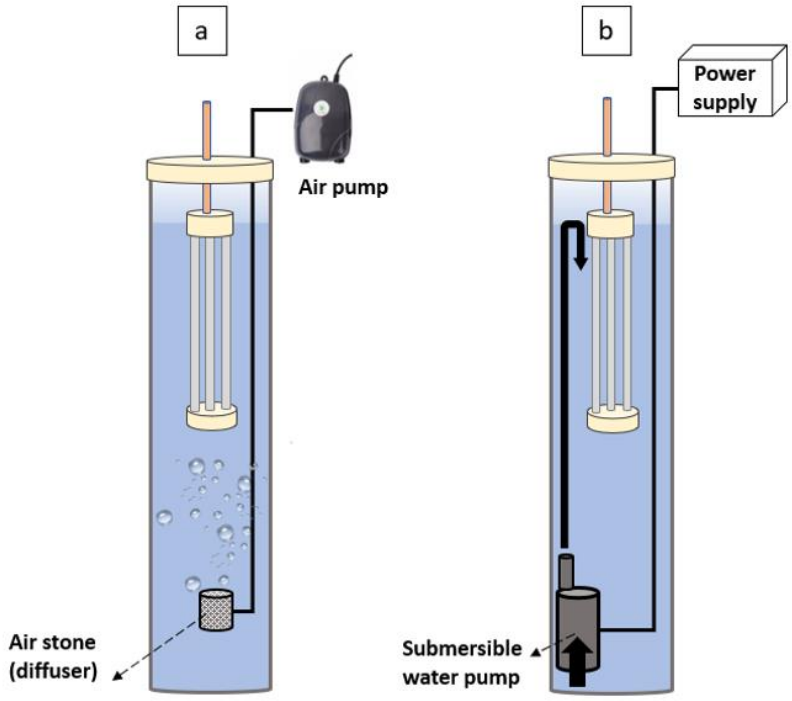

Figure 22. Different Modes of Feed Agitation: (a) Aeration, (b) Internal Circulation.

At the completion of each daily experiment, the membrane was taken outside the solar tube to be rinsed and cleaned in order to be reused the following day. This process was found to be sufficient to restore the membrane's integrity particularly after a short–term operation that used synthetic NaCl solution as the feed water [60,62].

4.1.2.2 Indoor Testing Under Steady–State Operating Condition

A similar experimental procedure was conducted in an indoor controlled environment to measure the performance of the S–VMD with agitation and without agitation under steady–state operating conditions (i.e. at a constant feed temperature $T_{f,b}$). The energy source in the indoor tests is an electric immersion heating element. A transparent tube with similar dimensions as the ETCs was used as the feed water container in order to have a practical comparison with the outdoor results.

4.1.3 Uncertainty Analysis

Measurement uncertainties were calculated to be ± 0.58 g, ± 0.6 °C, and ± 2 cm^2 for water yield, temperature, and membrane effective surface area, respectively. The pyranometer sensor and the conductivity meter have a calibration accuracy of 5%. The vacuum pressure was controlled within ± 1.0 kPa, and the feed temperature in the indoor experiment was controlled within 2.0 °C. Repeated readings were obtained during the indoor experiments and showed a good reproducibility with a maximum uncertainty of 8.7%. Expanded uncertainty method with high level of confidence (~95%) was used [44]. These values are shown as error bars in the figures below.

4.2 Results and Discussion

4.2.1 Indoor Experiments Under Steady–State Conditions

In the indoor tests, the permeate flux was measured under steady–state operating conditions. The bulk feed temperature $T_{f,b}$ inside the tube (container) was kept at 45, 55, and 65 ^{o}C. The tests were conducted without agitation, with aeration (at an air flow rate of 1 and 2.5 L/min), and with circulation (at a flow rate of 2.0 and 3.5 L/min). Since the bubble motion inside the tube can be affected by the module orientation, the indoor aeration test was also studied with an inclined tube. In order to measure the effect of different agitation techniques on the module's performance, the permeate flux enhancement ratio Φ can be defined as:

$$\Phi = \frac{J_{with\ agitation}}{J_{no\ agitation}} \tag{4.2}$$

where $J_{with\ agitation}$ and $J_{no\ agitation}$ are the measured permeate fluxes of the S–VMD with agitation and without agitation, respectively.

Figure 23(a) shows the permeate flux as a function of the feed temperature (± 2 ^{o}C) under different agitation techniques. As expected, the permeate flux in all cases increases as the feed temperature increases. This is due to the fact that the permeate flux J is linearly dependent on the vapor partial pressure difference across the membrane [9,17]:

$$J = K\left(P_{f,m} - P_v\right) \tag{4.3}$$

where K is the mass transfer coefficient (kg·Pa^{-1}·m^{-2}·h^{-1}), $P_{f,m}$ the feed vapor pressure at the membrane surface (which increases exponentially with water temperature at the membrane surface $T_{f,m}$ according to Antoine's equation), and P_v the vacuum pressure in the permeate side.

Apparently, Figure 23(a) indicates that a greater permeate flux was achieved with agitation techniques, which is in agreement with results reported in the literature [53,62]. This can be mostly attributed to the reduction in temperature polarization effect due to turbulence from agitation which reduces the boundary layer resistance (i.e. higher heat transfer coefficient) [65]. This indicates that, under agitation, the difference between the feed temperature at the membrane's surface and that at the bulk phase ($T_{f,b}$–$T_{f,m}$) is less when compared to the case without agitation, resulting in a greater partial pressure difference and therefore a higher permeate flux as illustrated in Eq. (4.3).

The permeate flux enhancement ratio Φ for different agitation experiments under different $T_{f,b}$ is shown in Figure 23(b). Aeration was found to be more effective than circulation, particularly when the feed container/tube was placed vertically. The values of Φ varied between 1.16 and 1.35 at an aeration rate of 1 L/min, and between 1.34 and 1.47 at an aeration rate of 2.5 L/min, as illustrated in Figure 23(b). The long tube shape of the feed container played a role in magnifying the agitation effect under the aeration technique (See video 1 in the Supplementary Material). The bubble motion relative to the surrounding feed within a narrow cross–sectional area induced a relatively high degree of turbulence, diminishing the boundary layer resistance at the membrane surface. This finding agrees with Chen et al. who investigated the effect of feed aeration in a crossflow shell–and–tube DCMD system [66]. The authors found that permeate flux can be enhanced by 72% under very low feed flow rates. The enhancement ratio diminishes with increasing feed flow rate, as the boundary layers have already been reduced at higher flow rates. This implies that aeration is an excellent agitation strategy with submerged MD systems, in which the feed water flow is dominated by natural convection.

In order to mimic the operating condition of the outdoor test, an indoor aeration test with an inclined tube was conducted. It can be seen that the values of Φ are lower (between 1.11 to 1.15) in the aeration test with an inclined tube relative to those with a vertical tube (Figure 23(b)). One reason that can explain these results is that, when the tube is placed vertically, the air bubbles are distributed evenly, generating a large degree of turbulence. However, when the tube is inclined, the bubble motion is concentrated in the upper part of the tube's inner wall due to gravity, by–passing the hollow fiber membranes (See video 2 in the Supplementary Material). This caused relatively less feed turbulence along the membranes, which may explain the lower values of Φ in the inclined tube.

This observation seems to contradict the results presented in Chen et al. [66], who found that air bubbling in a DCMD shell–and–tube module inclined at a 45^{o} angle can enhance the flux by 34% compared to 28% in a vertically oriented module and 12% in a horizontal module. This contradictory result may be explained by the fact that the module they used is 0.34 m long, much shorter than the solar tube used in this study. Therefore, the bubble behavior in the long tube in the present study may tend to be similar to that in the horizontally oriented module, which "may experience by–passing because of gas buoyancy" as Chen et al. have noted, a similar observation for the inclined tube in this study.

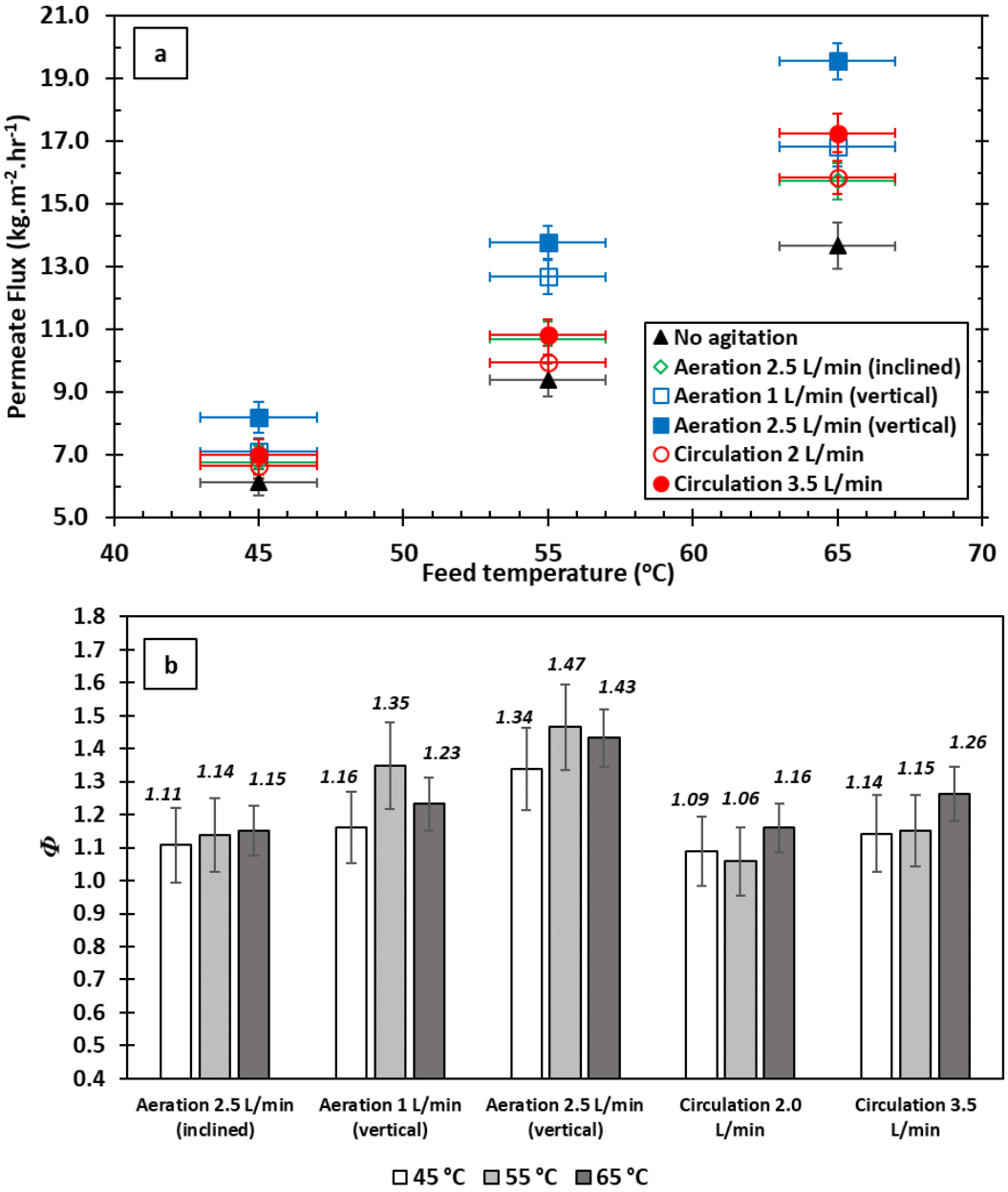

Figure 23. (a) Permeate Flux J and (b) the Flux Enhancement Ratio Φ as a Function of the Feed Temperature with and without Feed Agitation, from the Indoor Experiments. (P_v = –94.5 ± 1.0 kPa).

Although feed circulation improved the permeate flux compared to the case without agitation, the enhancement ratio Φ was relatively lower when compared to aeration in a vertically oriented tube. The values of Φ were 1.09, 1.06, and 1.16 at a circulation rate of

2 L/min, and was 1.14, 1.15, and 1.26 at a circulation rate of 3.5 L/min, at $T_{f,b}$ = 45, 55, and 65 °C, respectively. The relatively low values of Φ can be explained in part by the fact that internal circulation in submerged MD systems does not form a uniform hydrodynamic flow across the membrane as in the cross–flow MD configuration. In fact, the water movement can be quite random and may be affected by the density variation of feed water due to non–uniform temperature distribution (because of non–uniform heat flux) in the feed container. The turbulence effect was observed to be more effective in the part close to the pump outlet (just above the S–MD module), while the feed movement along the membranes was found to be much less turbulent (See video 3 in the Supplementary Material).

4.2.2 Outdoor Experiments Under Ambient Weather Conditions

4.2.2.1 Daily Performance on Sunny Days

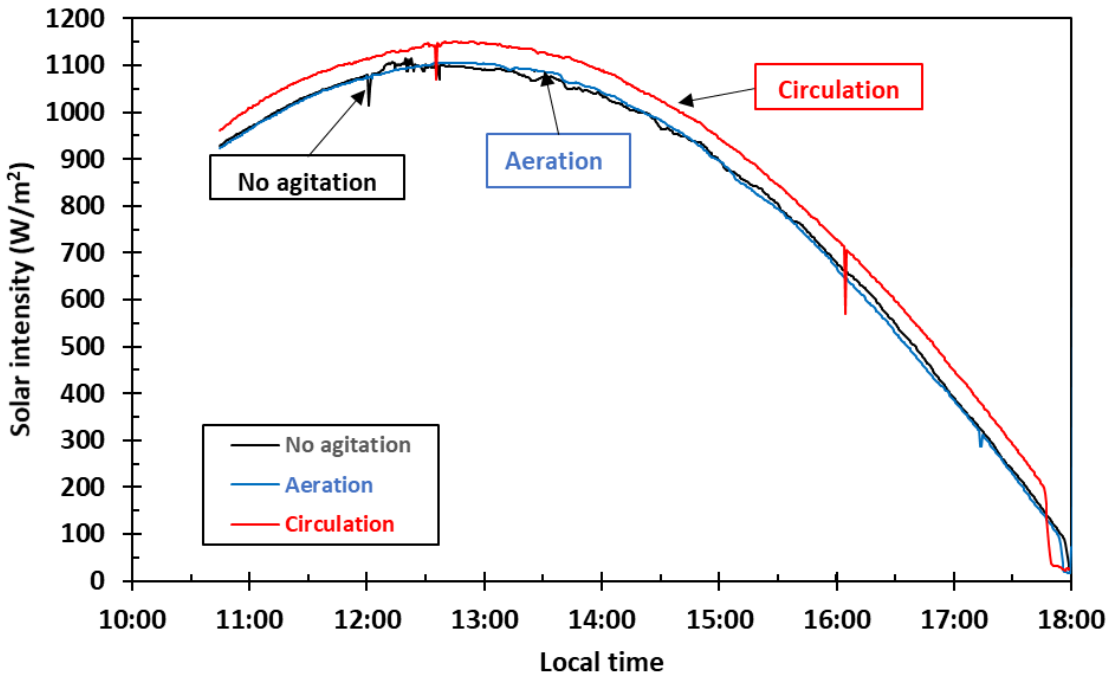

Figure 24. Solar Intensity for Different Sunny Outdoor Experimental Runs (Different Days).

The daily performance of the S–VMD system without agitation and with agitation (aeration and internal circulation) was measured. Three experiments were conducted under sunny days with a clear sky within a one–week period, in order to ensure similar operating conditions. Figure 24 shows the solar intensity profiles on these days.

It was found that the feed water temperature inside the ETC reaches 70 ± 2 ^{o}C at around 11:00 AM (local time). At this time, a vacuum pressure of –94.5 ± 1.0 kPa (equivalent to the partial vapor pressure at 37 ^{o}C) is applied to the permeate side of the membranes.

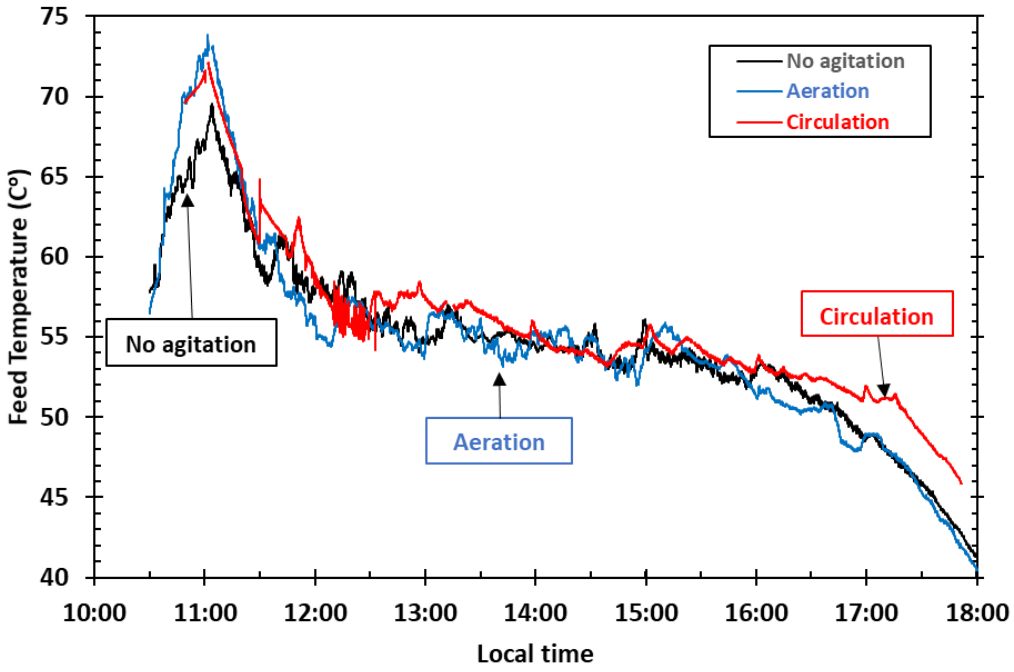

Figure 25. Variation of Feed Temperature for Different Sunny Outdoor Experimental Runs (Different Days).

Figure 25 shows the feed temperature profile as a function of time. The temperature fluctuation can be attributed to the continuous movement of water due to natural convection, bubble induction, and/or circulation. It can be seen that the feed temperature spikes 2–3 ^{o}C each hour as the process is stopped for three minutes to measure the amount

and quality of the distillate water. While this spike could affect the permeate flux, its influence is diminished on the comparison as it is observed in all cases.

The hourly permeate flux in each case is shown in Figure 26. It is evident that, in general, the permeate fluxes match approximately the temperature profiles in Figure 25. The maximum hourly permeate flux occurred in the first hour (from 11:00 to 12:00) in all cases. The first hour also experienced the highest temperature drop (>11 ^{o}C), indicating that the heat input from solar radiation $\dot{Q}_{in}$ in the first hour was not sufficient to compensate for the heat loss due to distillation $\dot{Q}_{loss}$. The permeate flux in the next five hours decreased gradually and the operation was more thermally stable as the feed dropped 5–6 ^{o}C from 12:00 to 17:00. In the last hour, the feed temperature decreased rapidly due to the weaker solar intensity which resulted in a lower permeate flux.

During the no–agitation operation, the permeate flux varied between 5.9 to 11.1 $kg \cdot m^{-2} \cdot h^{-1}$ (with an average hourly permeate flux of 8.6 $kg \cdot m^{-2} \cdot h^{-1}$). This proves that the concept of a stand–alone submerged membrane within a feed container can achieve a high production of water without the need of feed pumping or even agitation.

As expected, feed agitation was found to be effective in increasing the water production during the day. Interestingly, the results revealed that the circulation technique slightly outperformed aeration in the sunny outdoor test. The average hourly permeate flux was 9.4 $kg \cdot m^{-2} \cdot h^{-1}$ under aeration (10% increase relative to the no–agitation test) and was 10.5 $kg \cdot m^{-2} \cdot h^{-1}$ under circulation (22% increase). While the solar intensity was slightly higher during the circulation experiment (Figure 24), the temperature profile was similar for the three sunny outdoor experimental runs (Figure 25). This suggests that the amount of solar radiation is not the primary reason that explains why the circulation technique was more

effective during the outdoor experiment. In fact, the enhancement ratios are relatively consistent with those obtained in the indoor steady–state tests, which varied between 14% to 26% under circulation and between 11% to 15% under aeration with an inclined tube, as shown in Figure 23(b).

As discussed earlier, aeration is an effective strategy to reduce the temperature polarization effect and enhance the permeate flux. However, the aeration effect in an inclined tube is lower as the bubble motion tends to concentrate in the upper part of the inner wall causing less turbulence near the membranes compared to that in a vertically oriented tube. Moreover, because the bubbles are concentrated in a small area and due to the high length–to–diameter ratio of the tube, the bubbles may tend to merge as they move from the bottom to the upper part of the tube. Consequently, larger bubbles are formed, and the total number of bubbles are reduced, resulting in less turbulence effect in the feed [66].

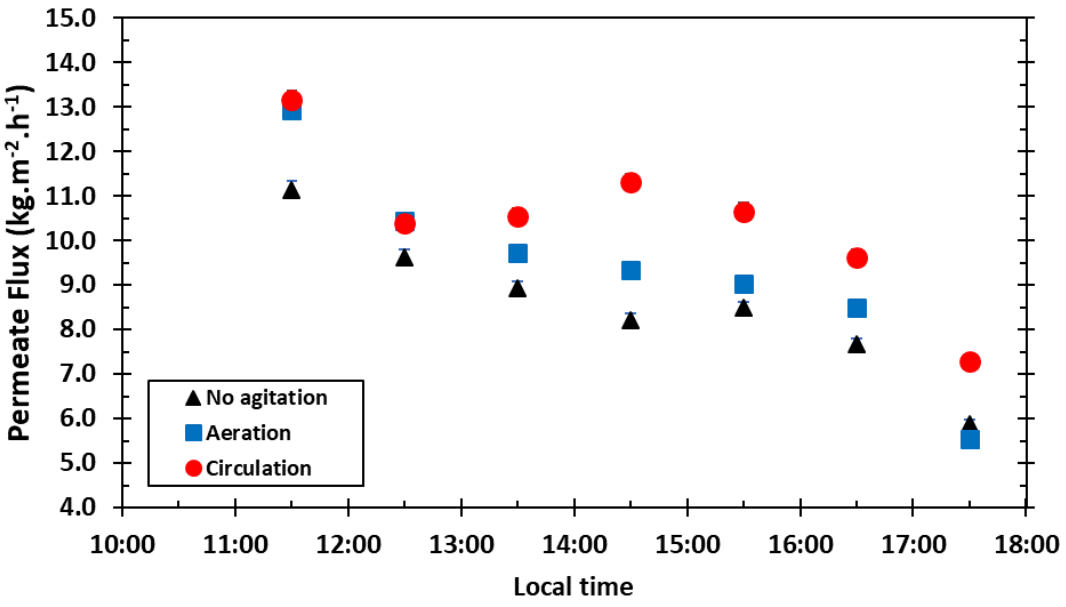

Figure 26. Variation of Permeate Flux of the S–VMD System with and without Agitation, from the Outdoor Experiments on Sunny Days. (P_v = –94.5 ± 1.0 kPa).

Furthermore, internal circulation was found to achieve higher permeate flux throughout the day as shown in Figure 26. This can be explained in part by the reduction of the temperature polarization effect as discussed earlier. Another possible explanation for this result is that, during the no–agitation test, the area near the membranes becomes relatively cooler due to the evaporation effect. Since the solar tube is heated uniformly, the feed water circulates slowly inside the tube by natural convection. Introducing forced circulation allows the feed water to move from the hotter parts inside the tube to the less hot areas near the membranes, exposing the membranes to hotter feed water continuously, resulting in a higher permeate flux. This was clearly demonstrated in the temperature profile during the weaker solar intensity (from 16:30 to 18:00), where the feed temperature under the circulation mode is 3–4 ^{o}C higher than that under no–agitation and aeration, as shown in Figure 25.

4.2.2.2 The Daily Performance on A Cloudy Day

In order to investigate the functionality of the system under different weather conditions, a cloudy day test without agitation was conducted. Figure 27 illustrates the feed temperature, hourly permeate flux, and the solar intensity during this test. It is clear that the feed water on a cloudy day wasn't heated as much as during sunny days due to the weaker solar intensity. In fact, the feed temperature reached 55 ^{o}C at 11:00 (local time), which is ~15 ^{o}C lower when compared with sunny days at the same time. Accordingly, the permeate flux was found to be lower throughout the day. The flux varied between 7.2 to 8.6 $kg \cdot m^{-2} \cdot h^{-1}$ during the first half of the experiment when the feed temperature was above 55 ^{o}C. The flux gradually decreased until it reached 3.6 $kg \cdot m^{-2} \cdot h^{-1}$ when the feed

temperature was below 40 °C. Although the permeate flux is reduced relative to sunny days, the results indicate that the system is still able to maintain a stable water production under weak and highly intermittent solar energy.

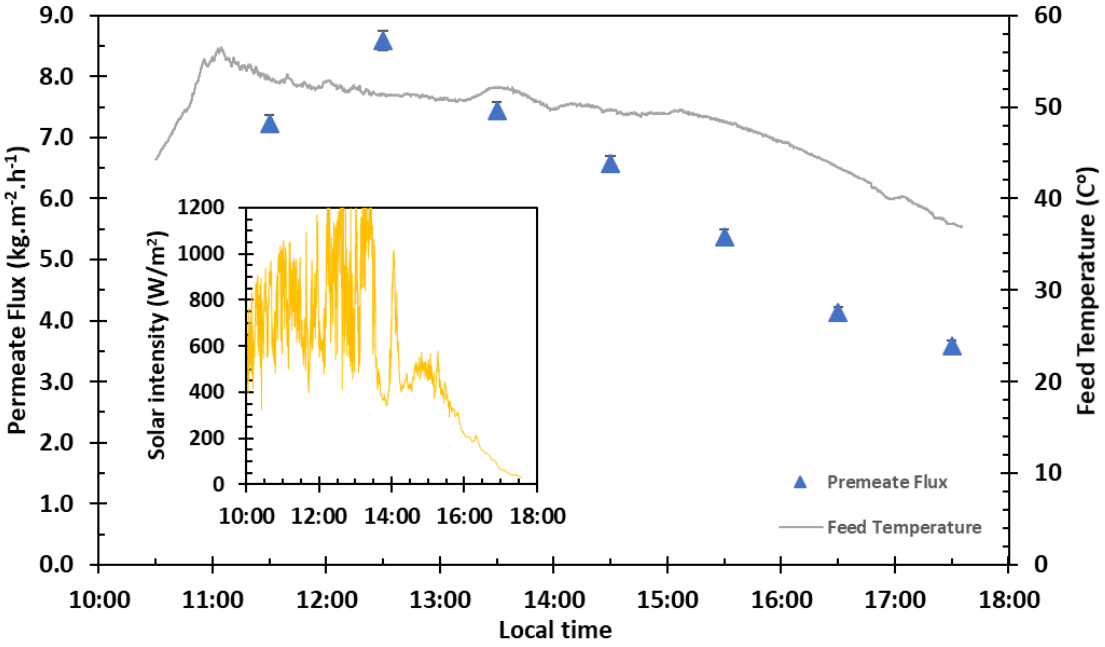

Figure 27. The Changes in Solar Intensity, Feed Temperature, and Permeate Flux of the S–VMD without Agitation on a Cloudy Day (P_v = –94.5 ± 1.0 kPa).

4.2.3 Technical Assessment of The Outdoor Tests

Table 5 summarizes the daily performance parameters of the different experiments conducted in this study. The amount of distillate water under no–agitation conditions was 0.55 kg on a sunny day and 0.40 kg on a cloudy day. Feed aeration and circulation produced 0.60 kg and 0.67 of fresh water, respectively. This indicates that the system can produce 5.5 to 6.7 kg of fresh water per day if 10 ETCs (with a total absorbing area of 1 m^2) equipped with a total membrane area of 0.1 m^2 are used. This is enough to provide the minimum drinking water needs for two to three persons [67]. It is worth mentioning that

these results were achieved during the winter season under only 7 hours of operation. It is expected that the amount of produced water would be more during other seasons due to greater radiation, warmer ambient weather (i.e. less heat loss to surroundings), and longer daytime hours.

Table 5 Comparison of Performance Parameters for Different Experimental Runs

Experiment	Ambient T (°C)	Daily solar exposure (kWh/m^2)	Total distillate water (g)	Average J (kg·m^{-2}·h^{-1})	Daily water production per A_a (kg/m^2/day)	Average distillate water quality (μS/cm)
No Agitation	13-25	7.92	548	8.6	5.5	38
Aeration	11-23	7.88	602.5	9.4	6.0	33
Circulation	9-20	8.30	671	10.4	6.7	28
Cloudy day	17-24	5.09	395	6.1	4.0	47

Table 5 also shows the average water quality for each experimental run. The conductivity of the distillate water varied between 28 to 47 μS/cm, well below the acceptable conductivity of drinkable water and in–line with high water quality standards produced by thermally–driven processes [68]. The water quality may be reduced under longer operation hours or if high concentrated feed is used, considering the fact that membrane wetting is a critical challenge in the VMD configuration. In this context, agitation techniques can play an important role not only to enhance the permeate flux, but also to mitigate membrane scaling, delay flux decline, and produce better quality water as researchers have observed [54,62]. These parameters will be deeply investigated and reported in future work.

4.2.3.1 Thermal Performance Parameter (*GOR*)

To measure how well the input solar energy is utilized to produce water, the gain output ratio *GOR* is used. *GOR* is defined as the ratio of the heat required to evaporate the distillate water to the total input solar radiation [20,43]:

$$GOR = \frac{m_d h_{fg}}{I A_a} \quad (4) \qquad (4.4)$$

where m_d is the daily water production (kg), h_{fg} the latent heat of water (J/kg), I the daily solar intensity (kWh/m^2), and A_a the absorbing area of the solar collector (m^2). The values of *GOR* were found to be between 0.43 (in no-agitation tests) to 0.51 (in circulation tests) as Figure 28 shows. This indicates that more distillate water can be produced per unit of input energy via solar radiation, if an agitation technique is used in the process.

It is important to note that in cross-flow VMD systems, where the feed water is pumped into the MD module, higher *GOR* values can be achieved if a heat recovery mechanism is applied (i.e. utilizing the vapor condensation process to preheat the inlet feed, or the use of multi-stage system with internal heat recovery [69]). This mechanism is unattainable in submerged VMD systems, which represents a limitation of the submerged MD configuration. Nevertheless, heat can be recovered for other heating applications, such as residential water heating. The amount of recoverable heat of the current design can be estimated to be between 3.5 to 4.2 kWh per 1 m^2 of A_a.

Moreover, considering the fact that a large amount of solar radiation goes to heating up the feed water from ~15 ^{o}C at 8:00 (local time) to ~70 ^{o}C at 11:00 (local time), better performance of the current S-VMD design can be achieved if the feed water is pre-heated

as suggested by other authors [37]. As a result, the system can operate for longer hours, produce more water per day, and achieve a better thermal efficiency.

4.2.3.2 Specific Electric Energy Consumption (*SEEC*)

Specific electrical energy consumption (*SEEC*) is a commonly used parameter to measure the electrical performance of MD systems. *SEEC* (in kWh/kg) can be defined as the amount of electric energy ($\dot{W}$) required to produce a unit mass of distillate water [70]:

$$SEEC = \frac{\dot{W}}{m_d} \tag{4.5}$$

The SEEC estimation in this study considers the electric energy required to operate the vacuum pump, the air pump (in the aeration experiment), and/or the submersible water pump (in the circulation experiment). This can determine whether the added energy required by the agitation techniques resulted in a better energy consumption per unit mass of produced water.

Figure 28 shows the values of *SEEC* for each experimental run. For no–agitation tests, where the vacuum pump consumes all the input energy (~2.8 kWh/day), *SEEC* was found to be 0.51 kWh/kg. Under aeration, *SEEC* was reduced to 0.48 kWh/kg. This suggests that the added energy required to operate the air pump was negligible (~0.11 kWh/day), yet it was efficient enough to produce more distillate water. On the other hand, *SEEC* was slightly higher (0.54 kWh/kg) for the circulation technique. This indicates that, even though the total amount of distillate water is higher under circulation, it is important to take into account the amount of added energy required to operate the submersible pumps (~0.85 kWh/day) in the S–VMD system. In the cloudy day test, *SEEC* was much higher (0.71 kWh/kg) as less amount of water was produced due to weaker solar radiation.

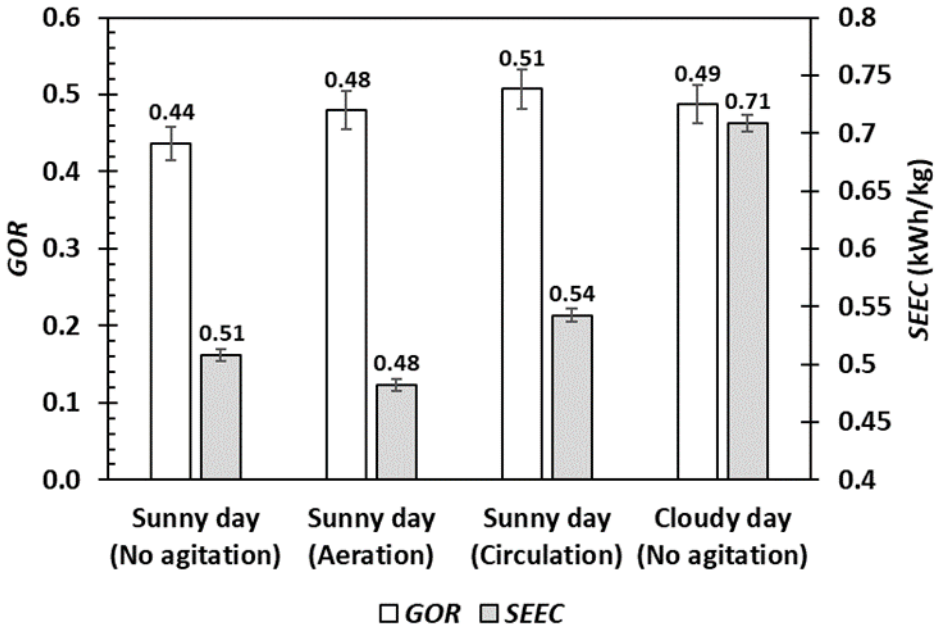

Figure 28. Comparison of *GOR* and *SEEC* of the S–VMD System from Different Outdoor Experimental Runs (P_v = –94.5 ± 1.0 kPa), where the *SEEC* Values Are Estimated for A_a = 1 m^2 (10 ETCs) Based on Our Experimental Results with 1 ETC.

It is critical to point out that the values of *SEEC* were estimated for a small–scale S–VMD system with 1 m^2 of A_a (i.e. using 10 ETCs). If more ETCs are utilized, it is expected to achieve better values of *SEEC* because the energy required for the vacuum pump per unit of ETC may be reduced.

4.2.4 Comparison of Some Direct Heating SP–MD Desalination Systems

Table 6 compares some directly heated SP–MD desalination systems including the two systems we proposed in Chapter 3 and Chapter 4. In fact, it is challenging to provide one metric that can determine which system is superior as these studies are based on different MD configurations, different membranes and operating conditions, and different methodologies. Nevertheless, it is still useful to compare these systems in terms of flux,

operating conditions and efficiency in order to identify the opportunities and challenges in this process.

As shown in Table 6, the average permeate flux in stand–alone SP–MD systems varied between 0.14 to 10.4 $kg \cdot m^{-2} \cdot h^{-1}$. It is evident that systems that work using the VMD configuration achieved higher flux, which is in agreement with what is reported in the MD literature. Other MD configurations such as DCMD and AGMD suffer from high conduction heat loss and high mass transfer resistance.

It is also noted that the submerged VMD system proposed in Chapter 4 outperformed the VMD system that works in a cross-flow configuration [37]. This may be because of the lower vacuum used in the submerged VMD system as well as the higher radiation exposure. This can be also because, in a cross-flow configuration, the system experiences higher heat loss due to recirculation.

The GOR values of the different direct SP–MD systems varies between 0.12 to 0.71 as shown in Table 6. In addition, the submerged S-VMD system we proposed in Chapter 4 achieved higher values of GOR when compared to previous cross-flow MD systems 330 that integrated the membranes within ETCs, which can be attributed in part to the lower heat losses in the submerged MD configuration. For indirect SP–MD systems, Gopi et al. found that the GOR varies between 0.1 to 6.6 depending on the system size and configuration [20]. A GOR of 13.5 was recently reported in an indirect SP–MD system working under vacuum–enhanced AGMD configuration [71].

Another parameter that is usually used in solar–based desalination systems in general (including RO, conventional thermal MED/MSF, and indirect SP–MD systems) is the rate of water produced per unit area of solar collectors. As shown in Table 6, this value varied

between 0.14 to 0. 6 $kg \cdot m^{-2} \cdot h^{-1}$ for two directly heated SP–MD systems that integrate a flat-sheet membrane in a flat–plate collector. In the DCMD study presented in Chapter 3, the average production per collector area is almost the same (~0.37 $kg \cdot m^{-2} \cdot h^{-1}$) when two or three ETCs were used, which is also close to the lower value obtained in the cross-flow VMD configuration [37]. Table 2 also presents results of The submerged VMD configuration presented in Chapter 4 achieved the highest production per collector area (0.79 to 0.96 $kg \cdot m^{-2} \cdot h^{-1}$ on sunny days), when compared to the two studies that integrated MD membranes within ETCs in a cross-flow operation mode, as shown in Table 6.

For indirect SP–MD, the water produced per collector area varies greatly from one study to another. For instance, Lee et al. found that, for a large–scale, continuous 24 h/day, indirect SP–MD system with a 550 m^2 collector area, the monthly average daily production was in the range of 400 L to 1200 L [31]. This implies that the average water production per collector area was 0.03 to 0.09 $kg \cdot m^{-2} \cdot h^{-1}$. In Duong et al. [72], the distillate water per collector area was calculated to be 0.52 $kg \cdot m^{-2} \cdot h^{-1}$ assuming 12 hours of operation. One of the first studies in indirect SP–MD, however, found that a 3 m^2 collector can be used with a DCMD system to produce 50 kg of water per day [73]. Based on 8 hours of operation, the average water production per area of collector was 2.1 $kg \cdot m^{-2} \cdot h^{-1}$, which is close to that of solar–powered MSF and MED desalination systems [16].

Table 6 Comparison of Some Direct Heating SP–MD Desalination Systems

Study	Study type	MD Configuration	Solar collector		A_m (m^2)	Operating conditions				Average hourly permeate flux [7] [kg/(m^2·h)]	Average hourly water production per A_a [7] [kg/(m^2·h)]	*GOR* [7]
			Type	A_a (m^2)		T_f	Feed flow	Time	Daily I (kWh/m^2)			
Chen et al. (2010) [1]	Experiment/ modelling	DCMD	Flat-plate	0.061		35-55	0.0086 m/s	Steady-State		6.4-19.7		-
Summers et al. (2013) [2]	Experiment	AGMD	Flat-plate	0.044		26-30	0.4–2.4 g/s	Steady-State		0.14-0.35		0.12-0.29
Ma et al. (2018) [3]	Modelling	VMD	Flat-plate	0.350		~35	Re=600	8:00- 20:00		0.60		0.71
Li et al. (2019) [4]	Experiment	VMD	ETC	0.1	0.007	~50-65	2 g/s	12:00-17:30	6	7.8	0.54	0.31
									4.2 (cloudy)	5.2	0.36	0.30
Chapter 3 (*present study*) [5]	Experiment	DCMD	ETC	0.2	0.035	~45-85	4 g/s	12:30–17:15	6.1	2.1	0.37	0.18
				0.3				11:00-17:30	6.1	3.1	0.36	0.24
Chapter 4 (*present study*) [6]	Experiment	*Submerged* VMD	ETC	0.1	0.0092	~40-70	No agitation	11:00-18:00	7.92	8.6	0.79	0.44
							Aeration		7.88	9.4	0.86	0.48
							Circulation		8.3	10.4	0.96	0.51
						~38-55	No agitation		5.1 (cloudy)	6.1	0.57	0.49

[1] A heater was assisted with solar energy (at 1100 W/m^2). [33]
[2] Under 750W/m^2 provided by a solar simulator. [34]
[3] At vacuum pressure 5kPa, continuous operation, feed water circulates in a closed loop. [35]
[4] At vacuum pressure 10kPa, feed water circulates in a closed loop that includes a water bath for the feed container. [37]
[5] At permeate inlet temperature of 22-25°C, a solar tube was used as a feed container.
[6] At vacuum pressure of -94.5 kPa.
[7] Values calculated from reported experimental data.

4.2.5 Long-Term Operation

Membrane scaling and pore wetting are particularly problematic for submerged–MD configurations. In order to demonstrate long-term operation and to investigate any changes in the permeate flux and its quality, the proposed S-VMD system was tested indoors using a new membrane for 13 consecutive days (with a total operation time of 91 hours). Two types of feeds were used during the experiments. In the first six days, a synthetic NaCl solution at 30,000 ppm was used as the feed water. In the following seven days, a real RO retentate from the Scottsdale Water Campus (Scottsdale, AZ) was used. The RO retentate had a TDS of 9,600 ppm, a conductivity of 11.6 mS/cm, and dissolved organic carbon (DOC) of 40 mg/L. A new feed water was used in each daily test to mimic the system operation in a real-life scenario.

Because the main goal of this section is to investigate any changes in the permeate flux and its quality after extended operation hours, it is essential to maintain similar operating conditions throughout the experimental runs. Therefore, the 13 daily tests were conducted in a controlled indoor environment with temperature patterns similar to those obtained in the outdoor test (in Figure 25). The feed was heated using an electric immersion heating element and its temperature was varied continuously using a temperature controller to match the temperature pattern obtained in the outdoor test. This technique was adopted before in Hejazi et al. [74]. As can be seen in Figure 29, the feed temperature pattern generated in the indoor environment is in good agreement with the outdoor temperature profile.

In order to account for the worst-case scenario, the tests were conducted without feed agitation. Moreover, after the end of each daily test, the membrane was taken outside the feed container and left to dry overnight without rinsing or cleaning. This daily shutdown protocol was found to result in a fast decline in the permeate quality in solar-powered MD systems [37,74].

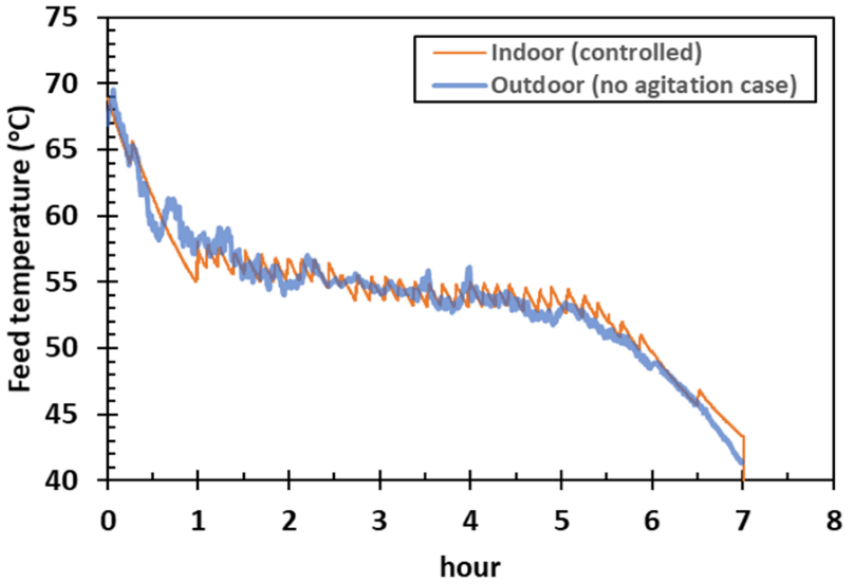

Figure 29. The Feed Temperature Profiles of a One-Day Test in an Indoor Controlled Environment and in the Outdoor Test.

Figure 30 shows the hourly permeate flux, the average daily permeate flux, and the hourly permeate quality throughout the 13-days test. Several comments can be made based on this chart:

- In general, the performance of the system in terms of water production and quality was found to be stable over 91 hours of operation. The average daily permeate flux during the first 8 days varied between 7.8 to 8.6 $kg \cdot m^{-2} \cdot h^{-1}$ (with a mean value of 8.3 $kg \cdot m^{-2} \cdot h^{-1}$ and a standard deviation of ± 0.3 $kg \cdot m^{-2} \cdot h^{-1}$), which is in line with the results obtained

from the outdoor test without feed agitation (i.e. 8.6 $kg \cdot m^{-2} \cdot h^{-1}$, as shown in Table 2). Interestingly, the average daily flux relatively increased in the next five days (varied between 9.0 to 9.8 $kg \cdot m^{-2} \cdot h^{-1}$ with a mean value of 9.3 and a standard deviation of 0.3 $kg \cdot m^{-2} \cdot h^{-1}$). This might be attributed to a partial wetting which could lead to an increase in the permeate flux due to wetting of some pores [75]. This can be further explained by the noticeable increase in the permeate conductivity starting from day 9.

- The permeate conductivity was maintained well below the minimum conductivity of drinkable water. These results contradict the findings by Li et al. [37], who tested a similar membrane using a synthetic NaCl solution (at 35,000 ppm) as the feed. In their cross-flow VMD experiment, a rapid decline in the permeate quality was reported within 4 days when the membrane was not rinsed at the end of each daily run.
- The use of RO retentate starting from day 7 seems to affect the permeate quality even though the RO retentate had a lower TDS value compared to the synthetic NaCl feed. One possible reason for this may be due to the presence of organic compounds in the RO retentate, which could decrease the surface tension of the feed, leading to a partial pore wetting [75].
- It can be noted that the permeate conductivity at the first hour of each daily test was relatively higher compared to the next six hours. This trend was noticeable throughout the 13 days of experimental runs. A similar behavior was reported before in a simulated solar-powered DCMD system [74]. This may be because, during the overnight natural drying process, small salt deposits are formed on the membrane surface and inside the partially wetted pores. During the first hour of the daily operation, the membrane is

washed out by the permeate vapor, and consequently the permeate flux improved in the following hours.

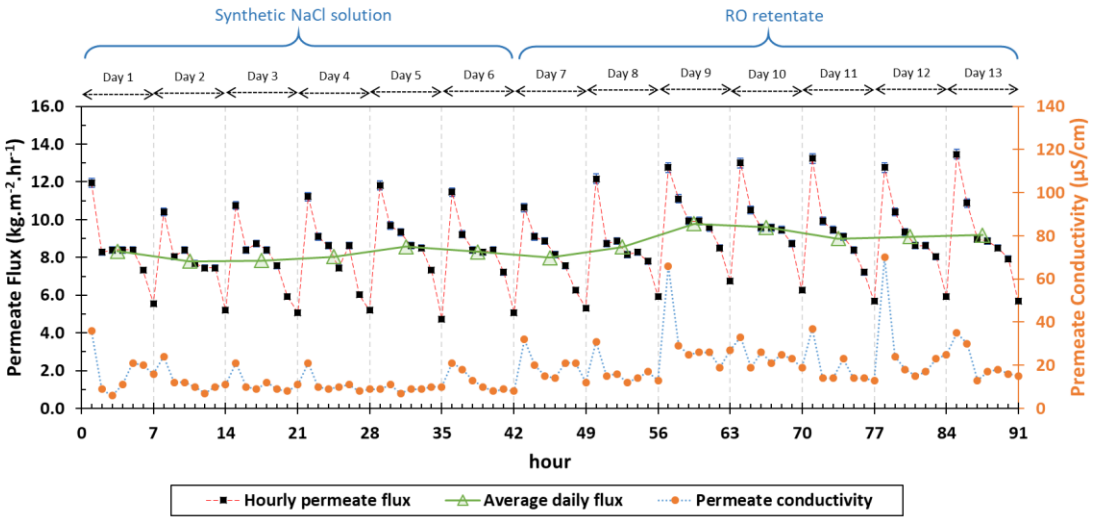

Figure 30. The Performance of the S-VMD System Over 13 Days (P_v = -94.5 ± 1.0 kPa).

It is important to note that the permeate flux and water quality may decline at a faster rate if high concentrated feed is used, considering the fact that membrane wetting is a critical challenge in the VMD configuration. In this context, agitation techniques can play an important role not only to enhance the permeate flux due to reduction of temperature polarization [54,62], but also to mitigate membrane scaling, delay flux decline, and produce better quality water as researchers have observed [54,62]. Moreover, membrane cleaning techniques such as air backwash washing were found to be effective to restore the membrane's integrity in submerged MD systems [61]. These parameters will be deeply investigated and reported in future work.

4.3 Summary

The performance of a solar–heated submerged vacuum membrane distillation (S–VMD) system that uses solar evacuated tubes as the feed container was investigated experimentally. The system eliminated the need of feed pumping, resulting in lower energy consumption and lower heat loss due to recirculation and reheating. The small–scale design represents a simple yet effective solution to provide fresh water from concentrated brine.

The functionality of the S–VMD system was demonstrated first indoors under steady–state operating conditions. The effects of two feed agitation strategies (aeration and internal circulation) were examined. Both strategies were able to minimize the effect of temperature polarization and enhance the permeate flux when compared to the case without agitation. The enhancement ratio was greater with higher rates of aeration and circulation.

The outdoor tests of the S–VMD system revealed that it can operate under different radiation and weather profiles. On a sunny day without agitation, the system can achieve an average hourly permeate flux of 8.5 $kg \cdot m^{-2} \cdot h^{-1}$. Aeration and internal circulation improved the average permeate flux by 10% and 22%, respectively. The daily water production can reach 6.7 kg, using 1 m^2 of solar absorbing area and a total membrane area of 0.1 m^2, with a thermal efficiency of 0.51.

In future work, it will be important to study the system's performance using high concentrated brine water and to investigate the long–term effects of agitation techniques on the membrane's durability and the distillate water quality.

5 PERFORMANCE ENHANCEMENT OF A SUBMERGED VACUUM MEMBRANE DISTILLATION SYSTEM USING LOW-POWER ULTRASOUND[3]

Membrane distillation (MD) is a thermally driven desalination method that uses a microporous hydrophobic membrane as a physical barrier between a hot feed side (e.g. seawater or inland water) and a cold permeate side [4,17]. Vapor transfers from the feed side to the permeate side as a result of the difference in partial pressure across the membrane wall. The vapor can either condense inside the MD modules as in direct contact MD (DCMD) and air gap MD (AGMD) configurations, or in an external condenser as in sweeping gas MD (SGMD) and vacuum MD (VMD) configurations [76].

MD can be classified on the basis of the feed water mechanism into cross-flow and submerged configurations. Cross-flow MD systems are considered the default configuration, where the feed is pumped through an MD module with feed inlet and outlet. Recently, researchers have suggested a submerged MD (S-MD) configuration, where the membranes are directly submerged within the feed tank that is heated by an electric heating element. This eliminates the need for circulating pumps and minimizes heat loss that exists in the cross-flow configuration due to recirculation and reheating. S-MD has been mainly applied to treat high concentration feed water such as inland brine [53,54], seawater RO brine [55], and coal-seam-gas-produced water [56].

---

[3] Submitted for publication as:
Bamasag, A., Daghooghi-Mobarakeh, H., Alqahtani, T., & Phelan, P. E. (2020). Performance enhancement of a submerged vacuum membrane distillation (S-VMD) system using low-power ultrasound.

One major drawback of S-MD systems is that they lack feed turbulence, which may worsen the effects of temperature and concentration polarizations, leading to lower permeate flux and faster membrane fouling. Therefore, various agitation techniques were applied to tackle this challenge, including transverse vibration [53,54,62], stirring [52,55,62], and aeration [53,54]. These methods reportedly enhanced permeate flux and reduced membrane fouling and scaling. For example, Meng et al. found that, in a submerged VMD system, applying transverse vibration can improve the permeate flux by 21% compared to the case without agitation [53]. More recently, Bamasag et al. found that circulation and aeration can significantly improve the permeate flux in submerged VMD [77].

One potential enhancement method that has not been studied in S-MD systems yet is ultrasound energy. In fact, ultrasound energy has been used to enhance thermal-based processes such as heat exchangers, phase change, and desorption processes [78,79]. Moreover, ultrasound energy was integrated before with membrane-based water treatment technologies such as Ultrafiltration (UF) and Microfiltration (MF) mainly to mitigate membrane fouling [80]. More relevantly, US irradiation has been integrated before with conventional cross-flow MD systems under the AGMD [81,82] and DCMD [83] configurations. Generally speaking, ultrasound energy was found to be effective in increasing the permeate flux and reducing membrane fouling and scaling.

To our knowledge, the first work that integrated ultrasound with MD was conducted by Zhu et al [82]. They found that the permeate flux in an ultrasonic-assisted AGMD system can be improved by up to 25% compared to that with no ultrasonic irradiation. The

improvement was attributed to a reduction in the temperature polarization caused by microstreaming and cavitation mechanisms.

Hou et al. studied the performance of an ultrasonic-assisted DCMD process using hollow fiber membranes [83]. It was reported that the permeate flux can be enhanced between 5% to 60% depending on the operating conditions. The enhancement ratio (i.e. the permeate flux with US to that with no US) can be enlarged at lower feed temperature and velocity, and low frequency as well as higher feed concentration and higher ultrasonic power. In subsequent studies, the same group illustrated how the use of US can mitigate $CaSO_4$ membrane scaling [84] and silica fouling [85] and maintain a more stable permeate flux in a DCMD system.

Recently, Naji et al. studied the effect of directly attached low-power ultrasound on the performance of a cross-flow AGMD using a flat sheet membrane [81]. The authors reported an enhancement on the permeate flux after extended operation, which was attributed only to the acoustic streaming effects that improved mass transfer and membrane cleaning.

It is worth noting that ultrasound was also used as an off-line membrane cleaning method. Hejazi et al. reported that ultrasonic cleaning helped to restore the hydrophobicity of used membranes [74]. Cho et al. applied ultrasonic cleaning on fouled membranes, and they found it is more efficient in removing membrane foulants and recovering the flux when compared to conventional physical and chemical cleaning techniques [86]. However, the authors reported a structural damage or wetting of the MD membranes when high ultrasonic power at low frequencies (150 and 300 W at 28 and 45 kHz) are used.

The goal of this chapter is to experimentally investigate the use of ultrasonic energy as an agitation technique in a submerged vacuum membrane distillation (S-VMD) system. The effect of ultrasonic power and frequency on the permeate flux with different feed temperatures and concentrations will be studied. The enhanced transport phenomena associated with application of ultrasound in the S-VMD systems are investigated and mechanisms which dominantly contribute are identified and quantified. Finally, a relatively long-duration test was conducted to investigate the effect of ultrasound on the permeate flux and water quality. The study represents the first attempt to apply ultrasonic energy in an S-VMD system, and it will add substantially to our understanding of integrating ultrasound with different MD processes.

5.1 Materials and Methodology

5.1.1 Membrane and Module Specifications

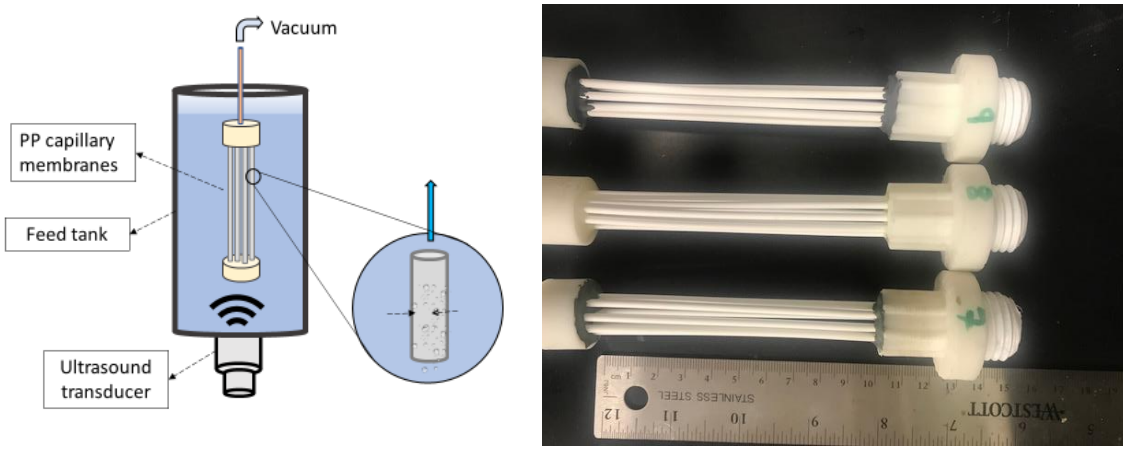

Figure 31. A Schematic Diagram (Left) and a Photograph (Right) of the S-VMD Modules.

Figure 31 shows a schematic and a photograph of the proposed US-assisted S-VMD system. A membrane module is submerged in a container filled with feed water, which is

heated internally by a tubing coil. An ultrasonic transducer is directly attached to the bottom of the feed container. The module consists of eight hydrophobic capillary membranes with effective length of 9.7 ± 0.1 cm and a surface area of 43.9 ± 0.5 cm^2. The membranes were potted manually using epoxy resin with a "dead-end" bottom side and a top side connected to the vacuum line. The physical characteristics of the membranes and the container are shown in Table 7.

Table 7 Characteristics of the S-VMD Module

Membrane manufacturer	Microdyn-Nadir
Membrane material	Polypropylene
Pore size (μm)	0.2
Porosity	0.7
Tortuosity	1.4
Capillary inner diameter (mm)	1.8
Capillary outer diameter (mm)	2.7
Capillary thickness (μm)	450
Number of membrane capillaries	8
Length of membrane (cm)	9.7
Membrane surface area A_m (m^2)	0.0044
Container diameter (cm)	44
Container length (cm)	58
Container capacity (L)	0.55

5.1.2 Experimental Setup and Procedure

A schematic diagram of the experimental setup is shown in Figure 32. The feed solution is heated by a tubing coil with pure water as the heat transfer fluid. The pure water is circulated by a temperature-controlled hot water bath (Thermo Haake DC 10-P5), which is adjusted to achieve the required feed temperature. In contrast to the conventional heating method in S-VMD which uses an electric immersion heating element placed on the top of

the container, the heating method in the current design provides a more uniform thermal distribution and ensures consistent heat supply in all experimental runs.

Considering the diameter of the heating coil relative to the diameter of the feed tank and the feed tank's height relative to its radius ($O(L_{FT}/r_{FT})\sim10$), radial temperature measurement was deemed to be unnecessary. The feed solution temperature was measured at two different locations using OMEGA K- type thermocouples (wire diameter = 0.571 mm), referred to as top-axial and bottom-axial temperatures, and a NATIONAL INSTRUMENTS data acquisition device NI cDAQ-9171.

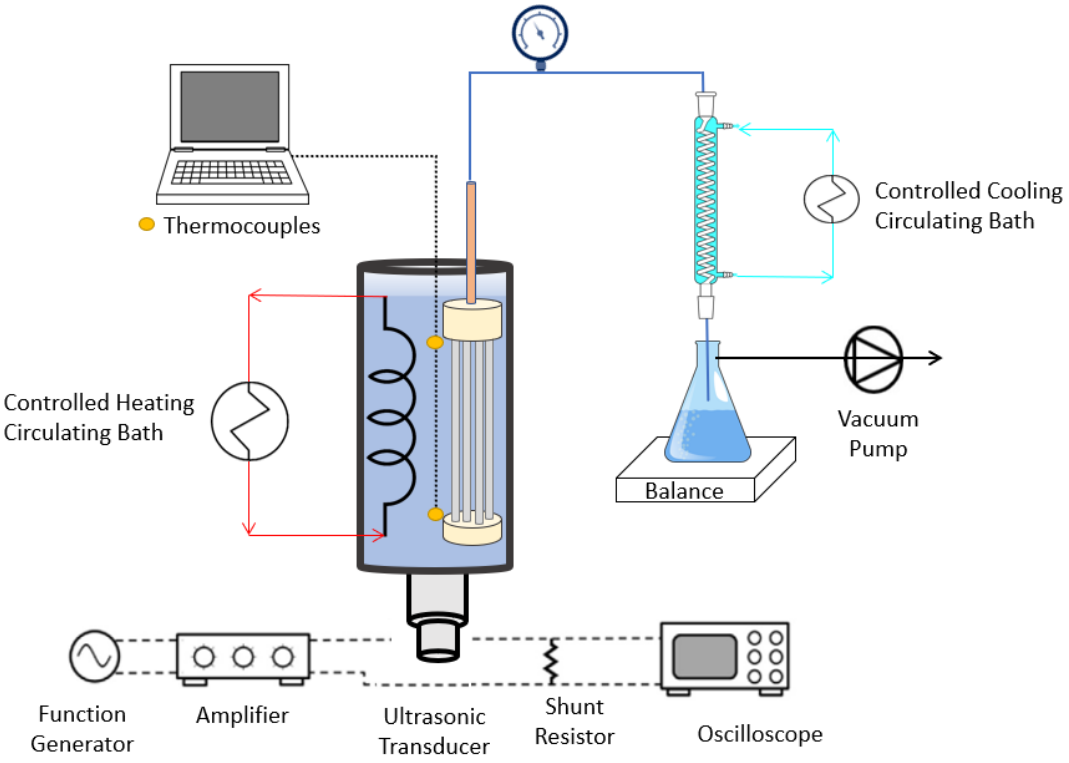

Figure 32. A Schematic Diagram of the Experimental Setup.

A vacuum pump is used to create a vacuum pressure (-93.5 ± 0.5 kPa) on the permeate side of the membranes. The pressure was monitored using a digital pressure gauge. An external condenser liquefies the water vapor generated by the distillation process using

cold pure water at 5 °C, which is supplied by a thermal circulating bath (Col-Parmer EW-12122-42). The amount of distillate water is measured using an electronic scale. The permeate flux J (in $kg \cdot m^{-2} \cdot h^{-1}$) is calculated as:

$$J = \frac{m}{A_m \Delta t} \tag{5.1}$$

where m_d is the amount of distillate water (kg), A_m the membrane area (m^2), and t the sampling period (h). The permeate water quality is measured by a portable electrical conductivity meter (HM EC-3).

The main constituent elements of the ultrasonic unit used in this study are a function generator (Siglent Technologies SDG1032X), a high frequency-low slew rate amplifier (AALABSYSTEMS A-303), a shunt resistor and two ultrasonic power transducers of different resonant frequencies. The ultrasonic power transducers used are of low-heat, high-efficiency piezoceramic type acquired from APC INTERNATIONAL, LTD. The ultrasonic transducer and the shunt resistor were connected in series and with the help of four voltage probes, the impedance of the transducer based on the voltages across the transducer and across the shunt resistor was measured. The resonant frequency corresponds to the lowest impedance (also the phase difference between the voltage and current is zero). The resonant frequencies of the unloaded transducers given by the supplier, 28 kHz-50 W (APC 90-4040) and 40 kHz-50 W (APC 90-4050), were verified and the resonant frequencies of the loaded transducer-feed tank assembly were determined to be 27.55 and 39.65 kHz, respectively. Instead of using a commercially available ultrasonic generator with a fixed or limited power and frequency output, an integration of function generator and amplifier which allows for the transducer to be powered at any desirable power level and frequency was used. The ultrasonic power was determined as:

$$P_{US} = V_{rms}\, I_{rms}\, \cos\theta \qquad (5.2)$$

where V_{rms} is the root mean square voltage across the transducer, I_{rms} the root mean square alternating current passing through the transducer, and θ the phase angle between the voltage and current. In order to avoid any structural damage and in consideration of minimizing energy consumption, low levels of ultrasonic power of 10 and 30 W were considered [81].

Short-term experimental runs were conducted to study the enhancement effect of ultrasonic power and frequency on the permeate flux. Different feed temperatures (45, 55, and 65 °C) and different feed concentration (pure water, 35, 100, 200 g/L) were tested. At the completion of each experimental run, the membranes are taken outside the container to be rinsed and cleaned. A similar experimental procedure was conducted to measure the time-evolution of permeate flux and quality for a relatively long operation. At the end of these tests, the membranes were characterized with scanning electron microscopy (SEM)

5.1.3 Uncertainty Analysis

The accuracy of the measured variables was calculated to be ± 0.01 g, ± 0.4 °C, and ± 0.5 cm^2 for mass, temperature, and membrane surface area, respectively. The vacuum pressure and feed temperature were controlled within ± 0.5 kPa and 0.5 °C, respectively. To show a reasonable reproducibility, repeated readings were obtained with a maximum standard deviation of 2.7%. To determine the errors in the calculated variables (i.e. J and Φ), the expanded uncertainty method was adopted to achieve a high level of confidence (~95%) [44]. The details of the uncertainty analysis are presented in a previous work [64].

5.2 Results and Discussion

5.2.1 The Performance of the Ultrasonic-Assisted S-VMD with Feed Temperature

The effect of the ultrasonic power and frequency on the permeate flux (J) under steady-state operating conditions was measured. The bulk feed temperature $T_{f,b}$ was kept at 45, 55, and 65 ^{o}C, and a 35 g/l NaCl solution was used as the feed water (TDS of standard seawater). The experiments were carried out with and without ultrasonic energy at two levels of power (10 and 30 Watts) and two values of frequency (28 and 40 kHz).

The values of J as a function of the feed temperature (± 0.5 ^{o}C) with and without ultrasonic energy at a frequency of 40 kHz and 28 kHz are shown in Figs. 3(a) and 3(b), respectively. As expected, in all cases, higher values of J are achieved with higher feed temperature. This is because J increases linearly with the difference in the vapor partial pressure across the membrane wall [9,17]:

$$J = K\left(P_{f,m} - P_v\right) \tag{5.3}$$

where K is the mass transfer coefficient (kg·Pa^{-1}·m^{-2}·h^{-1}), $P_{f,m}$ the feed vapor pressure at the membrane surface, and P_v the vacuum pressure on the permeate side. While K and P_v are almost constant in all cases, $P_{f,m}$ is exponentially related to temperature at the membrane surface ($T_{f,m}$) according to Antoine's equation [17].

Apparently, Figs. 3(a) and 3(b) show that applying ultrasonic energy using different values of power and frequency in the S-VMD improved the permeate flux relative to the case without ultrasonic energy, under similar feed temperatures. This finding is in line with previous research which reported improvement in permeate flux in S-VMD systems using other agitation techniques such as aeration or circulation [53,62].

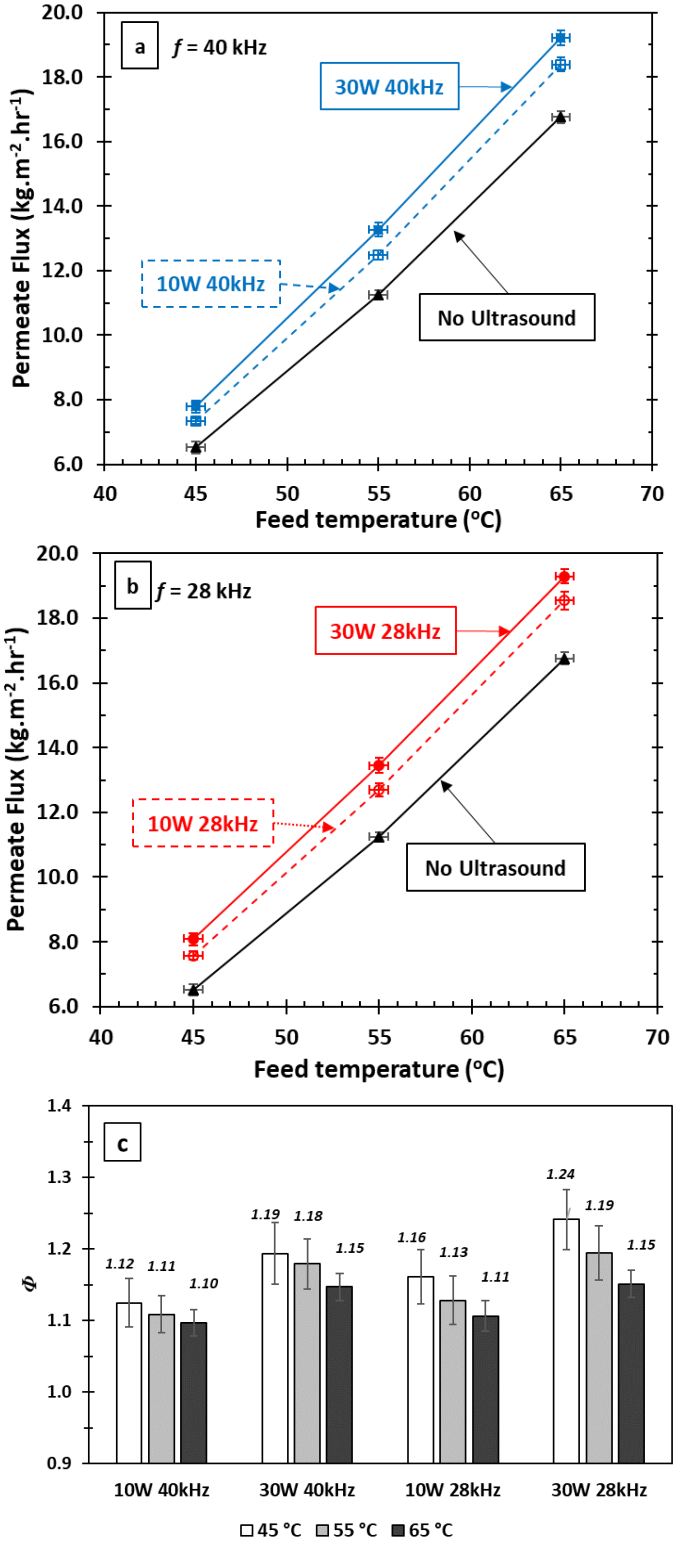

Figure 33. Permeate Flux J with and without Ultrasound at (a) f = 40 kHz, and (b) f = 28 kHz, and (c) the Flux Enhancement Ratio Φ (P_v = -93.5 ± 0.5 kPa, Feed Concentration = 35 g/L).

It is important to note that, in submerged MD systems, the effect of temperature polarization is more significant due to the lack of turbulence relative to that in cross-flow MD systems. In other words, S-MD suffers from a larger difference between the feed temperature at the membrane surface and that at the bulk phase ($T_{f,b}$ - $T_{f,m}$) which is a result of the presence of a boundary layer and the heat loss due to evaporation at the membrane surface [18]. Thus, applying ultrasonic energy can reduce the effect of temperature polarization (i.e. lower boundary layer resistance) resulting in higher $T_{f,m}$ and therefore a higher permeate flux as described in Eq. (5.3).

In order to accurately measure the enhancement effect of ultrasound with different values of power and frequency, the permeate flux enhancement ratio Φ can be used:

$$\Phi = \frac{J_{US}}{J_{non-US}} \tag{5.4}$$

where J_{US} and $J_{non\text{-}US}$ are the measured permeate fluxes of the S-VMD with ultrasound and without ultrasound under the same operating conditions, respectively.

The values of Φ for two values of ultrasonic power and frequency under different $T_{f,b}$ is shown in Figure 33(c). It is clear that, in general, applying higher power and lower frequency results in better values of Φ. This is in agreement with what is reported in the literature in ultrasonic-assisted MD systems under cross-flow configuration [82,84].

Moreover, it can be noted that the use of ultrasonic energy (under the same power and frequency) is more effective in terms of Φ with lower $T_{f,b}$. This occurred despite the fact that the effect of temperature polarization is expected to be higher at high values of $T_{f,b}$ [18] and so the ultrasonic energy is expected to perform better at higher $T_{f,b}$. This raises questions about dominating mechanisms associated with ultrasound enhancement in the S-

VMD and the role the feed temperature plays. This is discussed in detail in the following section.

5.2.2 Identifying the Ultrasonic Enhancing Mechanisms

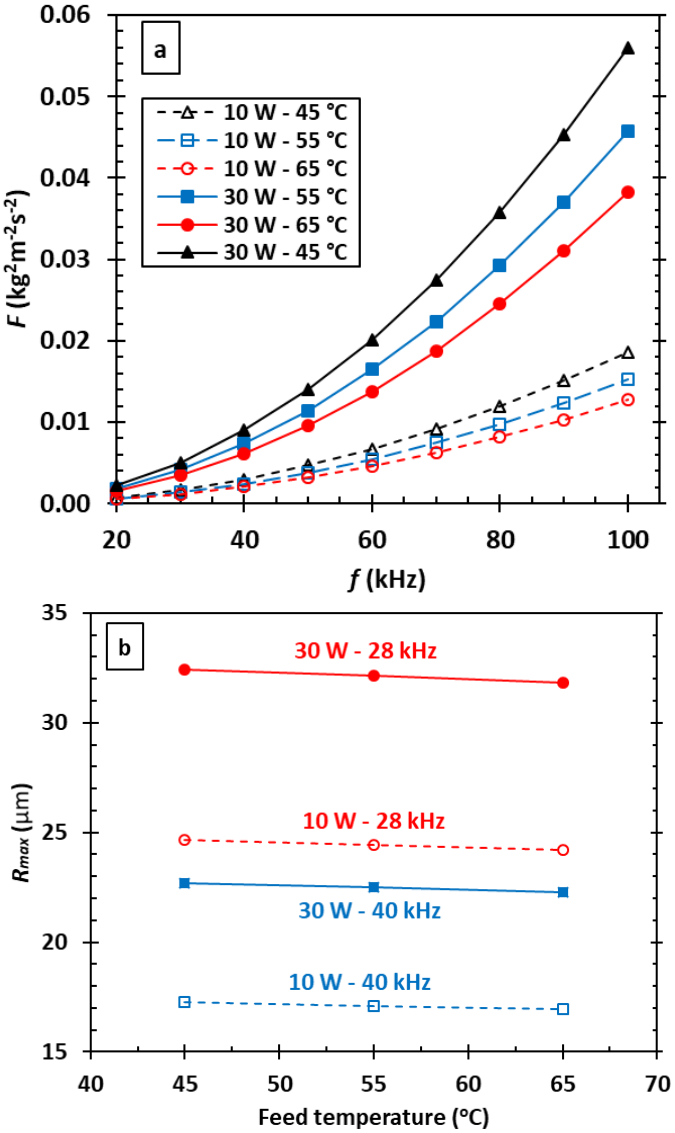

Figure 34. The Variation of Kinematic Momentum (a) and (b) Critical Cavitation Bubble Radius with Ultrasonic Power, Frequency, and Feed Water Temperature.

The ultrasound-induced improvement in permeate flux can be explained through heat and mass transfer enhancing mechanisms associated with application of ultrasound in MD

[80–82,84,86,87]. Commonly postulated in the literature and main contributor mechanisms to ultrasound-enhanced heat and mass transfer phenomena are *acoustic streaming* and *acoustic cavitation* and other minor mechanisms including but not limited to *microstreaming*, *surface cavitation*, *turbulent boundary layer alteration*, and *enhanced diffusion* [78,79,96,88–95]. The real challenge is to identify the degree to which these mechanisms contribute to the enhancement. Investigating the effects of frequency at which ultrasound is applied is the key parameter to fundamentally understand the ultrasound-induced enhancement in permeate flux as acoustic streaming effects intensify with an increase in frequency and acoustic cavitation effects amplify with a decrease in frequency [88,91,92,97,98]. The ultrasonically induced kinematic momentum *F* resulting in acoustic streaming of a fluidic medium is defined as [91]:

$$F = \frac{\rho W_{US}}{c}(1 - e^{-2\alpha x}) \tag{5.5}$$

where ρ is the fluid density, c the speed of sound in the fluidic medium, W_{US} the ultrasonic power, α the acoustic attenuation coefficient of the fluidic medium and x the distance from the ultrasound emitting source. Considering an arbitrary point in the middle of the feed tank ($x = 0.1\ m$), the variation of kinematic momentum with frequency for both power levels and three feed water temperatures is depicted in Figure 34(a). As it can be inferred from the figure, the ultrasonically induced kinematic momentum and consequently the acoustic streaming effect increases with an increase in frequency regardless of ultrasonic power and fluid temperature. If we consider acoustic streaming as the key player in enhancement of the permeate flux, the enhancement ratio (Φ) should increase with an increase in frequency. However, the results indicate an opposite trend as shown in Figure

33(c) and values of Φ *decrease* with an increase in frequency. So, acoustic streaming can be disregarded as the key player in ultrasound-enhanced VMDs and its effects on permeate flux enhancement can be considered as insignificant.

Acoustic cavitation is the establishment and growth of gas/vapor-filled bubbles that move around and consequently implode violently to cause microstreaming. The movement and jet-like streams due to implosion of the cavitation bubbles result in enhanced heat and mass transfer [88,92,93,99–101]. The heat and mass transfer enhancement associated with cavitation-induced effects of ultrasound is proportional to the cavitation bubble critical radius; the larger the bubbles are the more disruption they cause upon movement and the more energy released upon collapse [102,103]. The critical radius R_{max} of a cavitation bubble, which is the bubble radius right before the implosion, is determined as [88]:

$$\omega^2 \rho R_{max}^2 = 3\mu(P_a - \frac{2\sigma}{R_{max}}) \quad (5.6)$$

where ω is the angular frequency ($\omega = 2\pi f$), μ the kinematic viscosity of the fluid, P_a the acoustic pressure, and σ the surface tension of the fluid. The values of critical bubble radius for all cases of ultrasonic power, ultrasonic frequency and feed water temperature are shown in Figure 34(b). Comparing the trend in variations of Φ (Figure 33(c)) and cavitation bubble critical radius (Figure 34(b)) with regard to feed water temperature, ultrasonic power and ultrasonic frequency reveals an almost perfect hand-in hand similarity between the two: both increase as ultrasonic power increases and decrease when feed water temperature and ultrasonic frequency increase. The two are correlated with a coefficient of 95%. The inverse proportionality between permeate flux enhancement ratio and ultrasonic

frequency suggests that acoustic cavitation is the dominant contributor to the observed enhancement.

5.2.3 The Influence of Feed Temperature on the Ultrasound-Assisted Enhancement

The decline in ultrasound-induced improvement in permeate flux with an increase in feed water temperature could be explained by the cavitation effect. The maximum pressure P_{max} and temperature T_{max} attained upon bursting of a cavitation bubble are obtained as [104,105]:

$$P_{max} = P_b\left(\frac{P_l(\gamma - 1)}{P_b}\right)^{\frac{\gamma}{\gamma-1}} \tag{5.7}$$

$$T_{max} = T_l\left(\frac{P_l(\gamma - 1)}{P_b}\right) \tag{5.8}$$

where P_b is the pressure inside the bubble at its maximum size and is assumed to be equal to the vapor pressure of the liquid ($P_b = P_v@T_l$), P_l the instantaneous fluid pressure at the moment of collapse including hydraulic P_h and acoustic pressure ($P_l = P_h + P_a$), γ the specific heat ratio of the vapor/gas inside the bubble, and T_l the temperature of the fluid. With an increase in feed water temperature, the water vapor pressure increases resulting in damping the shockwave and lower implosion pressure and temperature and hence the decline in Φ [102,105].

5.2.4 The Influence of Ultrasonic Frequency on the Ultrasound-Assisted Enhancement

Although integration of ultrasound enhances the permeate flux, the frequency at which ultrasound is applied in order to achieve higher permeate flux is of major concern. As shown in Figure 33(c), the values of Φ reduce when frequency increases from 28 kHz to 40 kHz regardless of ultrasonic power and feed water temperature. It is also noteworthy

that a transducer of 120 kHz frequency was tried with a power of 30 W, but no significant improvements were observed suggesting that the ultrasonic power was not sufficient to initiate acoustic cavitation since the acoustic cavitation threshold increases with frequency [102,105] .

This is because the effects of acoustic cavitation being the major contributor to the observed enhancement decreases as frequency increases [87,88,105]. It can be argued that as frequency increases, the rarefaction cycles become shorter, and the time period necessary for the rarefaction cycle becomes too short to allow bubbles to grow to a size sufficient to cause significant disturbances in the liquid [105]. The shortness of the time period of the compression half-cycle can also affect the cavitation if it becomes shorter than the time required for the bubble to collapse. Another possible reason can be the amount of ultrasonic energy delivered to the system. The acoustic intensity I is defined as:

$$I = 2\rho c\pi^2\delta^2 f^2 \tag{5.9}$$

where δ is the acoustic displacement, and f is the ultrasonic frequency. For constant acoustic intensity in a medium, the acoustic displacement changes with frequency according to:

$$I_1 = I_2 \rightarrow \frac{\delta_2}{\delta_1} = \frac{f_1}{f_2} \tag{5.10}$$

Meaning that at constant ultrasonic intensity, acoustic displacement decreases linearly with an increase in frequency. The ultrasonic energy delivered by a transducer E_T is proportional to the acoustic displacement and is defined as [87,106]:

$$E_T = \frac{I}{c}\,\pi b^2(2\delta) \tag{5.11}$$

where b is the transducer radius. So, under constant acoustic intensity, with an increase in frequency the delivered energy by the transducer decreases, and consequently the effectiveness of integration of ultrasound decreases resulting in lower Φ.

5.2.5 The Performance of the Ultrasonic-Assisted S-VMD with Feed Concentration

The effect of the ultrasonic energy with different concentrations of NaCl solutions was also examined. In these experimental runs, the feed temperature was fixed at 55 ^{o}C, whereas the ultrasonic power and frequency were set at 30 W and 40 kHz, respectively. As shown in Figure 35(a), the permeate flux declines with an increase in feed concentration with and without ultrasonic energy. This is expected as the presence of salt reduces the vapor partial pressure of the feed which negatively affects the driving force as described in Eq. (5.3). Moreover, the effect of concentration polarization (i.e. higher concentration at the membrane surface relative to that at the bulk phase of the feed) worsens as both the feed viscosity and the boundary layer thickness increase with higher feed concentration.

Figure 35(a) also indicates that ultrasonic energy enhanced the permeate flux when compared to the case without ultrasonic energy at the same feed concentration. While the absolute values of J decreased with increasing the feed concentration as discussed above, the enhancement ratio Φ was better at higher concentration as shown in Figure 35(b), which is consistent with what others reported in the literature [82,83]. This clearly suggests that ultrasonic energy can play a role in mitigating the effect of concentration polarization, which is mainly attributed to the cavitation effects that potentially enhance the mass transfer process at the membrane-liquid interface.

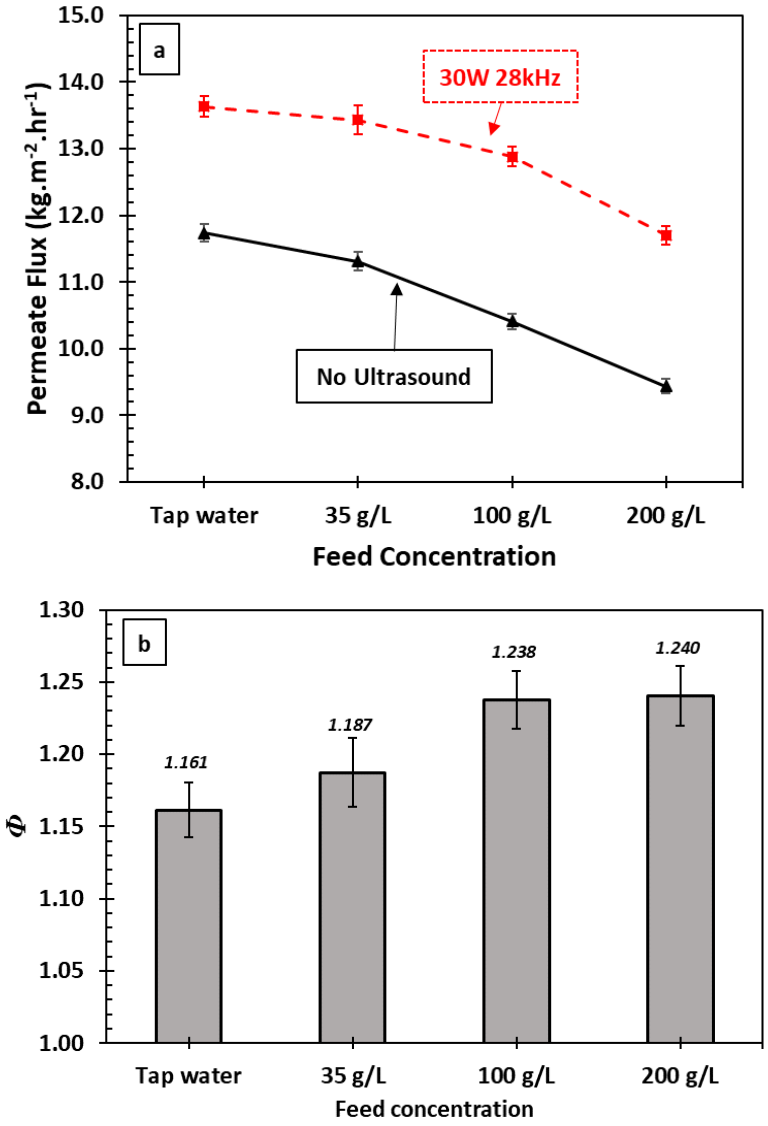

Figure 35. (a) Permeate flux J and (b) the Flux Enhancement Ratio Φ as a Function of Feed Concentration with and without Ultrasound. (P_v = -93.5 ± 0.5 kPa, $T_{f,b}$ = 55 °C, W_{US} = 30 W, and f = 40 kHz).

To clarify this, it is necessary to note that impurities and molecular discontinuity play a crucial role in acoustic cavitation. It is very difficult to induce cavitation in pure liquids and requires high levels of acoustic intensity to initiate acoustic cavitation. The presence of impurities and dissolved particles of particulate matter (level of hydrophobicity) provides nooks and crannies that could trap and host gas/vapor nuclei, thus lowering the

cavitation threshold. Another advantage of impurities and dissolved particles is that they lower the surface tension of the liquid resulting in lower acoustic cavitation threshold [102].

5.2.6 Long-term Operation

Membrane scaling represents a serious challenge particularly for S-VMD configuration [61]. Because of the lack of feed turbulence, inorganic salts can accumulate at a faster rate causing pore blocking and consequently reducing the permeate flux and its quality. While researchers reported that ultrasound significantly helped to mitigate membrane scaling in DCMD [84,85] and AGMD [81] systems under the cross-flow configuration, the effect of ultrasound to reduce membrane scaling in the submerged configuration is not clear yet. Moreover, it was reported that applying ultrasound in MD can cause structural damage and wetting of the membranes, especially if high power were used. Thus, it is important to investigate if applying ultrasonic energy in S-VMD would mitigate membrane scaling, and whether it causes structural damage of the membrane.

In this section, long-term tests (~15 to 16 hours) were conducted with and without applying ultrasound using two new modules. Because of power restrictions, the ultrasonic transducer operates in an intermittent cycle (5 minutes ON - 5 minutes OFF). A synthetic NaCl solution with an initial concentration of 100 g/l was used as the feed water and its temperature was kept at 65 ^{o}C. The feed volume was kept constant by adding 15 ml of the feed every 10 minutes to compensate for the decline in the water level. The experiments were terminated when the feed concentration reached a point very close to the supersaturation limit (~350 g/l).

Figure 36 shows the variation of permeate flux and conductivity as a function of feed concentration factor (i.e. the ratio of the feed concentration at a certain time to the initial concentration) with and without ultrasound. As expected, the permeate flux in both cases gradually declined as the feed concentration increased with time. While the permeate flux in both cases was very close when the concentration factor is less than 2.8, the case with ultrasound seems to perform better overall, but not significantly (up to 10% increase). This can be attributed to the intermittent nature of applying ultrasound in the long-term operation. Another reason is that the enhancement ratio after applying ultrasound is diminished with higher feed temperature, as discussed above.

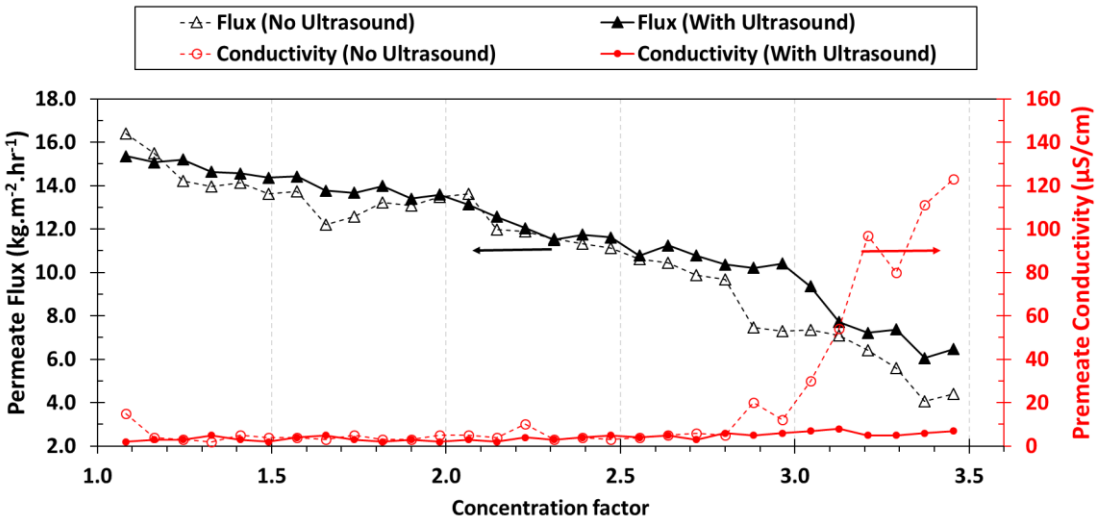

Figure 36. The Variation of Permeate Flux J and Conductivity as a Function of Feed Concentration Factor with and without Ultrasound. (P_v = -93.5 ± 0.5 kPa, $T_{f,b}$ = 65 ^{o}C, Initial NaCl Concentration = 100 g/l, W_{US} = 30 W, and f = 40 kHz).

Interestingly, as the concentration factor reached ~2.8, a rapid decline in the flux was observed in the test with no ultrasound. Starting from this point until the end of operation, the effect of ultrasound energy was more obvious as the permeate flux was remarkably higher compared to the case with no ultrasound. This can be explained as follows: as the

concentration factor reaches a point close to supersaturation, the feed concentration on the membrane surface can be greater than the metastability limit of NaCl solution, considering the polarization effect. This can lead to accumulation and crystallization of salt on the membrane surface, which can consequently block the membrane pores and cause penetration of salt crystals into the pores. This phenomenon is especially problematic when there is no feed agitation [62] and can cause a rapid decrease in the flux as in the case with no ultrasound.

To evaluate this closely, SEM/EDS analysis was conducted at the end of each long-duration test. Figure 37 shows SEM/EDS images of the membrane surface and cross section with and without applying ultrasound. The SEM images shows larger salt crystals deposited on the membrane surface, in the case without ultrasound. This could block the membrane pores and allow partial salt penetration to the permeate side. In the case with ultrasound, however, the deposition of salt on the membrane surface was relatively low. Moreover, the EDS analysis show a much lower deposition of Sodium salts in the case with ultrasound. This suggests that applying ultrasound in an MD process can operate as a cleaning technique that mitigates membrane scaling as reported in the literature [81,86]. The agitation effects caused by the ultrasonic waves can continuously stimulate the feed-membrane interface, preventing the formation of salt crystals on the membrane surface.

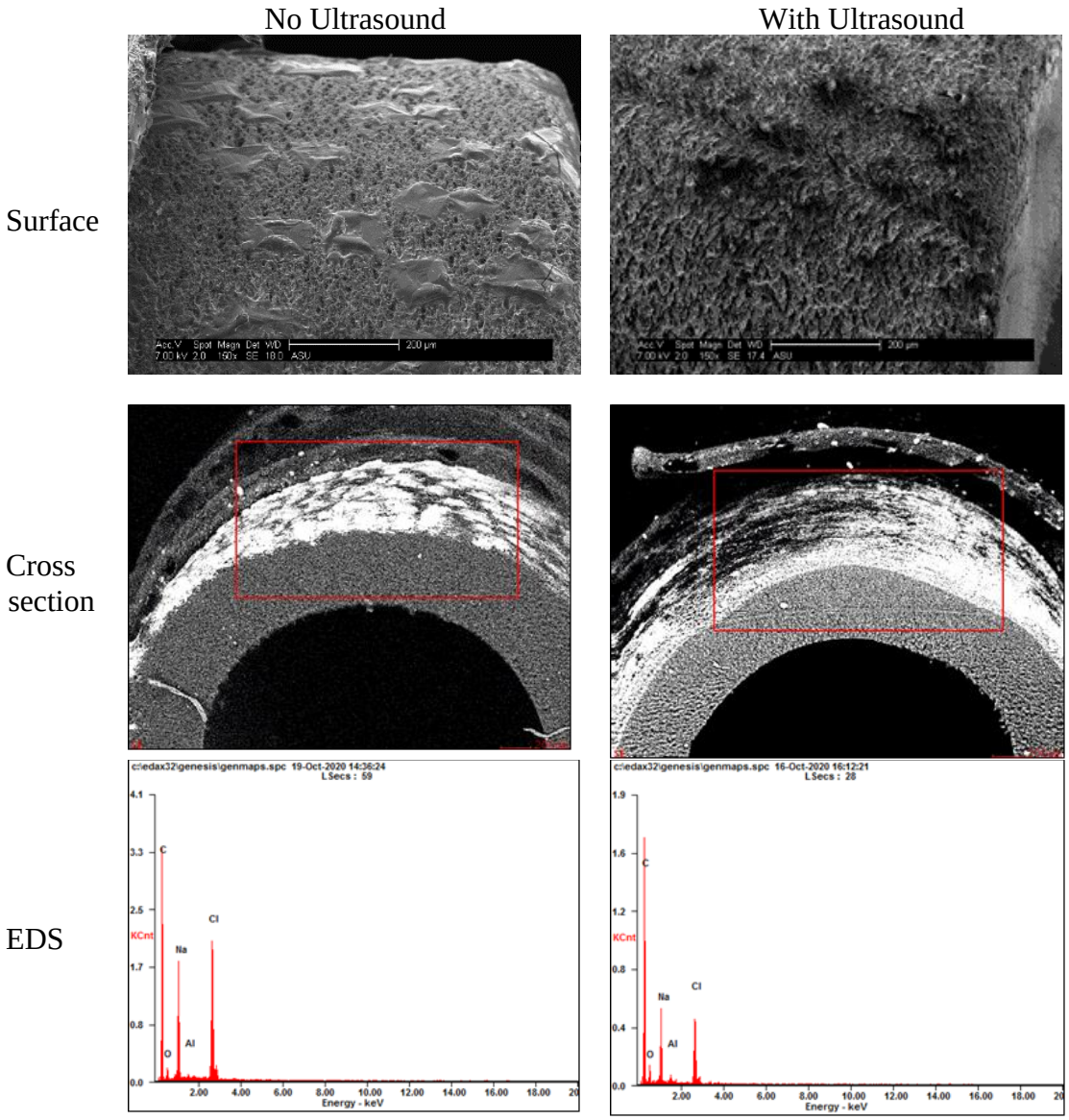

Figure 37. SEM/EDS of Membrane Surface and Cross Section at the End of the Long-Duration Test with And without Ultrasound.

With regard to the permeate quality, it can be seen in Figure 36 that the permeate conductivity increased remarkably (up to 123 µS/cm) when the concentration factor reached ~3.1 in the test with no ultrasound, which is possibly caused by partial penetration of salt crystals. However, the conductivity was maintained well below the conductivity of drinkable water, which means that the membrane did not suffer from pore wetting. On the

other hand, the salt rejection was very high in the ultrasonic test and the permeate quality was maintained below 10 µS/cm throughout the experiment. This indicates that ultrasound can mitigate salt crystallization on the membrane surface and prevent penetration of salt crystals into the pores. It also suggests that ultrasound did not cause pore wetting or structural damage of the membrane. In future work, it is important to investigate the effect of ultrasonic energy to mitigate membrane scaling and fouling in a S-VMD system using even higher concentration feed water (e.g. inland brine or oil-produced water).

5.2.7 Enhancement in Specific Energy Consumption

While previous studies focused on how ultrasound can enhance permeate flux and mitigate fouling in MD processes, the effect of applying ultrasound on energy consumption was not apparently addressed. In other words, it not yet clear whether the added power required to apply ultrasound can achieve better energy consumption per unit mass of distillate water produced.

In order to investigate this, the results obtained in section 5.2.1 are used to calculate the ultrasonic enhanced specific energy consumption (*UESEC*), which compares the specific energy consumption with applying ultrasound (SEC_{US}) to the case without ultrasound ($SEC_{NO\text{-}US}$):

$$UESEC = \frac{SEC_{NO-US} - SEC_{US}}{SEC_{NO-US}} \tag{5.12}$$

SEC calculates how much energy is required to produce a unit mass of freshwater (in kWh/kg). *SEC* is divided into specific thermal energy consumption (*STEC*) and specific electric energy consumption (*SEEC*) [107,108]:

$$SEC = STEC + SEEC \tag{5.13}$$

STEC can be defined as the amount of thermal energy ($\dot{Q}_{heat}$) required to produce a unit mass of distillate water ($\dot{m}_d$):

$$STEC = \frac{\dot{Q}_{heat}}{\dot{m}_d} = \frac{\dot{m}_{HTF} C_p \Delta T_{HTF}}{\dot{m}_d} \tag{5.14}$$

where $\dot{m}_{HTF}$ is the mass flow rate of the heat transfer fluid, C_p the specific heat, and ΔT_{HTF} the temperature drop of the heat transfer fluid in the heating coil.

Similarly, *SEEC* takes into account the total amount of electric energy required ($\dot{W}$):

$$SEEC = \frac{\sum \dot{W}}{\dot{m}_d} = \frac{\dot{W}_{vaccum} + \dot{W}_{US}}{\dot{m}_d} \tag{5.15}$$

where $\dot{W}$ is the combination of the power required for the ultrasonic transducer ($\dot{W}_{US}$) and that for the vacuum pump ($\dot{W}_{vaccum}$). For our lab-scale system, the rating power of the vacuum pump (168 W) is used for $\dot{W}_{vaccum}$ [107].

Figure 38 illustrates the *UESEC* for different ultrasonic power and frequency at different feed temperatures according to Eq. (5.12). It is clear that applying ultrasound in the S-VMD system resulted in a better utilization of energy (i.e. less energy per unit mass of distillate water), which is similar to the observed enhancement in permeate flux (Figure 33(c)). The values of *UESEC* were better with increasing the ultrasonic power from 10 W to 30 W, irrespective of the change in ultrasonic frequency or feed temperature. This indicates that the added power required to operate the ultrasonic transducers not only increases the amount of distillate water, but it is more effective in terms of energy

consumption. These findings are in agreement with a recent study which found that feed agitation using circulating pumps in an S-VMD can enhance its energy efficiency [109].

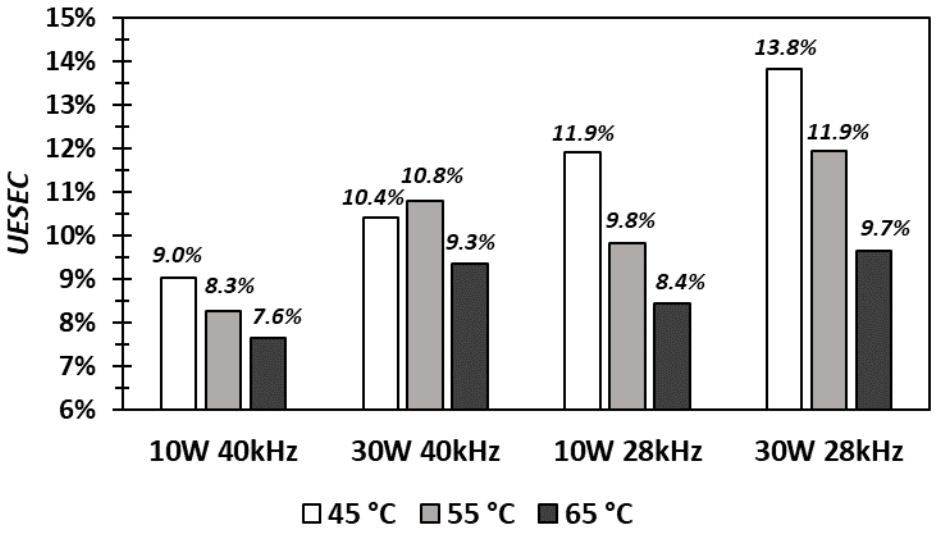

Figure 38. The Ultrasonic Enhanced Specific Energy Consumption (*UESEC*) (P_v = -93.5 ± 0.5 kPa, Feed Concentration = 35 g/L).

5.3 Summary

The performance of an ultrasonic-assisted submerged vacuum membrane distillation (S-VMD) system was investigated experimentally. To do so, the effects of the ultrasonic power and frequency on the permeate flux were demonstrated under different feed temperatures and concentrations. Moreover, the effects of ultrasound energy in a relatively long-term operation using high concentration NaCl solution were also examined. From the investigations, the following conclusions were made:

- Applying low-power ultrasound in the S-VMD enabled it to improve the permeate flux when compared to the case without feed agitation (up to 24%).

- The enhancement ratio was more pronounced with an increase in the ultrasonic power and feed concentration as well as a decrease in the ultrasonic frequency and feed temperature.
- Based on the observed variation of the enhancement ratio with frequency, acoustic cavitation was identified as the dominant mechanism of the enhancement. The enhancement ratio and critical radius of the cavitation bubble was observed to be highly correlated ($R = 0.95$).
- The variation of the enhancement ratio with other parameters including feed temperature and salt concentration is in accordance with acoustic cavitation being the dominant mechanism behind the observed improvement.
- The intermittent application of ultrasound in a long-term operation resulted in a relatively higher permeate flux and better salt rejection when compared to the case with no ultrasound.
- Applying ultrasound was found to be more efficient in terms of total energy required to produce a unit mass of freshwater.
- Future work will be needed to study the effect of ultrasonic energy to mitigate membrane scaling and foiling in S-VMD systems using high concentration feed water with a large suspended solid content.

6 CONCLUSIONS

Solar-powered membrane distillation (SP-MD) is examined as a promising renewable solution in the desalination and water treatment industry. While previous studies focused more on utilizing solar energy indirectly (i.e. to heat the feed water outside the MD module), researchers have recently proposed *direct* SP-MD systems that integrate the solar collector and the membrane in one compact standalone device that is suitable for small-scale applications. In this dissertation, we provided a comprehensive review of these systems in Chapter 2. In addition, we proposed two novel systems that are based on the direct SP-MD designs in Chapter 3 and Chapter 4. Finally, we proposed using ultrasound to enhance permeate flux and efficiency that can be used in these devices.

In Chapter 3, an innovative direct contact membrane distillation (DCMD) module to directly utilize solar thermal energy was proposed. The proposed system integrates capillary membranes inside evacuated tube solar collectors in order to achieve a more compact system. The performance of the direct SP-MD module was measured first indoors in a bench-scale experiment, and then tested outdoors under sunlight. Results showed that applying radiation directly can enhance the efficiency and permeate flux up to 17% compared to the same process when radiation is not applied under the same operating conditions. The daily operation of a stand-alone, directly heated SP-MD unit equipped with 0.035 m^2 membrane area achieved a permeate flux of 2.2 to 6.5 $kg \cdot m^{-2} \cdot h^{-1}$ depending on solar intensity.

In Chapter 4, a novel solar-heated submerged vacuum membrane distillation (S-VMD) system that uses an evacuated tube collector as the feed container was proposed. In this system, the hydrophobic membranes are directly submerged within the feed water,

eliminating the need for feed pumping. Indoor tests under steady-state operating conditions and daily outdoor tests under ambient weather conditions were conducted to investigate the system's functionality. The effect of two agitation techniques (aeration and internal circulation) to reduce temperature and concentration polarizations were studied. The daily performance tests revealed that the solar-heated S-VMD system can achieve a permeate flux of 5.9 to 11.1 $kg \cdot m^{-2} \cdot h^{-1}$ depending on solar intensity. The permeate flux was enhanced by 9% under aeration and by 22% under circulation in the outdoor tests. The water production per solar absorbing area can be as high as 0.96 $kg \cdot m^{-2} \cdot h^{-1}$. The system maintained a stable permeate flux and excellent water quality over a long-term operation. The small-scale system can provide fresh water in remote areas with limited natural resources.

In Chapter 5, an S-VMD system that uses ultrasonic energy as an agitation technique was proposed. The effects of ultrasonic power and frequency under different feed temperatures and concentrations were investigated experimentally. Results showed that applying low-power ultrasonic energy can improve the permeate flux up to 24% compared to the same process without ultrasonic energy under the same operating conditions. The ultrasound-assisted enhancement increases with the higher ultrasonic power and lower frequency, as well as lower feed temperature and higher concentration. Possible heat and mass transfer enhancement mechanisms associated with integration of ultrasound were investigated and based on the variation of the permeate flux with frequency, the enhancement was mainly attributed to acoustic cavitation. The ultrasonic-assisted S-VMD system maintained a stable permeate flux and excellent water quality over a relatively long-

term operation, indicating that ultrasonic energy is a promising and safe method to enhance the permeate flux in S-VMD systems.

7 FUTURE WORK

The two direct solar-powered MD systems we proposed in this dissertation are scalable, easy to implement, and could be applied to broader solar desalination markets. We estimate that the systems can potentially achieve a daily water production of 20-30 L per 1 m^2 of solar absorbing area. Our cost goal is to achieve a levelized cost of water (LCOW) of \$1/m^3 to make it competitive for off-grid or decentralized applications. In order to further improve the performance of these systems and demonstrate these goals, the following measures can be considered in future work:

1) Enhancing thermal efficiency: As discussed earlier, one drawback of the direct SP-MD systems is that a large amount of solar radiation goes to heating up the feed water before the distillation process takes place, which negatively impacts its thermal efficiency. Several techniques can be adopted to tackle this challenge which may include:

- **a)** Feed preheating: Feed preheating using conventional or renewable methods would allow more radiation to be used in the distillation process.
- **b)** Applying heat recovery scheme: the vapor generated in the distillation process can be passed to a condenser/heat exchanger to recover the heat of enthalpy, which can be used to preheat the feed or to provide thermal energy for residential or industrial heating applications. Moreover, a thermal energy storage unit can be integrated so the system can operate during the nighttime.
- **c)** Applying heat transfer enhancement methods: More heat is transferred from the solar collectors to the feed water if heat transfer enhancement methods such as using additives or extended surfaces are used.

2) **Optimizing the operating conditions:** It is important to consider several operating conditions in order to maximize the performance of the system. More tests need to be conducted in order to find the optimal operating conditions which may include:

a) The membrane type and surface area: Other types of membrane materials that can produce higher flux will be evaluated. Moreover, it is essential to determine the maximum membrane area per solar absorbing area so that the system can maintain a stable thermal operation with the most water production.

b) The tube inclination angle: It was found that the inclination angle of the solar collector can affect the performance of the membrane distillation. So, it is important to find the optimal inclination angle of the tubes to maximize both the absorbed solar radiation and water production.

c) The operation hours: Different scenarios can be studied to find optimal operation hours of the system to maximize the daily water production (i.e. is it better to run the system for longer hours or start running it at noon when the feed temperature is the highest). We can also investigate implementing a temperature–based control strategy so that the system only operates over a specified range of high temperatures.

3) **Conducting long-term operation with high concentrated feed:** So far, the functionality of the systems was demonstrated by measuring its performance using a synthetic saline water and low–salinity RO brine. However, in order to understand the system's performance in a real-life application, it is necessary to conduct long-term operation tests using a high concentration feed water (e.g. real inland brine or produced water). This will allow us to study the resulting fouling and scaling in the membrane which

can reduce the amount of distillate water and its quality. Different modes of feed agitation will be applied to study their effects on the membrane integrity for extended operation. Moreover, different operational strategies and cleaning protocols (e.g. rinsing, air backwashing, etc.) will be studied to ensure longer membrane life. It would be interesting to integrate ultrasound to the system in the outdoor test to induce turbulence in the feed and mitigate membrane fouling.

4) Building and testing a large-scale prototype: This can be the final prototype product to test and modify. It is important to design and build a prototype structure that is practical and scalable for real-world application and has long-term stability.

5) Economic analysis: Based on the results we obtain from the long-term tests and using the large-scale prototype, we will develop a detailed techno-economic model to calculate the levelized cost of water (LCOW). This will allow us to focus on lowering key cost drivers.

REFERENCES

[1] H. Sharon, K.S. Reddy, A review of solar energy driven desalination technologies, Renew. Sustain. Energy Rev. 41 (2015) 1080–1118. https://doi.org/10.1016/j.rser.2014.09.002.

[2] N. Ghaffour, T.M. Missimer, G.L. Amy, Technical review and evaluation of the economics of water desalination: Current and future challenges for better water supply sustainability, Desalination. 309 (2013) 197–207. https://doi.org/10.1016/j.desal.2012.10.015.

[3] J.G. Lee, N. Ghaffour, Predicting the performance of large-scale forward osmosis module using spatial variation model: Effect of operating parameters including temperature, Desalination. 469 (2019) 114095. https://doi.org/10.1016/j.desal.2019.114095.

[4] E. Drioli, A. Ali, F. Macedonio, Membrane distillation: Recent developments and perspectives, Desalination. 356 (2015) 56–84. https://doi.org/10.1016/j.desal.2014.10.028.

[5] J. Bundschuh, N. Ghaffour, H. Mahmoudi, M. Goosen, S. Mushtaq, J. Hoinkis, Low-cost low-enthalpy geothermal heat for freshwater production: Innovative applications using thermal desalination processes, Renew. Sustain. Energy Rev. 43 (2015) 196–206. https://doi.org/10.1016/j.rser.2014.10.102.

[6] F. Macedonio, A. Ali, T. Poerio, E. El-Sayed, E. Drioli, M. Abdel-Jawad, Direct contact membrane distillation for treatment of oilfield produced water, Sep. Purif. Technol. 126 (2014) 69–81. https://doi.org/10.1016/j.seppur.2014.02.004.

[7] N. Ghaffour, S. Soukane, J.-G. Lee, Y. Kim, A. Alpatova, Membrane distillation hybrids for water production and energy efficiency enhancement: A critical review, Appl. Energy. 254 (2019) 113698. https://doi.org/10.1016/j.apenergy.2019.113698.

[8] M.C. De Andrés, J. Doria, M. Khayet, L. Peñ, J.I. Mengual, Coupling of a membrane distillation module to a multieffect distiller for pure water production, Desalination. 115 (1998) 71–81. https://doi.org/10.1016/S0011-9164(98)00028-9.

[9] M. Khayet, Membranes and theoretical modeling of membrane distillation: A review, Adv. Colloid Interface Sci. 164 (2011) 56–88. https://doi.org/10.1016/j.cis.2010.09.005.

[10] A.M. Alklaibi, N. Lior, Membrane-distillation desalination: Status and potential, Desalination. 171 (2005) 111–131. https://doi.org/10.1016/j.desal.2004.03.024.

[11] L. Francis, N. Ghaffour, A.A. Alsaadi, G.L. Amy, Material gap membrane distillation: A new design for water vapor flux enhancement, J. Memb. Sci. 448 (2013) 240–247. https://doi.org/10.1016/j.memsci.2013.08.013.

[12] D. Winter, J. Koschikowski, S. Ripperger, Desalination using membrane distillation: Flux enhancement by feed water deaeration on spiral-wound modules, J. Memb. Sci. (2012). https://doi.org/10.1016/j.memsci.2012.08.018.

[13] P. Onsekizoglu, Membrane Distillation: Principle, Advances, Limitations and Future Prospects in Food Industry, Distill. - Adv. from Model. to Appl. (2012). https://doi.org/10.5772/37625.

[14] A. Alpatova, A.S. Alsaadi, M. Alharthi, J.G. Lee, N. Ghaffour, Co-axial hollow fiber module for air gap membrane distillation, J. Memb. Sci. 578 (2019) 172–182. https://doi.org/10.1016/j.memsci.2019.02.052.

[15] L.M. Camacho, L. Dumée, J. Zhang, J. de Li, M. Duke, J. Gomez, S. Gray, Advances in membrane distillation for water desalination and purification applications, Water (Switzerland). 5 (2013) 94–196. https://doi.org/10.3390/w5010094.

[16] M.R. Qtaishat, F. Banat, Desalination by solar powered membrane distillation systems, Desalination. 308 (2013) 186–197. https://doi.org/10.1016/j.desal.2012.01.021.

[17] A. Alkhudhiri, N. Darwish, N. Hilal, Membrane distillation: A comprehensive review, Desalination. 287 (2012) 2–18. https://doi.org/10.1016/j.desal.2011.08.027.

[18] A.S. Alsaadi, L. Francis, G.L. Amy, N. Ghaffour, Experimental and theoretical analyses of temperature polarization effect in vacuum membrane distillation, J. Memb. Sci. 471 (2014) 138–148. https://doi.org/10.1016/j.memsci.2014.08.005.

[19] R.B. Saffarini, E.K. Summers, H.A. Arafat, J.H. Lienhard V, Economic evaluation of stand-alone solar powered membrane distillation systems, Desalination. 299 (2012) 55–62. https://doi.org/10.1016/j.desal.2012.05.017.

[20] G. Gopi, G. Arthanareeswaran, I. AF, Perspective of renewable desalination by using membrane distillation, Chem. Eng. Res. Des. 144 (2019) 520–537. https://doi.org/10.1016/j.cherd.2019.02.036.

[21] F.E. Ahmed, R. Hashaikeh, N. Hilal, Solar powered desalination – Technology, energy and future outlook, Desalination. 453 (2019) 54–76. https://doi.org/10.1016/j.desal.2018.12.002.

[22] T. Sokhansefat, A. Kasaeian, K. Rahmani, A.H. Heidari, F. Aghakhani, O. Mahian, Thermoeconomic and environmental analysis of solar flat plate and evacuated tube collectors in cold climatic conditions, Renew. Energy. (2018). https://doi.org/10.1016/j.renene.2017.08.057.

[23] E. Jones, M. Qadir, M.T.H. van Vliet, V. Smakhtin, S. mu Kang, The state of desalination and brine production: A global outlook, Sci. Total Environ. 657 (2019) 1343–1356. https://doi.org/10.1016/j.scitotenv.2018.12.076.

[24] S. Al-Obaidani, E. Curcio, F. Macedonio, G. Di Profio, H. Al-Hinai, E. Drioli, Potential of membrane distillation in seawater desalination: Thermal efficiency, sensitivity study and cost estimation, J. Memb. Sci. 323 (2008) 85–98. https://doi.org/10.1016/j.memsci.2008.06.006.

[25] N. Ghaffour, J. Bundschuh, H. Mahmoudi, M.F. a. Goosen, Renewable energy-driven desalination technologies: A comprehensive review on challenges and potential applications of integrated systems., Desalination. 356 (2015) 94–114. https://doi.org/10.1016/j.desal.2014.10.024.

[26] D.M. Warsinger, J. Swaminathan, E. Guillen-Burrieza, H.A. Arafat, J.H. Lienhard V, Scaling and fouling in membrane distillation for desalination applications: A review, Desalination. (2015). https://doi.org/10.1016/j.desal.2014.06.031.

[27] R. Porrazzo, A. Cipollina, M. Galluzzo, G. Micale, A neural network-based optimizing control system for a seawater-desalination solar-powered membrane distillation unit, Comput. Chem. Eng. 54 (2013) 79–96. https://doi.org/10.1016/j.compchemeng.2013.03.015.

[28] N. Palanisami, K. He, I.S. Moon, Utilization of solar energy for direct contact membrane distillation process: An experimental study for desalination of real seawater, Korean J. Chem. Eng. 31 (2014) 155–161. https://doi.org/10.1007/s11814-013-0250-1.

[29] A. Shafieian, M. Khiadani, A novel solar-driven direct contact membrane-based water desalination system, Energy Convers. Manag. 199 (2019) 112055. https://doi.org/10.1016/j.enconman.2019.112055.

[30] A.E. Kabeel, M. Abdelgaied, E.M.S. El-Said, Study of a solar-driven membrane distillation system: Evaporative cooling effect on performance enhancement, Renew. Energy. 106 (2017) 192–200. https://doi.org/10.1016/j.renene.2017.01.030.

[31] J.G. Lee, W.S. Kim, J.S. Choi, N. Ghaffour, Y.D. Kim, Dynamic solar-powered multi-stage direct contact membrane distillation system: Concept design, modeling and simulation, Desalination. 435 (2018) 278–292. https://doi.org/10.1016/j.desal.2017.04.008.

[32] F. Suárez, S.W. Tyler, A.E. Childress, A theoretical study of a direct contact membrane distillation system coupled to a salt-gradient solar pond for terminal lakes reclamation, Water Res. 44 (2010) 4601–4615. https://doi.org/10.1016/j.watres.2010.05.050.

[33] T.C. Chen, C.D. Ho, Immediate assisted solar direct contact membrane distillation in saline water desalination, J. Memb. Sci. 358 (2010) 122–130. https://doi.org/10.1016/j.memsci.2010.04.037.

[34] E.K. Summers, J.H. Lienhard, Experimental study of thermal performance in air gap

membrane distillation systems, including the direct solar heating of membranes, Desalination. 330 (2013) 100–111. https://doi.org/10.1016/j.desal.2013.09.023.

[35] Q. Ma, A. Ahmadi, C. Cabassud, Direct integration of a vacuum membrane distillation module within a solar collector for small-scale units adapted to seawater desalination in remote places: Design, modeling & evaluation of a flat-plate equipment, J. Memb. Sci. 564 (2018) 617–633. https://doi.org/10.1016/j.memsci.2018.07.067.

[36] Q. Ma, A. Ahmadi, C. Cabassud, Optimization and design of a novel small-scale integrated vacuum membrane distillation - solar flat-plate collector module with heat recovery strategy through heat pumps, Desalination. 478 (2020) 114285. https://doi.org/10.1016/j.desal.2019.114285.

[37] Q. Li, L.J. Beier, J. Tan, C. Brown, B. Lian, W. Zhong, Y. Wang, C. Ji, P. Dai, T. Li, P. Le Clech, H. Tyagi, X. Liu, G. Leslie, R.A. Taylor, An integrated, solar-driven membrane distillation system for water purification and energy generation, Appl. Energy. 237 (2019) 534–548. https://doi.org/10.1016/j.apenergy.2018.12.069.

[38] S. Ben Abdallah, N. Frikha, S. Gabsi, Study of the performances of different configurations of seawater desalination with a solar membrane distillation, Desalin. Water Treat. 52 (2014) 2362–2371. https://doi.org/10.1080/19443994.2013.792746.

[39] A. Zrelli, B. Chaouchi, S. Gabsi, Simulation of vacuum membrane distillation coupled with solar energy: Optimization of the geometric configuration of a helically coiled fiber, Desalin. Water Treat. 36 (2011) 41–49. https://doi.org/10.5004/dwt.2011.1831.

[40] P.D. Dongare, A. Alabastri, S. Pedersen, K.R. Zodrow, N.J. Hogan, O. Neumann, J. Wud, T. Wang, A. Deshmukh, M. Elimelech, Q. Li, P. Nordlander, N.J. Halas, Nanophotonics-enabled solar membrane distillation for off-grid water purification, Proc. Natl. Acad. Sci. U. S. A. 114 (2017) 6936–6941. https://doi.org/10.1073/pnas.1701835114.

[41] J. Wu, K.R. Zodrow, P.B. Szemraj, Q. Li, Photothermal nanocomposite membranes for direct solar membrane distillation, J. Mater. Chem. A. 5 (2017) 23712–23719. https://doi.org/10.1039/c7ta04555g.

[42] A. Politano, P. Argurio, G. Di Profio, V. Sanna, A. Cupolillo, S. Chakraborty, H.A. Arafat, E. Curcio, Photothermal Membrane Distillation for Seawater Desalination, Adv. Mater. 29 (2017) 1–6. https://doi.org/10.1002/adma.201603504.

[43] M. Khayet, Solar desalination by membrane distillation: Dispersion in energy consumption analysis and water production costs (a review), Desalination. 308 (2013) 89–101. https://doi.org/10.1016/j.desal.2012.07.010.

[44] S. Bell, A beginner's guide to uncertainty of measurement., Natl. Phys. Lab. (2004) 1–41. https://doi.org/10.1111/j.1468-3148.2007.00360.x.

[45] H. Jafari Mosleh, S.J. Mamouri, M.B. Shafii, A. Hakim Sima, A new desalination system using a combination of heat pipe, evacuated tube and parabolic through collector, Energy Convers. Manag. 99 (2015) 141–150. https://doi.org/10.1016/j.enconman.2015.04.028.

[46] M.S. El-Bourawi, Z. Ding, R. Ma, M. Khayet, A framework for better understanding membrane distillation separation process, J. Memb. Sci. 285 (2006) 4–29. https://doi.org/10.1016/j.memsci.2006.08.002.

[47] S. Soukane, M.W. Naceur, L. Francis, A. Alsaadi, N. Ghaffour, Effect of feed flow pattern on the distribution of permeate fluxes in desalination by direct contact membrane distillation, Desalination. 418 (2017) 43–59. https://doi.org/10.1016/j.desal.2017.05.028.

[48] A. Bamasag, T. Alqahtani, S. Sinha, P. Phelan, Experimental Investigation of a Membrane Distillation System Using Solar Evacuated Tubes, in: Vol. 6 Energy, American Society of Mechanical Engineers, 2019. https://doi.org/10.1115/IMECE2019-11486.

[49] A.S. Alsaadi, L. Francis, H. Maab, G.L. Amy, N. Ghaffour, Evaluation of air gap membrane distillation process running under sub-atmospheric conditions: Experimental and simulation studies, J. Memb. Sci. 489 (2015) 73–80. https://doi.org/10.1016/j.memsci.2015.04.008.

[50] A. Criscuoli, M.C. Carnevale, E. Drioli, Evaluation of energy requirements in membrane distillation, Chem. Eng. Process. Process Intensif. 47 (2008) 1098–1105. https://doi.org/10.1016/j.cep.2007.03.006.

[51] A.S. Alsaadi, A. Alpatova, J.G. Lee, L. Francis, N. Ghaffour, Flashed-feed VMD configuration as a novel method for eliminating temperature polarization effect and enhancing water vapor flux, J. Memb. Sci. 563 (2018) 175–182. https://doi.org/10.1016/j.memsci.2018.05.060.

[52] L. Francis, N. Ghaffour, A.S. Al-Saadi, G.L. Amy, Submerged membrane distillation for seawater desalination, Desalin. Water Treat. 55 (2015) 2741–2746. https://doi.org/10.1080/19443994.2014.946716.

[53] S. Meng, Y.C. Hsu, Y. Ye, V. Chen, Submerged membrane distillation for inland desalination applications, Desalination. 361 (2015) 72–80. https://doi.org/10.1016/j.desal.2015.01.038.

[54] H. Julian, S. Meng, H. Li, Y. Ye, V. Chen, Effect of operation parameters on the mass transfer and fouling in submerged vacuum membrane distillation crystallization (VMDC) for inland brine water treatment, J. Memb. Sci. 520 (2016)

679–692. https://doi.org/10.1016/j.memsci.2016.08.032.

[55] Y. Choi, G. Naidu, S. Jeong, S. Vigneswaran, S. Lee, R. Wang, A.G. Fane, Experimental comparison of submerged membrane distillation configurations for concentrated brine treatment, Desalination. 420 (2017) 54–62. https://doi.org/10.1016/j.desal.2017.06.024.

[56] W. Zhong, H. Li, Y. Ye, V. Chen, Evaluation of silica fouling for coal seam gas produced water in a submerged vacuum membrane distillation system, Desalination. 393 (2016) 52–64. https://doi.org/10.1016/j.desal.2016.03.004.

[57] T.H. Khaing, J. Li, Y. Li, N. Wai, F.S. Wong, Feasibility study on petrochemical wastewater treatment and reuse using a novel submerged membrane distillation bioreactor, Sep. Purif. Technol. 74 (2010) 138–143. https://doi.org/10.1016/j.seppur.2010.05.016.

[58] J. Phattaranawik, A.G. Fane, A.C.S. Pasquier, W. Bing, A novel membrane bioreactor based on membrane distillation, Desalination. (2008). https://doi.org/10.1016/j.desal.2007.02.075.

[59] J. Phattaranawik, A.G. Fane, A.C.S. Pasquier, W. Bing, F.S. Wong, Experimental study and design of a submerged membrane distillation bioreactor, Chem. Eng. Technol. (2009). https://doi.org/10.1002/ceat.200800498.

[60] Y. Choi, G. Naidu, S. Jeong, S. Lee, S. Vigneswaran, Fractional-submerged membrane distillation crystallizer (F-SMDC) for treatment of high salinity solution, Desalination. 440 (2018) 59–67. https://doi.org/10.1016/j.desal.2018.01.027.

[61] H. Julian, Y. Ye, H. Li, V. Chen, Scaling mitigation in submerged vacuum membrane distillation and crystallization (VMDC) with periodic air-backwash, J. Memb. Sci. 547 (2018) 19–33. https://doi.org/10.1016/j.memsci.2017.10.035.

[62] T. Zou, G. Kang, M. Zhou, M. Li, Y. Cao, Submerged vacuum membrane distillation crystallization (S-VMDC) with turbulent intensification for the concentration of NaCl solution, Sep. Purif. Technol. 211 (2019) 151–161. https://doi.org/10.1016/j.seppur.2018.09.072.

[63] J.P. Mericq, S. Laborie, C. Cabassud, Evaluation of systems coupling vacuum membrane distillation and solar energy for seawater desalination, Chem. Eng. J. 166 (2011) 596–606. https://doi.org/10.1016/j.cej.2010.11.030.

[64] A. Bamasag, T. Alqahtani, S. Sinha, N. Ghaffour, P. Phelan, Experimental investigation of a solar-heated direct contact membrane distillation system using evacuated tube collectors, Desalination. 487 (2020). https://doi.org/10.1016/j.desal.2020.114497.

[65] Y.D. Kim, L. Francis, J.G. Lee, M.G. Ham, N. Ghaffour, Effect of non-woven net

spacer on a direct contact membrane distillation performance: Experimental and theoretical studies, J. Memb. Sci. 564 (2018) 193–203. https://doi.org/10.1016/j.memsci.2018.07.019.

[66] G. Chen, X. Yang, R. Wang, A.G. Fane, Performance enhancement and scaling control with gas bubbling in direct contact membrane distillation, Desalination. 308 (2013) 47–55. https://doi.org/10.1016/j.desal.2012.07.018.

[67] P.H. Gleick, Basic water requirements for human activities: Meeting basic needs, Water Int. 21 (1996) 83–92. https://doi.org/10.1080/02508069608686494.

[68] A. Alpatova, A. Alsaadi, N. Ghaffour, Boron evaporation in thermally-driven seawater desalination: Effect of temperature and operating conditions, J. Hazard. Mater. 351 (2018) 224–231. https://doi.org/10.1016/j.jhazmat.2018.02.056.

[69] J.G. Lee, W.S. Kim, J.S. Choi, N. Ghaffour, Y.D. Kim, A novel multi-stage direct contact membrane distillation module: Design, experimental and theoretical approaches, Water Res. 107 (2016) 47–56. https://doi.org/10.1016/j.watres.2016.10.059.

[70] A. Luo, N. Lior, Critical review of membrane distillation performance criteria, Desalin. Water Treat. 57 (2016) 20093–20140. https://doi.org/10.1080/19443994.2016.1152637.

[71] J.A. Andrés-Mañas, A. Ruiz-Aguirre, F.G. Acién, G. Zaragoza, Performance increase of membrane distillation pilot scale modules operating in vacuum-enhanced air-gap configuration, Desalination. 475 (2020). https://doi.org/10.1016/j.desal.2019.114202.

[72] H.C. Duong, L. Xia, Z. Ma, P. Cooper, W. Ela, L.D. Nghiem, Assessing the performance of solar thermal driven membrane distillation for seawater desalination by computer simulation, J. Memb. Sci. 542 (2017) 133–142. https://doi.org/10.1016/j.memsci.2017.08.007.

[73] P.A. Hogan, Sudjito, A.G. Fane, G.L. Morrison, Desalination by solar heated membrane distillation, Desalination. 81 (1991) 81–90. https://doi.org/10.1016/0011-9164(91)85047-X.

[74] M.A.A. Hejazi, O.A. Bamaga, M.H. Al-Beirutty, L. Gzara, H. Abulkhair, Effect of intermittent operation on performance of a solar-powered membrane distillation system, Sep. Purif. Technol. 220 (2019) 300–308. https://doi.org/10.1016/j.seppur.2019.03.055.

[75] M. Rezaei, D.M. Warsinger, J.H. Lienhard V, M.C. Duke, T. Matsuura, W.M. Samhaber, Wetting phenomena in membrane distillation: Mechanisms, reversal, and prevention, Water Res. 139 (2018) 329–352. https://doi.org/10.1016/j.watres.2018.03.058.

[76] P. Wang, T.S. Chung, Recent advances in membrane distillation processes: Membrane development, configuration design and application exploring, J. Memb. Sci. 474 (2015) 39–56. https://doi.org/10.1016/j.memsci.2014.09.016.

[77] A. Bamasag, T. Alqahtani, S. Sinha, N. Ghaffour, P. Phelan, Solar-heated submerged vacuum membrane distillation system with agitation techniques for desalination, Sep. Purif. Technol. (2020) 117855. https://doi.org/10.1016/j.seppur.2020.117855.

[78] M. Legay, N. Gondrexon, S. Le Person, P. Boldo, A. Bontemps, Enhancement of heat transfer by ultrasound: Review and recent advances, Int. J. Chem. Eng. 2011 (2011). https://doi.org/10.1155/2011/670108.

[79] H. Daghooghi-Mobarakeh, N. Campbell, W.K. Bertrand, P.G. Kumar, S. Tiwari, L. Wang, R. Wang, M. Miner, P.E. Phelan, Ultrasound-assisted regeneration of zeolite/water adsorption pair, Ultrason. Sonochem. 64 (2020) 105042. https://doi.org/10.1016/j.ultsonch.2020.105042.

[80] M. Qasim, N.N. Darwish, S. Mhiyo, N.A. Darwish, N. Hilal, The use of ultrasound to mitigate membrane fouling in desalination and water treatment, Desalination. 443 (2018) 143–164. https://doi.org/10.1016/j.desal.2018.04.007.

[81] O. Naji, R.A. Al-juboori, L. Bowtell, A. Alpatova, N. Ghaffour, Direct contact ultrasound for fouling control and flux enhancement in air-gap membrane distillation, Ultrason. Sonochem. 61 (2020). https://doi.org/10.1016/j.ultsonch.2019.104816.

[82] C. Zhu, G.L. Liu, C.S. Cheung, C.W. Leung, Z.C. Zhu, Ultrasonic stimulation on enhancement of air gap membrane distillation, J. Memb. Sci. 161 (1999) 85–93. https://doi.org/10.1016/S0376-7388(99)00105-2.

[83] D. Hou, G. Dai, H. Fan, H. Huang, J. Wang, An ultrasonic assisted direct contact membrane distillation hybrid process for desalination, J. Memb. Sci. 476 (2015) 59–67. https://doi.org/10.1016/j.memsci.2014.11.028.

[84] D. Hou, Z. Wang, G. Li, H. Fan, J. Wang, H. Huang, Ultrasonic assisted direct contact membrane distillation hybrid process for membrane scaling mitigation, Desalination. 375 (2015) 33–39. https://doi.org/10.1016/j.desal.2015.07.018.

[85] D. Hou, L. Zhang, C. zhao, H. Fan, J. Wang, H. Huang, Ultrasonic irradiation control of silica fouling during membrane distillation process, Desalination. 386 (2016) 48–57. https://doi.org/10.1016/j.desal.2016.02.032.

[86] H. Cho, J. Choi, Y. Choi, S. Lee, Ultrasonic-assisted removal of inorganic scales in high-salinity wastewater treatment using membrane distillation, Desalin. Water Treat. 157 (2019) 383–392. https://doi.org/10.5004/dwt.2019.24043.

[87] C. Zhu, G. Liu, Modeling of ultrasonic enhancement on membrane distillation, J. Memb. Sci. 176 (2000) 31–41. https://doi.org/10.1016/S0376-7388(00)00426-9.

[88] P. Gao, X. Zhou, B. Cheng, D. Zhang, G. Zhou, Study on heat and mass transfer of droplet cooling in ultrasound wave, Int. J. Heat Mass Transf. 107 (2017) 916–924. https://doi.org/10.1016/j.ijheatmasstransfer.2016.11.002.

[89] Y. Shen, K. Yasui, Z. Sun, B. Mei, M. You, T. Zhu, Study on the spatial distribution of the liquid temperature near a cavitation bubble wall, Ultrason. Sonochem. 29 (2016) 394–400. https://doi.org/10.1016/j.ultsonch.2015.10.015.

[90] X. Ma, B. Huang, Y. Li, Q. Chang, S. Qiu, Z. Su, X. Fu, G. Wang, Numerical simulation of single bubble dynamics under acoustic travelling waves, Ultrason. Sonochem. 42 (2018) 619–630. https://doi.org/10.1016/j.ultsonch.2017.12.021.

[91] F.J. Trujillo, K. Knoerzer, A computational modeling approach of the jet-like acoustic streaming and heat generation induced by low frequency high power ultrasonic horn reactors, Ultrason. Sonochem. 18 (2011) 1263–1273. https://doi.org/10.1016/j.ultsonch.2011.04.004.

[92] B. Li, X. Han, Z. Wan, X. Wang, Y. Tang, Influence of ultrasound on heat transfer of copper tubes with different surface characteristics in sub-cooled boiling, Appl. Therm. Eng. 92 (2016) 93–103. https://doi.org/10.1016/j.applthermaleng.2015.09.069.

[93] H. Kiani, D.W. Sun, Z. Zhang, The effect of ultrasound irradiation on the convective heat transfer rate during immersion cooling of a stationary sphere, Ultrason. Sonochem. 19 (2012) 1238–1245. https://doi.org/10.1016/j.ultsonch.2012.04.009.

[94] D.W. Zhou, D.Y. Liu, X.G. Hu, C.F. Ma, Effect of acoustic cavitation on boiling heat transfer, Exp. Therm. Fluid Sci. 26 (2002) 931–938. https://doi.org/10.1016/S0894-1777(02)00201-7.

[95] K. Kerboua, O. Hamdaoui, Influence of reactions heats on variation of radius, temperature, pressure and chemical species amounts within a single acoustic cavitation bubble, Ultrason. Sonochem. 41 (2018) 449–457. https://doi.org/10.1016/j.ultsonch.2017.10.001.

[96] J.L. Laborde, A. Hita, J.P. Caltagirone, A. Gerard, Fluid dynamics phenomena induced by power ultrasounds, Ultrasonics. 38 (2000) 297–300. https://doi.org/10.1016/S0041-624X(99)00124-9.

[97] N. Riley, Acoustic streaming, Theor. Comput. Fluid Dyn. 10 (1998) 349–356. https://doi.org/10.1007/s001620050068.

[98] T. Thanh, Y. Asakura, S. Koda, K. Yasuda, Ultrasonics - Sonochemistry Dependence of cavitation , chemical e ff ect , and mechanical e ff ect thresholds on

ultrasonic frequency, 39 (2017) 301–306. https://doi.org/10.1016/j.ultsonch.2017.04.037.

[99] J. Cai, X. Huai, R. Yan, Y. Cheng, Numerical simulation on enhancement of natural convection heat transfer by acoustic cavitation in a square enclosure, Appl. Therm. Eng. 29 (2009) 1973–1982. https://doi.org/10.1016/j.applthermaleng.2008.09.015.

[100] N.P. Dhanalakshmi, R. Nagarajan, N. Sivagaminathan, B.V.S.S.S. Prasad, Chemical Engineering and Processing : Process Intensification Acoustic enhancement of heat transfer in furnace tubes, Chem. Eng. Process. Process Intensif. 59 (2012) 36–42. https://doi.org/10.1016/j.cep.2012.05.001.

[101] Y. Chen, S. Sun, Y. Lai, C. Ma, Influence of ultrasound to convectional heat transfer with fouling of cooling water, Appl. Therm. Eng. 100 (2016) 340–347. https://doi.org/10.1016/j.applthermaleng.2016.01.144.

[102] A.J. Walton, G.T. Reynolds, Sonoluminescence, Adv. Phys. 33 (1984) 595–660. https://doi.org/10.1080/00018738400101711.

[103] L.A. Crum, Acoustic cavitation series:part five:Rectified diffusion, Ultrasonics. (1984) 215–223.

[104] S.K. Bhangu, M. Ashokkumar, Theory of Sonochemistry, Top. Curr. Chem. 374 (2016) 1–28. https://doi.org/10.1007/s41061-016-0054-y.

[105] B.J.P. Lorimer, T.J. Mason, Sonochemistry:Part 1-The Physical Aspects *, Chem. Soc. Rev. 3 (1987) 239–274.

[106] S.A. Perusich, R.C. Alkire, Ultrasonically Induced Cavitation Studies of Electrochemical Passivity and Transport Mechanisms: II . Experimental, J. Electrochem. Soc. 138 (1991) 708–713. https://doi.org/10.1149/1.2085662.

[107] C.K. Chiam, R. Sarbatly, Vacuum membrane distillation processes for aqueous solution treatment-A review, Chem. Eng. Process. - Process Intensif. 74 (2013) 27–54. https://doi.org/10.1016/j.cep.2013.10.002.

[108] R. Miladi, N. Frikha, A. Kheiri, S. Gabsi, Energetic performance analysis of seawater desalination with a solar membrane distillation, Energy Convers. Manag. 185 (2019) 143–154. https://doi.org/10.1016/j.enconman.2019.02.011.

[109] Y.S. Chang, B.S. Ooi, A.L. Ahmad, C.P. Leo, W.J. Lau, Numerical study on performance and efficiency of batch submerged vacuum membrane distillation for desalination, Chem. Eng. Res. Des. 163 (2020) 217–229. https://doi.org/10.1016/j.cherd.2020.08.031.

APPENDIX A

CO-AUTHOR PERMISSION STATEMENT

The chapters in this dissertation consist of collaborative work in which Ahmad Bamasag is the first listed co-author. All co-authors have granted their permissions for this co-authored work to be used in this dissertation.

APPENDIX B

LIST OF PUBLICATIONS

List of Publications:

1) **Bamasag, A.**, Daghooghi-Mobarakeh, H., Alqahtani, T., & Phelan, P. E. (2020). Performance enhancement of a submerged vacuum membrane distillation (S-VMD) system using low-power ultrasound. *(submitted for publication).*[**]
2) **Bamasag, A.**, Alqahtani, T., Sinha, S., Ghaffour, N., & Phelan, P. (2020). Solar-heated submerged vacuum membrane distillation system with agitation techniques for desalination. *Separation and Purification Technology*, 117855.[**]
3) Alqahtani, T., **Bamasag, A.**, Mellouli, S., Askri, F., & Phelan, P. E. (2020). Cyclic behaviors of a novel design of a metal hydride reactor encircled by cascaded phase change materials. *International Journal of Hydrogen Energy*.
4) Alqahtani, T., Mellouli, S., **Bamasag, A.**, Askri, F., & Phelan, P. E. (2020). Thermal performance analysis of a metal hydride reactor encircled by a phase change material sandwich bed. *International Journal of Hydrogen Energy*, *45*(43), 23076-23092.
5) **Bamasag, A.**, Alqahtani, T., Sinha, S., Ghaffour, N., & Phelan, P. (2020). Experimental investigation of a solar-heated direct contact membrane distillation system using evacuated tube collectors. *Desalination*, *487*, 114497. [**]
6) Alqahtani, T., Mellouli, S., **Bamasag, A.**, Askri, F., & Phelan, P. E. (2020). Experimental and numerical assessment of using coconut oil as a phase-change material for unconditioned buildings. *International Journal of Energy Research*, *44*(7), 5177-5196.
7) **Bamasag, A.**, Alqahtani, T., Sinha, S., & Phelan, P. (2019, November). Experimental investigation of a membrane distillation system using solar evacuated tubes. In *ASME International Mechanical Engineering Congress and Exposition* (Vol. 59438, p. V006T06A059). American Society of Mechanical Engineers.

[**] Publications used in this dissertation.